Optical antennas for single molecule fluorescence detection at physiological concentration

Deep Punj

To cite this version:

Deep Punj. Optical antennas for single molecule fluorescence detection at physiological concentration. Optics [physics.optics]. Aix Marseille université, 2014. English. NNT : . tel-01119033

HAL Id: tel-01119033
https://theses.hal.science/tel-01119033v1

Submitted on 20 Feb 2015

OPTICAL ANTENNAS FOR SINGLE MOLECULE FLUORESCENCE DETECTION AT PHYSIOLOGICAL CONCENTRATION

THÈSE

pour obtenir le grade de

DOCTEUR DE L'UNIVERSITE d'Aix-Marseille

Faculté des Sciences et Techniques

présentée et soutenue publiquement par

Deep PUNJ

le 17 Décembre 2014

ECOLE DOCTORALE :	Physique & Sciences de la matière
MENTION :	Optique, Photonique et Traitment d'Image

JURY :

Pr.	Philip TINNEFELD	: Président
Dr.	Sébastien BIDAULT	: Rapporteur
Dr.	Cyriaque GENET	: Rapporteur
Dr.	Sophie BRASSELET	: Examinateur
Dr.	Jérome WENGER	: Directeur de thèse
Dr.	Hervé RIGNEAULT	: Co-directeur de thèse

Abstract

Optical nanoantennas provide a rich control over light at nanoscale to achieve high field enhancement and localization with a large absorption cross-sections. Considering the need for these virtues in broad range of fields the possible applications of these nanoantennas span into the fields of spectroscopy, photovoltaics, single photon sources, biological sensing. This thesis work mainly focuses on characterizing and manipulating optical antenna to detect single molecule fluorescence signal at high concentration of micromolar regime. At such high concentration we need to get the detection volume reduced at least three orders of magnitude beyond diffraction limits. Also the fluorescence signal enhancement is needed to have better value in order to have a single molecule stand out from the background. Chapter 1 deals with the motivation of the thesis by discussing about the well established strategies already applied to tackle the issues of volume reduction and fluorescence rate enhancement and how to go beyond the limitations of these methods. In Chapter 2 we discuss the local surface plasmonic properties of optical nanoantennas responsible for the local field enhancement and give an overview of the applications of optical antennas. Chapter 3 gives the detailed idea of the experimental techniques (Fluorescence Correlation Spectroscopy and Time correlated Single Photon Counting) that have been used to characterize the influence of Optical nanoantenna. Chapter 4 introduces the novel "antenna-in-box" platform, based on a gap-antenna inside a nanoaperture, which combines both enhancement and background screening, offering high single molecule sensitivity at micromolar concentrations. We demonstrate gap-antenna detection volumes of zeptoliter dimensions, corresponding to a 10^4-volume reduction compared to diffraction-limited optics, fluorescence enhancement up to 1100-fold and microsecond transit time. In the last Chapter 5 we show the experimental results on single gold nanoparticles with various diameters giving the idea that with 80 nm gold nanoparticle we can achieve detection volumes down to 270 zeptoliters (three orders of magnitude beyond the diffraction barrier) together with 60-fold enhancement of the fluorescence brightness per molecule. This chapter also includes results on dimers and trimers of 80 nm gold nanoparticles showing light confinement comparable to the "antenna-in-box” platform.

The results in this thesis demonstrates the potential of optical antennas, fabricated by top-down ("antenna-in-box” platform) and bottom-up approach (colloidal synthesis of antennas using gold nanoparticles), to confine light and detect single molecule fluorescence at biologically relevant high concentrations regime.

Résumé

Les nanoantennes optiques offrent un contrôle riche sur la lumière à l'échelle nanométrique pour réaliser la mise en valeur de champ élevé et localisation avec une grande sections efficaces d'absorption. Considérant la nécessité pour ces vertus dans des domaines très divers les applications possibles de ces nanoantennes s'étendent dans les domaines de la spectroscopie, photovoltaïque, sources de photons uniques, détection biologique. Ce travail de thèse se concentre principalement sur la caractérisation et la manipulation antenne optique pour détecter seul signal de fluorescence de molécules à forte concentration de régime micromoles. Lors de cette forte concentration, nous devons obtenir le volume de détection réduite d'au moins trois ordres de grandeur au-delà des limites de diffraction. Aussi l'amélioration du signal de fluorescence est nécessaire d'avoir un meilleur rapport signal sur bruit afin d'avoir une seule molécule de se démarquer de l'arrière-plan. Chapitre 1 traite de la motivation de la thèse en discutant sur les stratégies bien établies déjà appliquées pour aborder les questions de la réduction du volume et l'amélioration du taux de fluorescence et comment aller au-delà des limites de ces méthodes. Dans le chapitre 2, nous discutons des propriétés de surface plasmoniques locaux de nanoantennes optiques responsables de la mise en valeur de champ local et donnons un aperçu des applications d'antennes optiques. Chapitre 3 donne l'idée détaillée des techniques expérimentales (corrélation de fluorescence de spectroscopie et Temps corrélation comptage de photons) qui ont été utilisées pour caractériser l'influence de la nano-antenne optique. Le chapitre 4 présente "antenne-in-box" plate-forme, basée sur un écart-antenne à l'intérieur d'un nanotrou, qui combine à la fois la mise en valeur et la vérification des antécédents, offrant une haute sensibilité de la molécule unique à des concentrations micromolaires. Nous démontrons volumes de détection écart-antenne de dimensions zeptoliter, correspondant à une réduction de 10^4-volume rapport à l'optique de diffraction limitée, l'amélioration de la fluorescence jusqu'à 1100 fois et le transit de la microseconde temps. Dans le dernier chapitre 5, nous montrons les résultats expérimentaux sur des nanoparticules d'or individuelles avec différents diamètres donnant l'idée que, avec 80 nm nanoparticules d'or, nous pouvons atteindre des volumes de détection jusqu'à 270 zeptoliters (trois ordres de grandeur au-delà de la barrière de diffraction) avec 60× l'amélioration de l'intensité de fluorescence par molécule. Ce chapitre comprend également les résultats actuels sur les dimères et trimères de 80 nm nanoparticules d'or montrant la lumière confinement comparable à la Plate-forme "antenne-in-box".

Les résultats de cette thèse démontre le potentiel des antennes optiques, fabriqué par top-down ("antenne-in-box" plate-forme) et l'approche bottom-up(synthèse colloïdale d'antennes

utilisant des nanoparticules d'or), pour confiner la lumière et de détecter la fluorescence d'une seule molécule au régime des concentrations élevées d'intérêt biologique.

Contents

Introduction

Single molecule study has become a major involvement of research in modern biophysics and every year more researchers are getting attracted to it. In order to find a general strategy to observe single molecule for a broader range of application, the biggest challenge is to overcome the limitation imposed by the diffraction. The microscopic observation volume must have only a single fluorescent molecule of interest during the measurement acquisition time to detect a single molecule. With the diffraction limited optics we get the focal volume of the order of 0.5 fL, which limits the concentration of the fluorescent species in the nanomolar range to get an isolated single molecule in the focal volume. Practically most biologically related processes involving binding or catalysis require the active molecule to be micro- to millimolar concentration regime [1, 2]. The common strategies of optical single molecule fluorescence detection viz. Fluorescence Correlation spectroscopy (FCS), Forster fluorescence resonance energy transfer (FRET), based on confocal microscopy [3] or total internal reflection fluorescence microscopy (TIRF) [4–6] are restricted by experimental condition limited by diffraction. Hence to get the single molecule resolution the detection volume should be decreased by at least three orders of magnitude to reach the physiological condition compared to the confocal condition [1, 7–11]. Besides this challenge, the diffraction phenomenon ultimately limits the amount of collected light from a single molecule and the achievable signal-to-background ratio which actually determines the maximum acquisition speed and temporal resolution of the experiments. As a consequence, single molecule detection can be performed only on fluorescent species which are relatively bright and have good photostability. To overcome this challenge, research have been going on to tailor the photonic environment surrounding the molecule that can affect the fluorescence emission.

The main goal of this thesis is to use Optical nanoantenna to manipulate the photonic environment surrounding the fluorophore in order to detect the single molecule fluorescence signal at micromolar concentration. Chapter 1 serves as the motivation of the thesis. In this chapter we will be discussing briefly about well established strategies already applied to tackle the key issue of circumventing the diffraction limit in order to detect single molecule fluorescence signal. In chapter 2 we talk about the light matter interaction at the nanoscale. Light matter interaction relies on the coupling between the single quantum emitters (fluorescent molecules, quantum dots) and the desired mode of radiation field [12]. These emitters have dimension very small compared to the wavelength and that is why they can be considered to be behaving like electric dipole [13]. And at nanoscale the transition between emitters and the radiation field has taken a great deal of advantage from plasmonics to exploit the unique optical properties of metallic nanostructures to confine light at nanometric regime [14]. In this chapter first we will discuss the optical properties of bulk noble metals based on Drude model. These properties are fundamentally important for dealing with the complex optical phenomena of metallic nanoantennas. Then we will go through the basics of localized surface plasmon resonance conditions that drives nanoantennas to localize the photon field in nanometric regime. In the next section we discuss about the optical antennas and how the radiative properties of emitter can be drastically modified by the presence of a nanoantenna. And finally we briefly go through some prominent applications of optical nanoantenna. Chapter 3 presents the experimental procedures for fluorescence characterization developed within our laboratory, which comprises combining the studies of fluorescence correlation spectroscopy and the measurements of fluorescence lifetime. This procedure allows to discriminate the relative excitation and emission gains contributing to the overall enhancement of fluorescence. We show that using a low quantum yield effect provides a better fluorescence enhancement effect.

In Chapter 4, we introduce a novel "antenna-in-box" platform, based on a gap-antenna inside a nanoaperture, which combines both enhancement and background screening, offering unprecedented single molecule sensitivity at ultrahigh sample concentrations. The rationale behind this design is that in any nanoantenna experiment on molecules in solution, the observed fluorescence is a sum of two contributions: the enhanced fluorescence from the few molecules in the nanoantnenna gap region (hot spot) and a flourescence background from several thousands of molecules within the diffraction-limited confocal volume (in our case at the concentration of $15\mu M$ of Alexa 647 fluor, we had 1 molecule in the hotspot and 4600 molecules in the confocal volume). The different components of our antenna-in-box therefore have complementary roles. A central gap-antenna creates the hot spot for enhancement and a surrounding nanoaperture screens the background by preventing direct excitation of molecules diffusing away from the central gap region. This work has been done in collaboration with Prof. Niek Van Hulst of Molecular Nanophotonics group, ICFO, Spain and Prof. María García-Parajo and Mattheiw Mivelle of Single Molecule Biophotonics group, ICFO, Spain. In order to achieve our goal to reduce the effective detection volume and enhance the fluorescence signal at high concentrated solution, gold nanoparticles have a strong appeal for practical applications to detect fluorescent molecules in solution owing to their large availability, low intrinsic cost, and tunable spectral response. In chapter 5 we investigate the colloidal synthesis of gold nanoparticles assembly. In the first section we probe individual spherical gold nanoparticles of diameter ranging from 60 nm to 150 nm, to perform enhanced single molecule fluorescence analysis in solutions at high (micromolar) concentrations. In the next section we show the experimental outcomes on dimers and trimers of gold nanoparticles of diameter 80 nm.

1 Photonic approaches to detect single molecule fluorescence at physiological concentration

1.1 Introduction: Single molecule fluorescence spectroscopy

Single molecule study has become a major involvement of research in modern biophysics and every year more researchers are getting attracted to it. The driving idea has been to understand the function of all constituent parts of living organisms. The single-molecule approach bears the intrinsic advantage to reveal information not normally accessible by ensemble measurements, such as sample heterogeneity, local concentration, and variances in kinetic rates. It does not require any perturbing synchronization of molecules to reach a sufficient ensemble-averaged signal, and it circumvents the need for 100% pure samples. Complex problems, such as protein structure folding, molecular motor operation or single-nucleotide polymorphism detection, are best studied at the single molecule level because of the molecular structure dispersion and the stochastic nature of the processes. Although modern molecular biology has made enormous progress in identifying single molecules and their functions, efficiently detecting a single molecule is still a major goal with applications in chemical, biochemical and biophysical analysis. Progress towards this goal crucially depends on the development of techniques that provide visualisation and imaging of processes down to the molecular scale in intact cells [15]. It is established that single molecule techniques have comparatively high vantage points and we have now advanced technology to perform these techniques. Even though there are key limitations of optical single-molecule techniques that have to be rectified in order to get the advantages of these techniques for various applications [10].

In order to find a general strategy to observe single molecule for a broader range of application, the biggest challenge is to overcome the limitation imposed by the diffraction. The microscopic observation volume must have only a single fluorescent molecule of interest during the measurement acquisition time to detect a single molecule. With the diffraction limited optics we get the focal volume of the order of 0.5 fL, which limits the concentration of the fluorescent species in the nanomolar range to get an isolated single molecule in the focal volume. Practically most biologically related processes involving binding or catalysis require the active molecule to be micro- to millimolar concentration regime as shown in Figure 1.1 [1,2]. The common strategies of optical single molecule fluorescence detection viz. Fluorescence Correlation spectroscopy (FCS), Forster fluorescence resonance energy transfer (FRET), based on confocal microscopy [3] or total internal reflection fluorescence microscopy (TIRF) [4–6] are restricted by experimental condition limited by diffraction. Hence to get the single molecule resolution the detection volume should be decreased by at least three orders of magnitude to reach the physiological condition compared to the confocal condition [1,7–11]. Besides this challenge, the diffraction phenomenon ultimately limits the amount of collected light from a single molecule and the achievable signal-to-background ratio which actually determines the maximum acquisition speed and temporal resolution of the experiments. As a consequence, single molecule detection can be performed only on fluorescent species which are relatively bright and have good photostability.

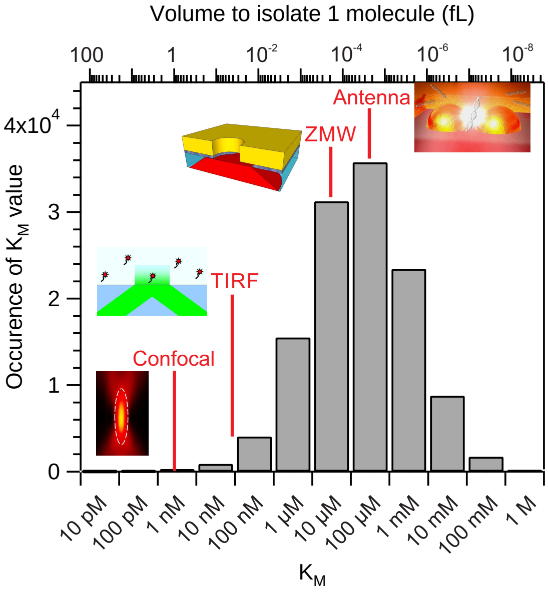

Figure 1.1: Histogram of Michaelis constant K_M for 118,000 enzymes taken from the brenda database (http://www.brenda-enzymes.org/) in November 2013. The top axis show the detection volume required to isolate a single molecule. The vertical bars indicate the effective concentration regime and detection volume reached by different techniques (TIRF: Total Internal Reflection fluorescence microscopy; ZMW: Zero mode waveguide)

To overcome this challenge, research have been going on to tailor the photonic environment surrounding the molecule that can affect the fluorescence emission in three ways: (i) by locally enhancing the excitation intensity, (ii) by increasing the emitter's radiative rate and quantum efficiency, and (iii) by modifying its radiation pattern, towards a higher emission directionality to the detectors [9].

In this chapter we will be discussing briefly about well established strategies already applied to tackle the key parameters of volume reduction and fluorescence rate enhancement. These strategies can be divided into two main areas. The first one takes advantages of shaping the laser excitation beam and the second area covers photonic nanostructural approaches [9].

1.2 Improving single molecule fluorescence detection

1.2.1 Methods by structuring the laser excitation beam

Confining the laser beam spatially on the nanoscale using several optical methodologies provides significant improvements (Figure:1.2). Although in practice these methodologies encounter unavoidable difficulties due to optical alignment issues.

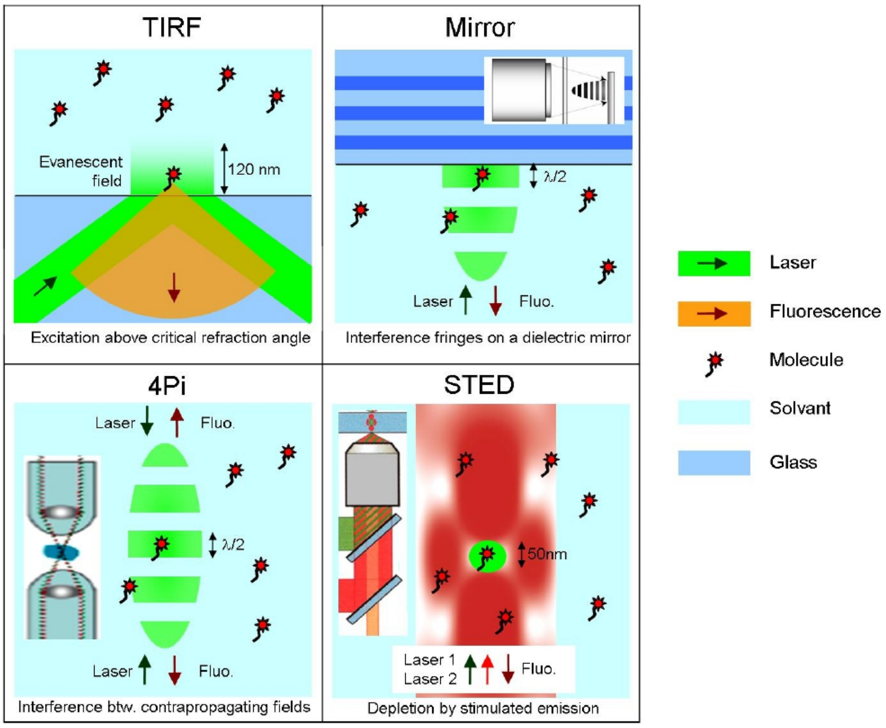

Figure 1.2: Different methods for improving single molecule fluorescence detection by taking advantages of structuring the laser excitation beam. Figure Courtesy [9].

Total internal reflection fluorescence microscopy(TIRF)

TIRF microscopy setup uses a prism or objective to excite the fluorescent molecules diffusing above the upper interface as shown in figure 1.2. Total internal reflection at the solid/liquid interface generates the evanescent wave for the illumination of fluorophores [4]. The detection volume defined by the evanescent field is reduced along the longitudinal direction. It typically extends ∼ $\lambda/6$ offering a reduction of 10 compared to conventional confocal microscopes. A constraint of this technique is that it does not provide lateral confinement of the excitation profile. TIRF-FCS offers a solution for lateral confinement by using a pinhole conjugated to the object plane to reduce the lateral extension of the detection profile [5]. This poses a serious issue of out-of-focus photobleaching, leading to a depletion of fluorophores and limiting the accuracy of FCS measurement.

Fluorescence detection on a mirror

Single molecule detection in solution is tightly bound to the implementation of confocal microscopy. An elegant way to reduce the confocal analysis volume and enhance the fluorescence rate emitted per molecule takes advantage of a dielectric mirror set at the focal point of the excitation beam as shown in figure 1.2. The mirror affects both the laser excitation intensity and pattern, and the collection of the emitted fluorescence. The coherent excitation beam, which is reflected, produces an interference pattern along the optical axis with an interfringe spacing of $\lambda/2n$, where λ is the excitation wavelength and n is the medium refractive index.

Two important effects occur when the confocal detection volume is located on the mirrors surface [16, 17]. First, interference fringes in the excitation beam give rise to a new characteristics time in the fluorescence correlation function. This new time is found to be independent of the transverse excitation fields beam waist and permits accurate measurement of diffusion coefficients without any a priori knowledge of the confocal volume geometry. Second, the count rate per emitter is significantly enhanced owing to control of spontaneous emission and enhancement of the excitation field, with a gain up to four times.

4Pi Microscopy

4Pi microscopy takes advantage of two opposite microscope objectives with high numerical apertures [18]. Coherent light from a laser is split into two beams, which are focused at the same point onto a sample by two opposite objectives. Constructive interference of the two beams enhances the focusing of the light, and the illuminated region gets narrower along the optical axis than in the case of the common confocal microscope. In 4pi microscopy, various types of illumination and detection are utilized: type A corresponds to the illumination via two objectives with constructive interference and detection through one of the objectives in a confocal mode.

Stimulated emission depletion microscopy (STED)

A different approach to overcome the diffraction barrier is to use stimulated emission depletion (STED) of the fluorescent molecular state (Fig. 1.2) [18]. STED is a far-field method bearing sub-diffraction analysis volumes suitable for FCS. In STED, a regular diffraction-limited focal spot (green) is used to excite the fluorescence, while a second laser beam (red) stimulates the excited molecules down to their ground state. The red laser beam is custom-tailored to feature a zero-intensity minimum at the center but high intensity in the focal periphery. This configuration ensures that fluorescence occurs only in the very center of the focal spots and is strongly suppressed in the spots periphery. An additional attractive feature of STED is that it allows to adjust the detection volume by increasing the power of the stimulating beam.

The first implementation of a STED experiment with FCS was shown by Kastrup et at. [19]. In a series of FCS measurements on a dilute solution of a red-fluorescing oxazine dye, the STED irradiance was successively increased yielding a 25-fold reduction of the axial diffusion time, equivalent to a 5-fold reduction of the focal volume. However, there is a chance to expect even stronger analysis volume reduction with that method. STED-FCS was also used to investigate the cell membrane architecture at the nanoscale [20]. Single diffusing lipid molecules were detected in nanosized areas in the plasma membrane of living cells. Tuning of the probed area 70-fold below the diffraction barrier reveals that sphingolipids and glycosylphosphatidylinositol-anchored proteins are transiently trapped in cholesterol-mediated molecular complexes dwelling within 20 nm diameter areas. This tunable noninvasive optical recording combined to nanoscale imaging is a powerful new approach to study the dynamics of molecules in living cells.

Even though it provides potentially unlimited resolution, while used in combination with fluorescence correlation spectroscopy STED is not a common tool to study individual molecules at elevated concentrations due to the high laser intensities involved.

1.2.2 Methods using photonic structures

To further enhance the detection, nanofabricated photonic structures viz. Nanofluidic channels and slits , Near-field Scanning optical microscopy (NSOM), zero mode wave guides have been used to perform single molecule experiments. Nanofluidic channels and slits provide moderate observation volume confinement of the order of tens of atto-liters requiring nano- to micromolar concentration for single molecule experiments [1]. Zero mode waveguides have been arguably the most prominent example in this course hence we have dedicated a section (section 1.3) on this to get an elaborated overview of the functioning and applications of ZMWs.

Near-field scanning optical microscope: NSOM

Near-field scanning optical microscopy (NSOM) is based on subwavelength-sized light source that is raster-scanned across a surface at a distance of a few nanometers to image the sample. A standard approach to NSOM probes implements tapered optical signal-mode fibers that are coated with metal. At the apex of the tip, an aperture of nanometer dimension is opened by focused ion beam milling. The nanoaperture at the apex of the tip constrains the illumination along both lateral and longitudinal directions. The light confinement can be used to improve the optical resolution for bioimaging, reaching about 50 nm for imaging on cell membranes [21–23]. Measurements using aperture-based NSOM probes have been reported on lipid bilayers [24], single nuclear pore [25], and intact living cell membranes [26]. These dynamic measurements provide sub-millisecond temporal resolution at spatial resolutions below 100 nm. A bowtie aperture has been used to improve the light throughput, enabling even better spatial and temporal resolution [27]. Another approach uses gold nanoparticles attached to glass tips as NSOM probes [28,29]. Moving one step ahead, the aperture-based and nanoparticle-based NSOM approaches can be combined by carving a resonant antenna tip on the top of a nanoaperture NSOM probe (Fig. 1.3) [8,30,31]. The antenna tip provides a high local field enhancement that suppresses the background from the aperture-based NSOM. The antenna tip can be used to control the fluorescence emission polarization and direction [30]. Maria and group [31] fabricated a NSOM probe with monopole optical antenna tip (Fig.1.3b,c). These probes are reported to image individual antibodies with a resolution of 26 ± 4 nm as well as a resolution of 30 ± 6 nm is obtained to image intact cell membranes in physiological conditions.

NSOM has the drawback of unreliable probe fabrication and complex implementation [1]. The principle has been picked up and led to the development of nanophotonic structures that allow the fabrication and observation of ultra-small volumes in a parallel and reliable fashion [10].

1.3 Plasmonic Nanoapertures: Zero Mode Waveguides (ZMWs)

In 2003, the groups of Harold Craighead and Watt Webb used single nanometric apertures milled in an opaque metallic films to surpass the diffraction limited detection volume barrier [32]. Since then these ZMWs have been fabricated and studied several times using gold, chromium, Aluminum films using different fabrications techniques viz e-beam lithography followed by dry etching or metal lift-off or by Focused Ion beam milling. Waveguides with metal clad has a cutoff wavelength λ_c above which no propagating modes exist inside the waveguide and an evanescent wave is generated at the aperture's entrance. (Figure 1.4c). λ_c is related to the diameter of aperture with the waveguide theory relation: $\lambda_c = 1.7d$, where d is the aperture diameter [1,32]. Owing to the fact that there can not be any propagating mode existance inside these nanometric aperture these are termed as zero-mode waveguides (ZMWs) to emphasize the nature of evanescent wave. For the diameter of 100 nm, a single nanoaperture reduces the diffraction limited confocal volume by three orders of magnitude reaching the detection volume of about 2 attoliters ($10^{-18}L$) [33,34].

These nanoapertures acts as the pinhole directly milled in the sample plane (Figure 1.4a,b). A particularly simple implementation of zero-mode waveguides consists of small holes in a metal film deposited on a microscope cover-slip. In this case, the metal film acts as the cladding, and the contents of the hole compose the core of the waveguide. Millions of such holes can be made on a single coverslip, resulting in massive parallelism. For direct observation of single-molecule enzymatic activity, enzymes can be adsorbed onto the bottom of the

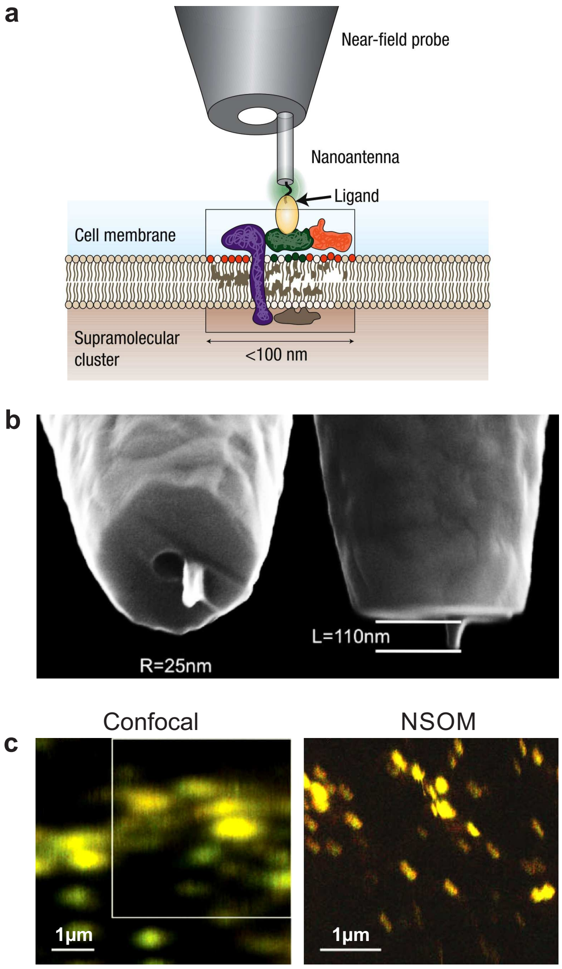

Figure 1.3: (a) Optical antenna carved on top of a NSOM aperture probe. Topography, biochemical recognition and fluorescence images can be recorded simultaneously at nanometre resolution [8]. (b) Scanning electron microscope image of a tip-on-aperture probe [31]. (c) Zoomed-in confocal microscopy image of LFA-1 at the cell surface of monocytes visualized by confocal microscopy (left). The right panel shows the NSOM imaging of the highlighted region in the confocal image [31].

waveguides in the presence of a solution containing the fluorescently tagged ligand molecules. Using a microscope objective the coverslip is illuminated from below and the fluorescence is collected back (Figure 1.4a). These sub-wavelength aperture significantly enhances the detected fluorescence rate per emitter, which increases the signal-to-noise ratio for single molecule detection. It has been shown that in isolated 150 nm diameter apertures milled in aluminum, a 6.5 fold enhancement of the fluorescence rate per molecule was obtained using single rhodamine 6G molecules [33]. Further enhancement up to 25-fold can be obtained by tuning the plasmon properties of nanoapertures [35–38].

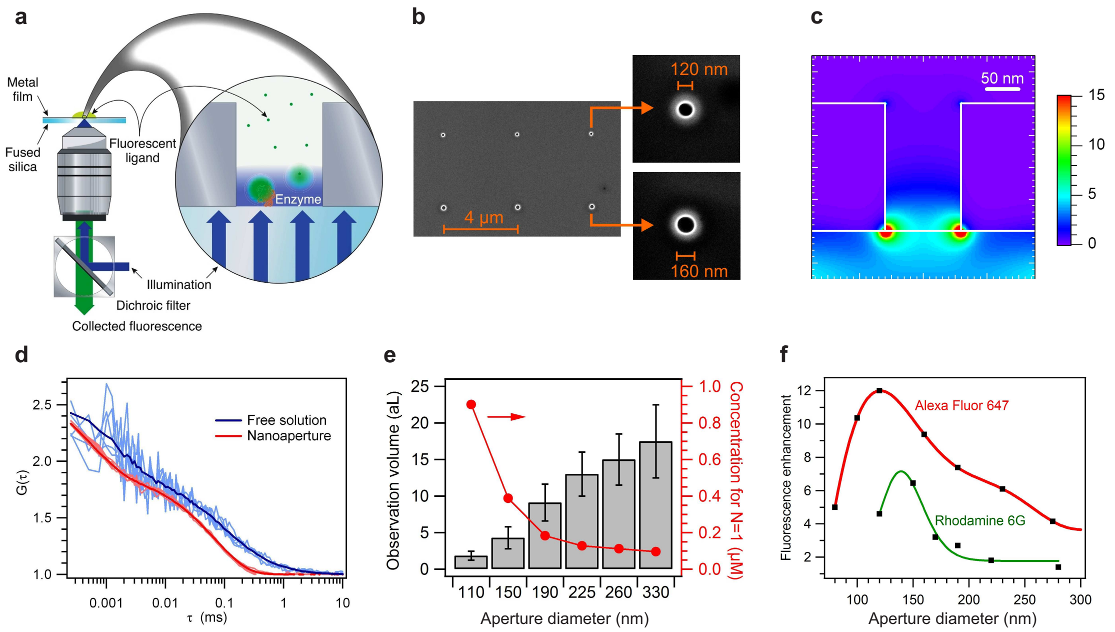

Figure 1.4: Zero Mode waveguides to enhance single molecule fluorescence detection at physiological concentration. (a) Nanoaperture for enhanced single molecule enzymology [32]. (b) Electron Microscope images of 120 and 160 nm apertures milled in gold [36].(c) Field intensity distribution on a 120 nm water-filled gold aperture illuminated at 633 nm [36].(d) Comparison of normalized FCS correlation curves between confocal and nanoapertures configurations [39]. (e) Observation volumes measured for aluminum apertures. The right axis shows the corresponding concentration to ensure there is a single molecule in the observation volume. [33]. (f) Fluorescence Enhancement factor for Alexa Fluor 647 molecules in apertures milled in gold and for Rhodamine 6G molecules in apertures milled in aluminum [35].

Enhanced single molecule detection in solution with ZMWs

A large range of biological processes have been monitored with single molecule resolution at micromolar concentrations using ZMW nanoapertures. Most studies take advantages of fluorescence correlation spectroscopy (FCS) (see chapter 3 for detail of FCS)as a biophotonic method to analyse the fluorescence intensity trace from individual molecules diffusing inside and outside the nanoaperture. Levene and co-workers [32] have effectively shown that arrays of ZMWs provides a highly parallel means for studying single-molecule dynamics at micromolar concentrations with microsecond temporal resolution. They monitored DNA polymerase activity at 10 μM dye concentration with an average of 0.1 molecule inside a 43 nm diameter aperture. However, for the experiments conducted on ultrasmall structures, the signal to noise ratio comes close to one, as a consequence of quenching losses and increased background. This work has led to a number of other applications combining nanometric apertures with single molecule detection. Among them are oligomerization of the bacteriophage λ-repressor protein [2], protein-protein interactions considering the GroEL-GroES complex [40, 41], or observation of flow mixing [42]. The applications can be extended to dual-color cross-correlation

FCCS analysis to monitor DNA enzymatic cleavage at micromolar concentrations with improved accuracy. [43]. To avoid the use of fluorescent labelling, the fluorescence detection technique can be operated in reverse mode: the solvent solution filling the aperture is made highly fluorescent by using a millimolar concentration of small fluorescent molecules. Label-free(non-fluorescent) analytes diffusing into the aperture displace the fluorescent molecules in the solution, leading to a decrease of the detected fluorescence intensity, while analytes diffusing out of the aperture return the fluorescence level [44].

Real time DNA RNA sequencing

A very promising application of nanometric apertures includes real-time single-molecule DNA and RNA sequencing [45–47]. The development of personalized quantitative genomics requires novel methods of DNA sequencing that meet the key requirements of high-throughput, high-accuracy and low operating costs simultaneously. To meet this goal, each nanoaperture forms a nano-observation chamber for watching the activity of a single DNA polymerase enzyme performing DNA sequencing by synthesis (Fig 1.5) [45]. The sequencing method records the temporal order of the enzymatic incorporation of the fluorescent nucleotides into a growing DNA strand replicate. Each nucleotide replication event lasts a few milliseconds, and can be observed in real-time. Currently, over 3000 nanoapertures can be operated simultaneously, allowing massive parallelization.

Live cell membranes investigation at the nanometer scale with ZMWs

Plasma membrane are highly dynamic structures, with key molecular interactions underlying their functionality occurring at nanometre scale. At this resolution it gets challenging to observe these interactions in living cells [48], as standard optical microscopy does not provide enough spatial resolution while electron microscopy lacks temporal dynamics and can not be easily applied to live cells. ZMWs combines with FCS offer the advantages of both high spatial and temporal resolution together with a direct statistical analysis as shown by Moran-Mirbal et al. [48](Fig. 1.6a). They showed that fluorescence from actin-eGFP correlates well with DiI-C12 fluorescence from a cell incubated on ZMW structures, indicating cellular membrane penetration into nanoscale apertures. The nanoaperture works as a pinhole directly located under the cell to restrict the illumination area (Fig. 1.6b). The fluorescent markers labeled into the cell membrane give the dynamic signal while they diffuse, which is analyzed by correlation spectroscopy to extract information about membrane organization (Fig. 1.6c,d) [49–51]. Wenger et al. [52] provided more insight about the membrane organization by performing measurements with increasing diameters. It was shown that fluorescent chimeric ganglioside proteins partition into 30 nm structures inside the cell membrane. Apart from the translational diffusion, the stoichiometry of nicotinic acetylcholine and P2X2 ATP receptors isolated in membrane portions inside zero-mode waveguides was analysed using single-step photobleaching of green fluorescent protein incorporated into individual subunits [53].

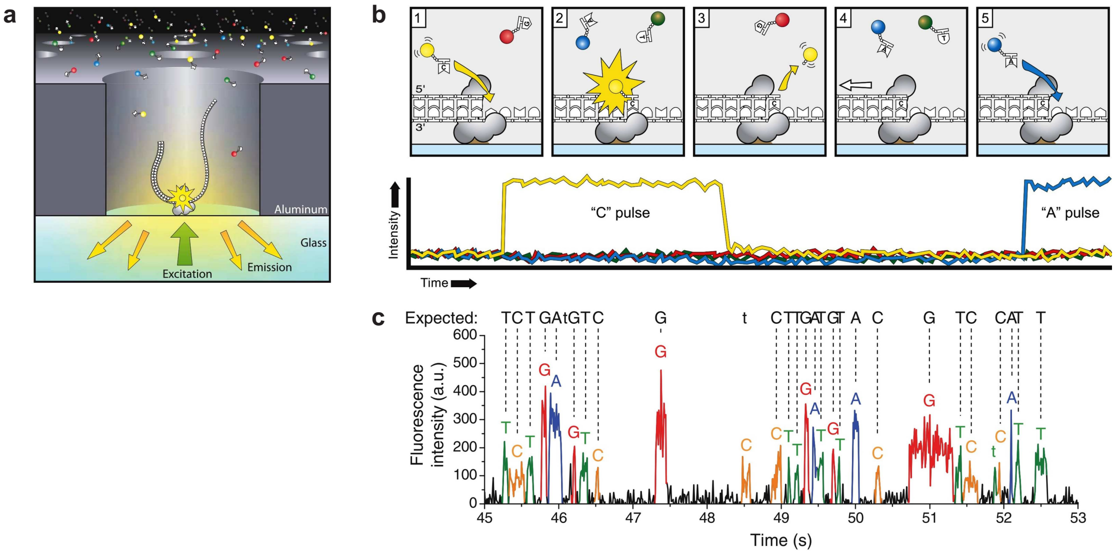

Figure 1.5: Application of zero-mode waveguides to single-molecule real-time DNA sequencing.(a) Principle of the experiment: a single DNA polymerase is immobilized at the bottom of a ZMW, which enables detection of individual phospholinked nucleotide substrates against the bulk solution background as they are incorporated into the DNA strand by the polymerase. (b) Schematic event sequence of the phospholinked dNTP incorporation cycle, the lower trace displays the temporal evolution of the fluorescence intensity. (c) Section of a fluorescence time trace showing 28 incorporations events with four color detection. Pulses correspond to the least-squares fitting decisions of the algorithm [45]

.

Performing live cell investigation requires cell membranes to adhere to the substrate. It depends on the membrane lipidic composition [50], and on actin filaments [48]. To further ease cell adhesion, and avoid membrane invagination issues, planarized 50 nm diameter apertures have been recently introduced [54]. The planarization procedure fills the aperture with fused silica, to achieve no height distinction between the aperture and the surrounding metal.

Plasmonic control of the fluorescence directivity

ZMWs provide a new pathway of directional control on the emitted light by adding concentric surface corrugations (or grooves) (Fig 1.7), while preserving the light localization inside the nanoaperture. Corrugated aperture have been reported to provide high fluorescence enhancement together with beaming of the fluorescence light into narrow cone [56,57]. The fluorescence light from single molecules can thus be efficiently collected with a low numerical aperture objective, releasing the need for complex high numerical aperture objectives. By tuning the geometrical properties of the corrugation design, the fluorescence directionality can be controlled, [55,58] which offers photon sorting abilities from nanoscale volumes. Also,

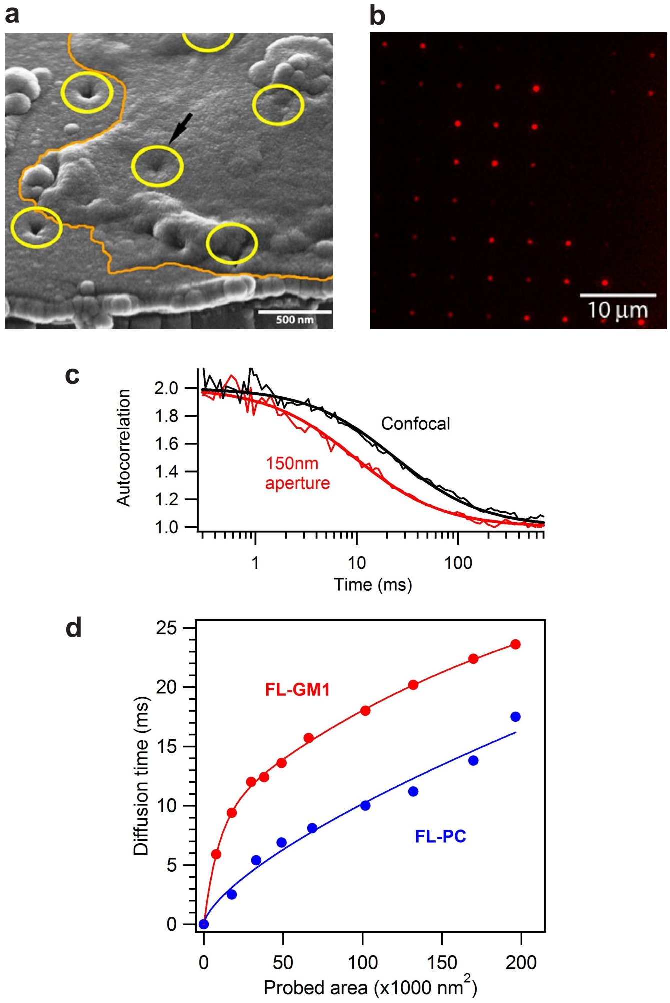

Figure 1.6: Application of zero-mode waveguides to investigate cell membranes below the diffraction limit. (a) Scanning electron microscope image of cross-sectional cuts of nanoapertures. Cell membranes have been outlined (lightgray), and aperture locations have been circled. Cell membrane spanning a nanoaperture dips down (arrow), suggesting membrane invagination. The scale bar is 500 nm [48]. (b) Fluorescence micrographs of cells labelled with DiI-C 12 membrane probe through 280 nm aluminum apertures [48]. (c) Normalized FCS correlation functions and numerical fits (thick lines) obtained for the FL-GM1 ganglioside lipid analog, demonstrating a significant diffusion time reduction in the nanoaperture [52]. (d) Molecular diffusion times versus aperture area for the FL-GM1 ganglioside and FL-PC phosphatidylcholine [52].

to release the need of complex nanofabrication, a new strategy has been presented by Lutz et al. [59], where the shallow grooves are replaced by nanoapertures milled into a regular array. It has been shown that Hexagonal clusters of nanoapertures in a plasmonic film realize a nanoscale phased array antenna to control single-molecule emission. The plasmonic band structure tailors the radiation pattern of localized single emitters in the forward direction along with 40× signal enhancement. The directionality of fluorescence of Alexa 647 dye molecules is

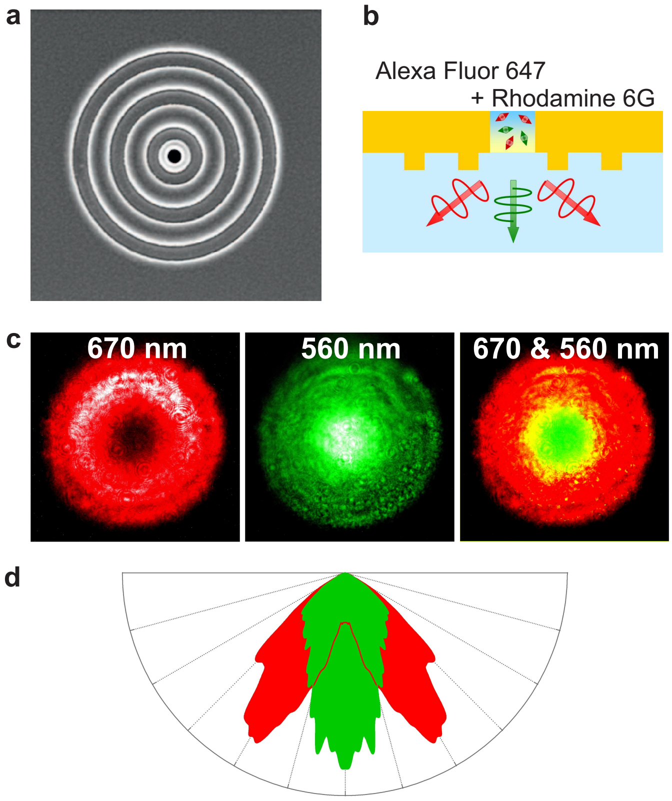

Figure 1.7: Corrugated nanoapertures to control the fluorescence directivity with surface plasmon waves. (a) Scanning electron microscope image of a single aperture of 140 nm diameter milled in gold with two concentric grooves of period 440 nm and depth 65 nm. (b) Sketch of the experiment to illustrate the photon sorting ability: the central aperture is filled with a mixed solution of Alexa Fluor 647 and Rhodamine 6G. (c) Radiation patterns in the back focal plane of the objective for emission centered at 670 nm and 560 nm. (d) Fluorescence radiation pattern for the two different emission wavelengths [55].

mapped in water diffusing through the central single nano-aperture of finite aperture clusters of different size (Fig. 1.8). It has been found that already small lattices with less than 25 unit cells show highly directional emission that is set by the plasmonic crystal band structure (see Fig 1.9).

1.4 Overview of plasmonic antennas under research

Top-down approaches

Top down nanofabrication techniques allow the nano-patterning of plasmonic antenna with improved resolution, throughput and reproducibility. Popular techniques include Electron-

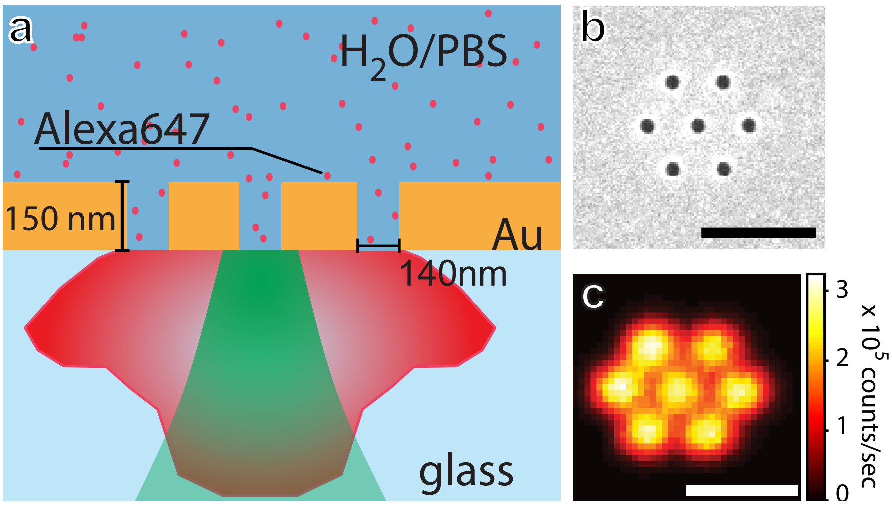

Figure 1.8: (a) Sketch of the sample consisting of a 150 nm thick gold film on glass with apertures of 140 nm diameter at 440 nm pitch. A drop of 1μM solution of Alexa Fluor 647 in a water saline solution is placed on top of the sample. (b) SEM image and (c) confocal fluorescence scan of a hexagonal array consisting of a central hole with one shell of apertures around it. The scale bars corresponds to 1 μm [59].

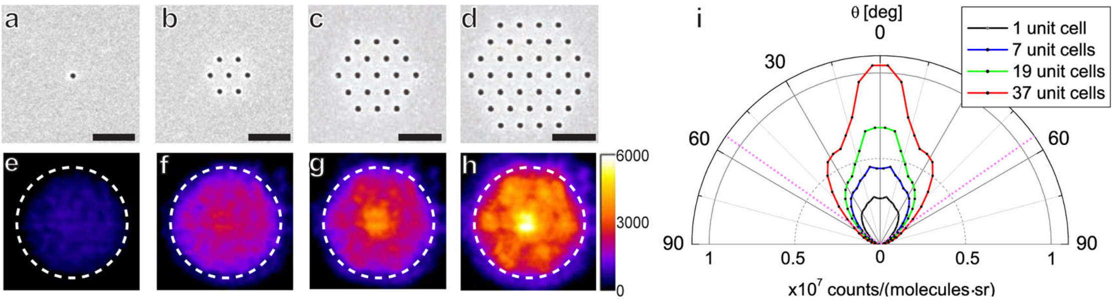

Figure 1.9: (a) Scanning electron micrographs of a single-hole structure and hexagonal clusters with (b) 7, (c) 19, and (d) 37 unit cells(one, two and three shells) around the central aperture (the scale bar is 1 μm). (e-h) Back focal plane (fourier plane) images representing the radiation patterns for the structures in (a)-(d). The point to be noted is that only the central aperture was illuminated by the laser beam in these experiments. The color bar represents a linear scale from 0 to 6000 counts per pixel. (i) Radiated intensity in counts per second per molecule per solid angle for hexagonal lattices of increasing number of apertures. [59].

beam lithography (EBL), Focused ion-beam nanofabrication (FIB), Nano-imprint lithography (NIL) [63, 64]. EBL uses a focused electron beam to pattern on a high-resolution electron-sensitive resist, e.g. PMMA, which is further developed and removed to deposit a desired layer of metal covering both the void and the remaining resist. Finally the lift-off is done with a solvent to remove remaining resist. FIB milling uses accelerated Ga ions focused into a beam with a few nanometer spot and scanned over a conductive substrate to produce a desired pattern. NIL technique is comparatively low-cost and high-throughput and it uses a hard mold that contains all the surface topographic features to be transferred onto the sample and

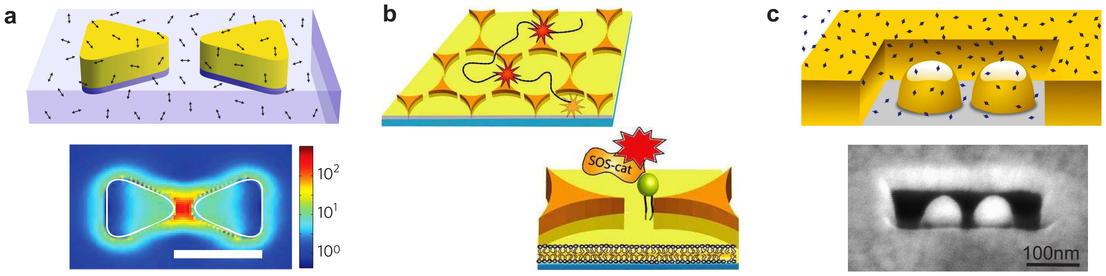

Figure 1.10: Top Down approaches to plasmonic antennas for enhanced single molecule fluorescence. (a) Gold bowtie antenna covered by fluorescent molecules (arrows) in PMMA resin. The lower image shows the computed local intensity enhancement [60]. (b) Plasmonic bowtie antennas surrounded by a fluid supported lipid bilayer, where fluorescently labeled Ras proteins are anchored in the upper leaflet of the lipid membrane. Fluorophores tethered to the supported membrane can diffuse in the plane and thereby pass through the nanogaps [61]. (c) Antenna-in-box platform for single-molecule analysis at high concentrations [62].

pressed under controlled temperature and pressure into a thin polymer film [65].

Bow-tie antenna stands out as an example of top-down approach (Figure 1.10a) [60]. It consists of two facing gold nanotriangles fabricated by electron beam lithography. The strong localized surface plasmon inside the 10 nm gap between the triangles enhances the excitation field around 100 times. Despite non-radiative ohmic losses to the metal, the quantum yield of a near-infrared fluorescent dye is increased by ten times, from 2.5% to about 25%. The gain in local excitation intensity and fluorescence quantum yield combine to reach overall fluorescence enhancement factors per single molecule of three orders of magnitude that come simultaneously with fluorescence lifetime reductions down to 10ps. Experiments to extend FCS towards micromolar concentrations with bowtie antennas have been reported in [66]. The bowtie antenna resonance in the near infrared imposes to use fluorescent dyes that emit into the near IR. For the two fluorophores probed [61], the bowtie-FCS signal was found dominated by molecules that transiently stick to the substrate near the bowtie gap, and by photobleaching/photoblinking dynamics on tens of millisecond time scale, much larger than typical translational diffusion times.

An elegant method to fabricate gold bowtie arrays with well-defined nanometer gaps has been reported by a combination of colloid lithography and plasma processing (Fig. 1.10b). Controlled spacing of the antenna gap is achieved by taking advantage of the melting between polystyrene particles at their contact point during their contact point during plasma processing and using this polymer thread as a mask for gold deposition. A supported lipid membrane can be formed on the intervening substrate by vesicle fusion, and diffusion trajectories of individuals proteins are traced as they sequentially pass through multiple gaps where fluorescence enhancement takes place.

Plasmonic antennas appear as efficient tools to provide large enhancement of the fluorescence excitation and emission rates [28, 29, 60], and direct fluorescence light [30, 67]. However, applications of plasmonic antennas to detect fluorescent molecules in solution of micromolar concentration are challenged by the large contribution in the detected fluorescence intensity from non-enhanced molecules tens of nanometer away from the antenna. In any nanoantenna experiment on molecules in solution, the observed fluorescence signal is a sum of two contributions: the enhanced fluorescence from the few molecules in the antenna gap region (hot spot) superimposed on a potentially large fluorescence background from the several thousands of molecules that are still present within the diffraction-limited confocal volume. To address this challenge, a design termed "antenna-in-box" has been proposed (Fig. 1.10c) [62]. This research work has been done during my Phd project and it will be discussed elaborately in chapter 4.

Bottom-up approaches

Bottom-up approach relies on the intrinsic properties of atoms and molecules to direct their self-organization to create complex shaped nanostructures to match up their complementary top-down approach [68–70]. Owing to their low intrinsic costs they provide a very promising platform for large-scale application of plasmonic nanostructures. As a prominent example of bottom-up nanofabrication, the synthesis of complex shaped metal nanoparticles has received a large attention. Metal nanoparticles are largely available at a low intrinsic cost. They support local surface plasmon resonances that confine and enhance the electromagnetic fields within a few tens of nanometers close to the nanoparticle surface. Moreover, the nanoparticle spectral response can be tuned by selecting appropriate material and shape. In the context of fluorescence applications to detect biomolecules at physiological concentrations, metal nanoparticles appear naturally as an attractive nanodevice to overcome the diffraction limit for the concentration of light (Fig 1.11a) [71–75]. However, as for top-down lithographied plasmonics antennas, the detection of diffusing molecules at micromolar concentration is challenged by the large contribution in the fluorescence signal from unenhanced molecules tens of nanometer away from the nanoparticles [72, 73]. Molecular sticking to the metal may also become an issue to analyse the signal dynamics [71, 74]. These issues can be avoided by using emitters with low quantum yield to take advantage of the higher fluorescence enhancement factors obtained with them [74], or by using a chemical quencher to the solution so as to reduce the fluorophore's quantum yield and maximize the fluorescence enhancement [75]. The use of surfactant and salts in solution was also found to reduce the binding of the molecules to the gold surface [62, 75] (For more details see Chatper 5). It should be noted that significantly higher enhancement factors can be reached by selecting nanoparticles with sharper plasmonic resonances such as nanorods, for which enhancement factors up to 1000 fold have been reported [74]. Additionally, silver nanoisland films prepared by wet chemical synthesis or thermal vapor deposition benefit from simple nanofabrication technique and have been reported to enhance FCS application up to 9 μM concentration [76].

To provide tighter confinement of light and larger fluorescence enhancement factors, nanoantennas can benefit from the electromagnetic coupling between several nanoparticles separated by distances much smaller than the nanoparticles radii (Fig. 1.11e). Gold nanoparticle dimers linked by a single DNA double-strand can be synthesized and filtered using electrophoresis (Fig. 1.11c) [77–79]. The interparticle distance defining the antenna gap is tuned by changing the length of the DNA template, and a binding site to target a single fluorescent molecule can be inserted in the structure. To provide further flexibility in the design of plasmonic antennas, DNA origami is a powerful method to obtain excellent nanofabrication control. Gold nanoparticles with diameters up to 100 nm were attached to DNA origami pillar structures, reaching gaps of 23 nm which also incorporated docking sites for fluorescent molecules (Fig.1.11d) [80]. Thanks for the large scattering cross-section of these antennas and the operation near resonance, a maximum of 117 fold fluorescence enhancement was obtained for a single ATTO647N fluorescent molecule (Fig.1.11f).Thanks to the intensity enhancement introduced by the nanoantenna, single-molecule measurements could be performed at concentrations up to 500 nm, two orders of magnitude higher than conventional measurements [80, 81]. Plasmonic antennas templated with DNA origami open the way for the development of bottom-up inexpensive enhancement chambers for biological assays with single molecule resolution at high physiological concentrations.

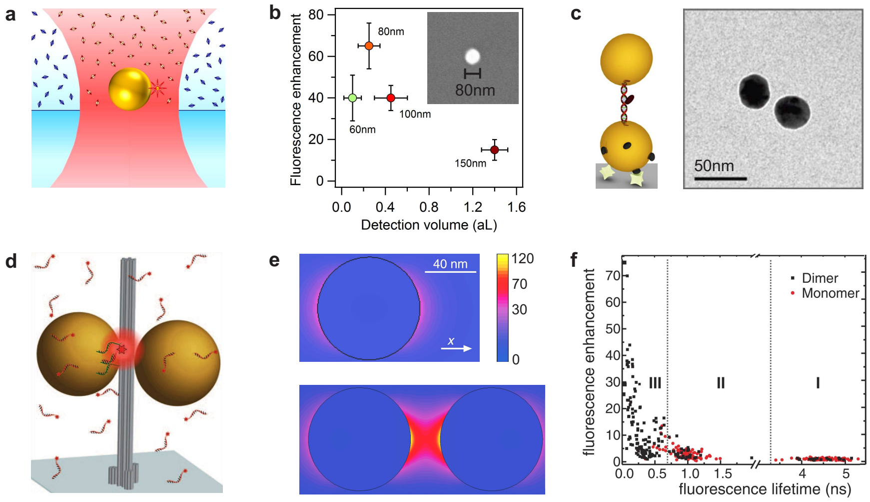

Figure 1.11: Bottom-up approaches to plasmonic antennas for enhanced single molecule fluorescence. (a) A single gold nanoparticle is used as optical antenna [75] (b) Fluorescence enhancement versus the near-field detection volume obtained with single gold nanoparticles, [75] the nanoparticle diameter is annotated close to the data point. (c) Cryo-EM of a plasmonic dimer antenna made of two 40 nm gold particles linked with a 30 base pairs double stranded DNA [77] (d) DNA origami pillar with two gold nanoparticles forming a dimer antenna [82]. Fluorescent labeled ssDNA sequences in solution can transiently hybridize with complimentary sequences in the origami structure at the hotspot between the particles. (e) Numerical simulation of electric field intensity for single and dimer of 80 nm diameter gold particles. The incoming light is horizontally polarized at a wavelength of 640 nm, the gap distance in the dimer is 23 nm [82]. (f) Scatter plot of fluorescence intensity versus lifetime of the ATTO647N-labeled DNA origami pillar with binding sites for one (monomer) and two (dimer) 80-nm diameters particles.

1.5 Conclusion

Monitoring single molecule at the physiologically relevant micromolar concentration regime imposes to rethink the optical microscope apparatus to break the diffraction limit. This difficulty can be accounted as one of the main limitations for the broad applicability of optical single-molecule detection in biology and medicine [8, 10]. The ability to reliably fabricate nanostructrues to confine and enhance the light into nanoscale volumes paves the way to overcome the diffraction challenge, and several methods based on zero-mode waveguides or plasmonic antennas have been reviewed here. Moreover, the plasmonic approach can benefit from other approaches using advanced microscopy techniques [19, 20], dielectric-based antennas [83, 84], microfluidics [85, 86], or optical fibre probes [87–89]. All these techniques, and their combination, significantly expand the single molecule toolbox. The application to biological problems is an emerging and exciting field, which is promising to reveal new insights on biological functions and dynamics.

2 Light matter interaction at nanoscale

Light matter interaction relies on the coupling between the single quantum emitters (fluorescent molecules, quantum dots) and the desired mode of radiation field [12]. These emitters have dimension very small compared to the wavelength and that is why they can be considered to be behaving like electric dipole [13]. And at nanoscale the transition between emitters and the radiation field has taken a great deal of advantage from plasmonics to exploit the unique optical properties of metallic nanostructures to confine light at nanometric regime. [14].

In practice to enhance the coupling between an optical emitter and a desired mode of radiation field, two approaches can be used. One strategy is to increase the lifetime of the confined optical excitation in high-Quality Factor(Q) dielectric resonators, such as whispering gallery structures, micropillars, and photonic crystals. Another strategy is to reduce the effective mode volume (V_{eff}) of the confined radiation, as is currently explored by using plasmonic nanostructures capable of confining light to dimensions well below the diffraction limit [12]. In first case the key property of a microcavity is the possibility of achieving quality factors as large as 10^6 by using lossless materials but the volume confinement is limited to approximately $(\lambda/2n)^3$ owing to the fact that only propagating waves are used , here "n" is the refractive index of the medium. In second case the nanoantennas have advantages in having large volume confinement due to evanescent waves which compensates the low Q value of Localized surface plasmon resonance (LSPR) $100-1000$ and that provides nanoantennas advantage of having a large purcell factor [90]. The excitation of plasmon resonances in these structures, which act as optical nanoantennas, leads to highly localized photon fields and therefore to an enhancement of the excitation as well as of the radiative and nonradiative decay rates of nearby emitters [91].

In this chapter first we will discuss the optical properties of bulk noble metals based on Drude model. These properties are fundamentally important for dealing with the complex optical phenomena of metallic nanoantennas. Then we will go through the basics of localized surface plasmon resonance conditions that drives nanoantennas to localize the photon field in nanometric regime. In the next section we discuss about the optical antennas and how the radiative properties of emitter can be drastically modified by the presence of a nanoantenna. And finally we briefly go through some prominent applications of optical nanoantenna.

2.1 Optical properties of bulk metals

Optical antennas use metals like aluminum, gold and silver which are characterized by high electrical and thermal conductivity with high reflectivity in the visible spectral range. The linear responses of metals to electromagnetic waves are described by their complex dielectric function $\epsilon(\omega) or \epsilon = \epsilon_1(\omega) + i\epsilon_2(\omega)$, at frequency ω. For noble metals such as gold and silver, the valence bands are completely filled and ϵ is mainly governed by the electron transitions within the partially filled conduction bands. However, in the energy range where interband transitions occur, the contribution of electrons from deep levels has also to be taken into account [92].

2.1.1 Dielectric functions of free electron metals

The dielectric functions of free-electron metals are described by the Drude-Lorentz-Sommerfeld model [93] in which the macroscopic response of the metal is determined by multiplying the effect of a single free electron to the external force by the number of electrons. The response of a free electron of mass m_e and charge e to an external electric field $\mathbf{E} = \mathbf{E_0} e^{i\omega t}$ can be described by the equation [94]:

$$m_e \frac{\partial^2 r}{\partial t^2} + m_e \gamma \frac{\partial r}{\partial t} = -e\mathbf{E} \tag{2.1}$$

with a solution

$$r(t) = \frac{e}{m_e(\omega^2 + i\gamma\omega)}\mathbf{E} \tag{2.2}$$

where $\gamma = 1/\tau$ denotes the damping constant having τ as the relaxation time of the free electron gas. Eq. 2.2 gives the induced dipole moment of a free electron $\mathbf{p} = e\mathbf{r}$ and the polarization $\mathbf{P} = n\mathbf{p}$, n is the number of electrons per unit volume. From here it follows for the dielectric displacement and dielectric constant:

$$\mathbf{D} = \epsilon_0 \mathbf{E} + \mathbf{P} = \epsilon_0 \epsilon \mathbf{E} = \epsilon_0 \left(1 - \frac{\omega_p^2}{\omega^2 + i\gamma\omega}\right)\mathbf{E} \tag{2.3}$$

We get the dielectric function of the metal as

$$\epsilon(\omega) = 1 - \frac{\omega_p^2}{\omega^2 + i\gamma\omega} \tag{2.4}$$

where $\omega_p = ne^2/(\epsilon_0 m_e)$ is the plasma frequency of the free electron gas that increases with increasing carrier density [94,95]. For noble metals at optical frequencies, typically $\omega < \omega_P$ and therefore this model accounts for (i) a negative real part, meaning that the conduction electrons do not oscillate in phase with the external field, which is the reason for high reflectivity of metal surfaces, and (ii) a significant imaginary part.

2.1.2 Interband transitions

For noble metals such as gold and silver, the electrons in deeper levels contribute to their dielectric function as well and the Drude-Sommerfeld model does not account for the possibility that photons with high-enough energy cause interband transitions by promoting electrons from lower lying valence bands to higher energy conduction bands [64]. This further degree of freedom is related to bound electrons and can be classically described by a collection of damped harmonic oscillators with well defined resonance frequencies ω_0, yielding contributions to the dielectric response of the type

$$\epsilon_{interband}(\omega) = 1 + \frac{\tilde{\omega}_p^2}{(\omega_0^2 - \omega^2) - i\tilde{\gamma}\omega} \tag{2.5}$$

where $\tilde{\omega_p}$ depends on the density of bound electrons involved in the absorption process and $\tilde{\gamma}$ is a damping constant for the bound electrons. This absorption channel leads to a strong deviation from the free electron gas model near ω_0, leading to a maximum in the imaginary part of $\epsilon(\omega)$ and therefore to strongly increased damping (see Figure 2.1). [64]

2.1.3 Skin depth of metals

The dielectric function is directly linked to the complex refractive index as:

$$n(\omega) = n_r(\omega) + i\kappa(\omega) = \sqrt{\epsilon_1 + i\epsilon_2}, \tag{2.6}$$

The damping of an electromagnetic wave in the direction of propagation is described by the imaginary park κ and on a metal surface it has a finite penetration depth due to energy dissipation. To explain this using dielectric functions the electric field in x direction can be written as

$$\mathbf{E} = \mathbf{E_0} e^{i(\mathbf{kx} - \omega t)}, \tag{2.7}$$

where $\mathbf{k}$ is the wave vector inside metal with magnitude $|\mathbf{k}| = (\omega / c)(n_r + i\kappa)$ and c is the light velocity in vacuum. Thus, the electric field within the metal can be rewritten as

$$\mathbf{E} = \mathbf{E_0} e^{i\omega(xn_r/c - t)} e^{-x/\delta}, \tag{2.8}$$

where,

$$\delta = \frac{c}{\omega\kappa} = \frac{\lambda}{2\pi\kappa} \tag{2.9}$$

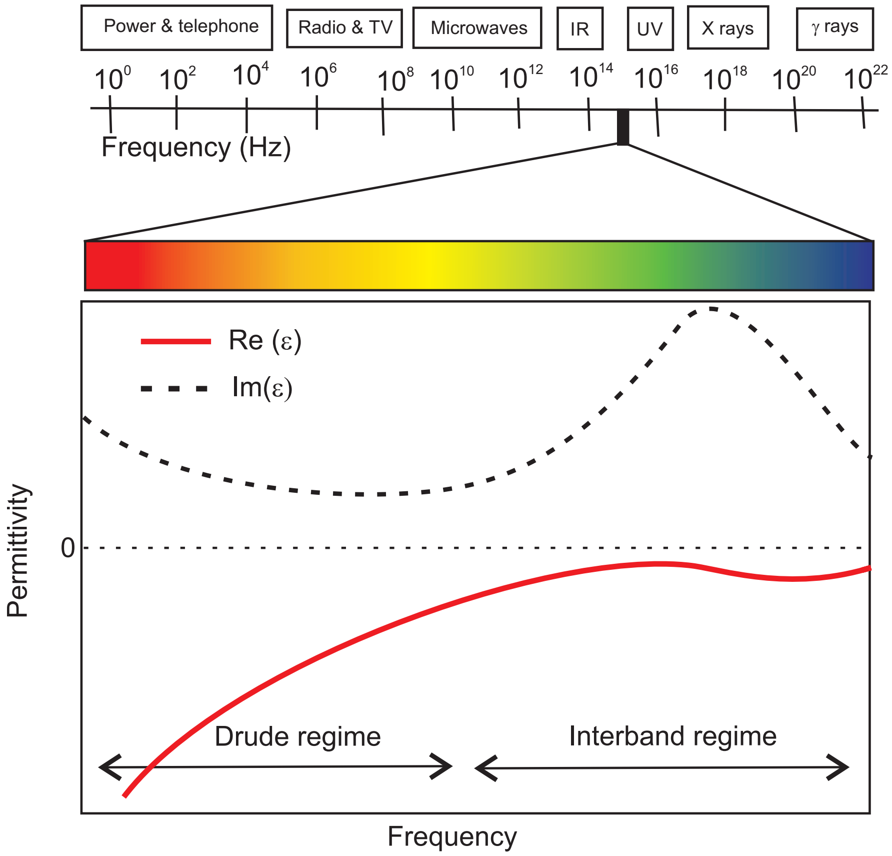

Figure 2.1: Figure shows a small part of the entire EM spectrum which represents a typical dielectric function of a metal at optical frequencies (top). An interband-transition peak, visible in the imaginary part of $\epsilon(\omega)$, is superimposed onto the monotonic Drude-like behavior of the free electron gas [64].

is the skin depth, which gives the idea about the attenuation of electric field in metal. From Eq. 2.6 we can deduce the value of κ as

$$\kappa = \sqrt{-\frac{\epsilon_1}{2} + \frac{1}{2}\sqrt{\epsilon_1^2 + \epsilon_2^2}} \tag{2.10}$$

Metals are generally characterized by large values of κ in the optical regime, and the electromagnetic waves are strongly damped within several tens of nanometers inside the metal. For example, gold and silver have skin depths of 31 nm and 24 nm, respectively, for a photon energy of 2 eV (620 nm) [93].

2.2 Localized surface plasmon polariton

Optical antennas are basically driven by localized surface plasmon-polariton resonance (LSPR) [96], which is generated by the collective oscillation of free electrons in metals coupled to the electromagnetic field.

The interaction of a metal particle having size d with the electromagnetic field can be analyzed using the simple quasi-static approximation provided that the particle is much smaller than the wavelength of the light ($d << \lambda$). This gives the opportunity to treat the phase of the harmonically oscillating electromagnetic field, constant compared to the particle volume, so that one can calculate the spatial field distribution by assuming the simplified problem of a particle in an electrostatic field. And once the field distribution are known the harmonic time dependence can be added afterwards. We consider a homogenous, isotropic sphere of radius a at origin in a uniform static electric field $\mathbf{E} = E_0\hat{\mathbf{z}}$ (Fig.2.2). $\epsilon(\omega)$ is the complex dielectric function of the sphere (ϵ) and ϵ_m is the dielectric constant of the isotropic and non-absorbing surrounding medium. Now we calculate the electric field $\mathbf{E} = -\nabla\phi$ by solving the Laplace equation for the potential, $\nabla^2\phi = 0$.

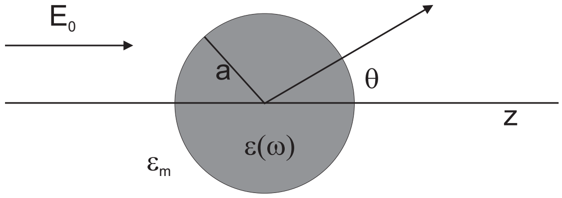

Figure 2.2: Schematic of a homogeneous sphere placed into an electrostatic field (Adapted from [94]).

In spherical coordinates, the Laplace equation is of the form

$$\frac{1}{r^2 sin\theta}\left[sin\theta\partial_r(r^2\partial_r) + \partial_\theta(sin\theta\partial_\theta) + \frac{1}{sin\theta}\partial_\phi^2\right]\Phi(r,\theta,\phi) = 0 \tag{2.11}$$

Due to the azimuthal symmetry, the general solution of Eq.2.11 is independent of ϕ and has the form [94, 97]

$$\Phi_{in}(r,\theta) = \sum_{l=0}^{\infty} A_l r^l P_l(cos\theta) \tag{2.12}$$

$$\Phi_{out}(r,\theta) = \sum_{l=0}^{\infty}(B_l r^l + C_l r^{-l-1})P_l(cos\theta) \tag{2.13}$$

where, Φ_{in} is the potential inside the sphere and $\Phi_{out} = \Phi_0 + \Phi_{scatter}$ is the potential outside consisting of an incoming and a scattered part.

When applying the boundary conditions at the interface $r = a$ for tangential part of the electric field and for the normal (longitudinal) part of the displacement field [94, 97], the potentials evaluate to

$$\begin{aligned}
\Phi_{in}(r,\theta) &= -\frac{3\epsilon_m}{\epsilon + 2\epsilon_m} E_0 r cos\theta && (2.14)\\
\Phi_{out}(r,\theta) &= -E_0 r cos\theta + \frac{\epsilon - \epsilon_m}{\epsilon + 2\epsilon_m} E_0 a^3 \frac{cos\theta}{r^2} && (2.15)\\
&= -E_0 r cos\theta + \frac{\mathbf{p} \cdot \mathbf{r}}{4\pi\epsilon_0\epsilon_m r^3} && (2.16)\\
with & \\
\mathbf{p} &= 4\pi\epsilon_0\epsilon_m a^3 \frac{\epsilon - \epsilon_m}{\epsilon + 2\epsilon_m} \mathbf{E_0} && (2.17)
\end{aligned}$$

Here the dipole moment **p** is induced in the sphere by the external field and it is proportional to $|E_0|$. Now we can derive the polarizability α_0 using the equation $\mathbf{p} = \epsilon_0\epsilon_m\alpha_0 E_0$ as

$$\alpha_0 = 4\pi\epsilon_0\epsilon_m a^3 \frac{\epsilon - \epsilon_m}{\epsilon + 2\epsilon_m} \tag{2.18}$$

The equation (2.18) takes the Clausius-Mossoti form [97] and provides the complex polarizability of a sub-wavelength diameter sphere in electrostatic field approximation (quasistatic approximation).

The energy conservation law for a single particle is written as

$$\sigma_{ext} = \sigma_{abs} + \sigma_{scat} \tag{2.19}$$

where $\sigma_{ext}, \sigma_{abs}\ and\ \sigma_{scat}$ are the extinction, absorption and scattering cross sections, respectively. When the polarizability α_0 of the nanoparticle is used in the dipolar approximation, the scattering, extinction and absorption cross-sections of the nanoparticles can be obtained as following expression [98]

$$\begin{aligned}
\sigma_{scat} &= \frac{k^4}{6\pi\epsilon_0^2\epsilon_m^2} |\alpha(\omega)|^2 && (2.20)\\
\sigma_{ext} &= \frac{-k}{\epsilon_0\epsilon_m} Im(\alpha(\omega)) && (2.21)\\
\sigma_{abs} &= \sigma_{ext} - \sigma_{scat} && (2.22)
\end{aligned}$$

where k is the wave number in the medium surrounding the nanoparticle. When the quasistatic expression (eq. 2.18) for the polarizability is used, a problem with the energy conservation law (eq. 2.19) is encountered (For more details refer [99]) and this can be overcome by considering a slight modification of the polarizability (eq. 2.18) by including an imaginary term which takes into account the radiation damping [99–102]:

$$\alpha^{-1} = \alpha_0^{-1} - i\frac{k^3}{6\pi} \tag{2.23}$$

This value of polrizability satisfies the energy conservation law (eq. 2.19) for lossless particles [99]. There are some authors who use this expression for lossy nanospheres as well [100, 103, 104].

Now from the expression 2.18, it is apparent that the polarizability experiences a resonant enhancement for minimum $|\epsilon + 2\epsilon_m|$ and by considering the slowly-varying $Im[\epsilon]$ [94], it gives us the Fröhlich condition.

$$Re[\epsilon(\omega)] = -2\epsilon_m \tag{2.24}$$

In the quasistatic approximation, for metal nanoparticles both absorption and scattering (and thus extinction) are resonantly enhanced at the LSPR of the dipole particle i.e. when the Fröhlich condition (equation 2.24) is met [94].

2.3 Optical antennas

Optical antenna enhances the coupling between the radiation field and the single quantum emitter. As the analogy of radio antenna which were developed for communication problem, optical antenna invention is inspired by microscopy. It is defined as a device designed to efficiently convert free-propagating optical radiation to localized energy and vice versa [105] as shown in Fig 2.3.

To design an antenna the constricted electron gas needed is provided by metals. Moreover, metals do not behave as perfect conductors at optical frequencies. For optical antennas the metals are chosen based on their low Ohmic losses. Material losses in metal nanostructures can be kept low either by choosing a metal with large(negative real part of the complex dielectric function, $\epsilon(\omega)$, or by selecting a low imaginary part of $\epsilon(\omega)$ [64]. The choice of materials for plasmonic antennas for particular applications are still a great deal for research. Among all the metals silver and gold are the two mostly used due to their relatively low loss in the visible and NIR ranges. So far almost all the significant research on optical antennas have used silver or gold [106]. Copper has the second-best conductivity among metals next to silver, it is expected to get promising antenna structures based on copper, but due to the fact that fabrications of coppper nanostructures are very challenging as it oxidises very easily they don't serve the

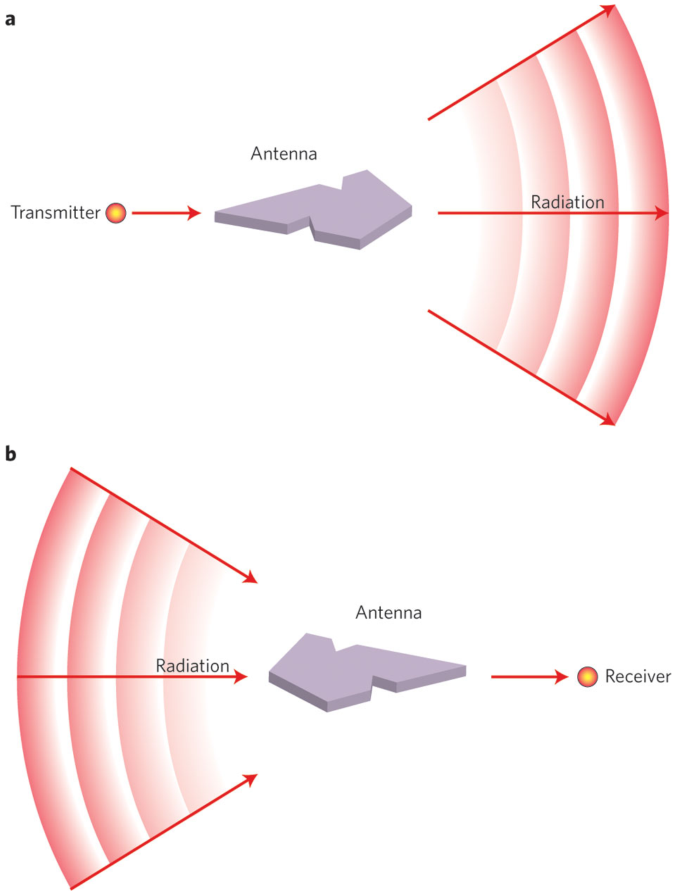

Figure 2.3: Antenna design. a, Transmitting antenna. b, Receiving antenna. Arrows indicate the direction of energy flow. The two configurations are related by the principle of reciprocity. In spectroscopy and microscopy, the two antenna concepts are combined; that is, the antenna is used both as a receiver and as a transmitter [105].

purpose.

2.3.1 Field enhancement

The excitation field can be increased by placing the emitter near the nanoantenna which modifies the electric field environment of the emitter. Earlier works based on the polarizability models have indicated the local surface plasmon resonance (LSPR) and the lightening rod effects, as the two electromagnetic field enhancement mechanisms. The latter can be explained on the basis that there is an increase in surface charge density σ, with the curvature of a metal surface. Since the near field is directly proportional to σ, nanostructures with sharp tips shows more field enhancements. Other methods to enhance the field include the exploitation of nanogaps between the two nanoparticles , the suppression of radiative broadening and the choice of different metals. With the availability of computational methods these basic design concepts have been studied and applied with more efficiency [107].

2.3.2 Decay rates emission close to a nanoantenna

Since the pioneering work of Purcell [108], it is well known that the lifetime of an excited atomic state is not only a function of the atom but also of its environment. Purcell's prediction has been verified in different experimental settings such as close to plane interfaces, in cavities and photonic crystals, and close to near- field optical probes. It was realized that the modification of the lifetime is influenced by the radiative decay rate due to photon emission and by the nonradiative decay rate due to energy dissipation in the environment. For atoms or molecules close to metal surfaces both rates can be enhanced. [28].

The local electromagnetic environment around the emitter influences the spontaneous emission (SE) rate. To model the decay rate of the single fluorescent emitter we use the simplest classical Lorentz harmonic oscillator [109], where the transition dipole moment induced in a weakly excited (below saturation) quantum emitter is modeled by a classical electric dipole, **p** having equation of motion as [110]:

$$\frac{d^2\mathbf{p}}{dt^2}+\omega_0^2\mathbf{p}+\Gamma_0\frac{du}{dt}=\frac{e^2}{m}[\mathbf{p}*E_{loc}]\frac{\mathbf{p}}{\mathbf{p}^2} \tag{2.25}$$

where ω_0 and $\Gamma_0(=1/\tau_0)$ are the resonant frequency and the decay rate (inverse of the lifetime) of the emitter in the absence of any excitation. Right hand side of Eq. 2.25 gives the account of interaction between the dipole and the local electric field E_{loc}, projected along the dipole axis and evaluated at the position of the emitter [111]. Now this electric field can be any external illumination or in the absence of that it can be the field emitted by the dipole itself, which is then backscattered by the surrounding medium. The presence of this term opens the way to manipulate the surrounding of dipole using metallic nanostructures.

In order to measure the efficiency of the emitter in the presence of metallic nanostructures, first the intrinsic quantum yield of the emitter is introduced, which depends on the two decay channels, radiative decay rate (Γ_{r0}) and non-radiative decay rate (Γ_{nr0}), as

$$\phi_0=\frac{\Gamma_{r0}}{\Gamma_{r0}+\Gamma_{nr0}} \tag{2.26}$$

And the effect of nanostructure modifies this quantum yield as

$$\phi=\frac{\Gamma_r}{\Gamma}=\frac{\Gamma_r}{\Gamma_r+\Gamma_{nr}+\Gamma_{nr0}} \tag{2.27}$$

where $\Gamma=1/\tau$ is the total decay rate and τ is the transition lifetime. We now see three different decay channels in the system, the radiative rate, Γ_r, the nonradiative rate due to metallic losses, Γ_{nr} and the intrinsic nonradiative rate to emitter, Γ_{nr0} [110, 111].

By considering the emitter as a quantum entity, the decay rate associated with the spontaneous emission process between two molecular energy states can be given by the

Fermi's golden rule,

$$\Gamma = \frac{2\pi}{\hbar^2}|M_{if}|^2\rho(\omega), \tag{2.28}$$

where M_{if} is the transition-matrix element between the initial, $\langle i|$, and final, $|f\rangle$, molecular states and $\rho(\omega)$ is the photonic local density of states (LDOS) and its been noted earlier that the environment of an emitter can modify the LDOS and therefore its emission properties. Now we will compare the two situations, first when the emitter is in free space and second in the presence of a nanostructure.

In free space, without any preferred dipole direction and without any incident field, the transition-matrix element averaged over all direction can be given by $|M_{if}|^2 = |\mathbf{p}|^2\hbar\omega/6\epsilon_0$, where $\mathbf{p} = -e\langle i|\, r\, |f\rangle$ is the dipole moment associated with the electronic transition. LDOS in free space is given as $\rho(\omega) = \omega^2/(\pi^2 c^3)$ [112], using this in Eq 2.28 we obtain the decay rate of an emitter in free space

$$\Gamma = \frac{|\,\mathbf{p}|^2\omega^3}{3\pi\epsilon_0\hbar c^3}, \tag{2.29}$$

In the presence of a metallic nanoantenna, $\rho(\omega)$ will be strongly altered. In 1946, Purcell, in his landmark letter [108] introduced the quality factor Q and the mode volume V, to quantify the modification in spontaneous decay due to the coupling of an emitter with a cavity in the weak coupling regime. The purcell factor, F, is given by [108, 113]

$$F = \frac{3}{4\pi^2}\left(\frac{\lambda_{res}}{n}\right)^3\frac{Q}{V} \tag{2.30}$$

Purcell Factor is being used as a quantitative figure of merit for high Q lossless cavities. Motivated by this, several works have been done to access the possibility of finding a generalized Purcell formula that are valid for any nanostructures with radiative losses, absorption including the special case of plasmonic nanoantennas [113, 114]. To further gain the knowledge about this I would refer to the work done by Sauvan et.al. [113]. In this paper they have shown an elegant theory of coupling between dipole emitters and dissipative nanoresonators.

2.3.3 Optical antenna design rules

The key design principles for achieving a strong modification of the spontaneous emission(SE) rate with minimal suffering of Γ_{nr} can be briefly summarized in following points [115]. (1) The geometry of Optical antenna should be tailored in such a way that SPP resonance lies in the spectral region that minimizes the dissipation in metal. (2) Elongated objects should be preferred over spherical ones to get benefitted from strong near field at sharp corners. (3) The adjustment of the emitter orientation can be done according to the electric dipole moment of the antenna. (4) Ensure that the antenna higher order SPP modes are spectrally separated from the dipolar one. (5) The antenna volume should be chosen properly to get the radiation stronger than absorption.

2.4 Applications of optical antennas

Optical antennas provide a rich control over light at nanoscale to provide high field enhancement and localization with a large absorption cross-sections. Considering the need for these virtues in broad range of fields we highlight the possible applications in this section which includes antennas for spectroscopy, photovoltaics, single photon sources, biological sensing.

Spectroscopy

Nanoantenna can cover broad spectral range, metal nanoantennas are particularly suitable for room-temperature single molecule studies. The metal-enhanced spectroscopies can include the improvement of fluorescence, Raman, Infrared vibrational and non-linear spectroscopies.

Nanoscale imaging

The ability of Optical antennas to manipulate light on the nanometer scale leads naturally to nanoimaging applications. In this context the antenna represents a near-field optical probe used to be guided over an unknown sample surface in close proximity to detect an optical response(scattering, fluorescence) for each image pixel. In general, a near-field image recorded in this way renders the spatial distribution of the antenna–sample interaction strength, and not the properties of the sample. It is possible, however, to write the interaction between antenna and sample as a series of interaction orders [116], and in many cases it is legitimate to retain only a single dominant term. For example, in scattering- based near-field microscopy, the antenna acts as a local perturbation that scatters away the field near the sample surface. Therefore, the antenna–sample interaction can be largely neglected. At the other extreme, in tip-enhanced near-field optical microscopy, the sample interacts predominantly with the locally enhanced antenna field, and the external irradiation can be largely ignored. In this regime the optical antenna acts as a nanoscale flashlight [117] that can be used to perform local spectroscopy.

Photodetectors and Photovoltaic

The traditional approach to photovoltaics is to use light for generating charge carriers in a semiconductor. The spatial separation of the charge carriers defines a current in an external circuit. For maximum efficiency it is important to absorb most of the incoming radiation, necessitating a minimum material thickness, which forms the primary cost determinant. Local field enhancement due to optical antenna can focus the incident light to weakly-absorbing materials such as thin-film photovoltaics. In a photodetector, reducing the active material volume [118] allows for faster speed due to improved carrier collection properties of optical antennas.

Antennas for single-photon sources

Optical antennas have potential to enhance the emission rates and achieve miniaturization to get ultrabright single photon sources, which is required for high-speed quantum communications and quantum computation applications [119]. When the emitter is placed in a 'hot spot' of a resonant optical antenna most of the single emitter decay processes will not generate a free propagating photon but will rather create a single plasmon in the resonant mode of the antenna. Upon radiative decay of these plasmons, single propagating photons are created that bear the properties of the antenna resonance, e.g. its resonance spectrum, polarization and emission pattern [64] . It provides the possibility to build single-photon sources [120] with well-defined polarization, optimized radiation patterns and several thousand times enhanced emission rates [64] by carefully adjusting the position of the emitter to avoid quenching.

In conclusion, optical antennas are trending as attractive optical element to manipulate and control light-matter interaction at the single-emitter level reaching nanoscale resolution in a variety of innovative ways, giving them the potential to be used in a broad range of research.

3 Experimental techniques

The properties of fluorescence emission of a fluorophore, depend on the local environment. In order to enhance the fluorescence signal, the process of tailoring the local environment can be very useful. In particular, the emission of fluorescence from a molecule can be greatly enhanced near nanoantenna's plasmonic environment. The physical origin of this enhancement due to antenna, lies in the changes of electromagnetic environment by enhancing the excitation intensity and/or by tailoring the radiation pattern and/or by increasing the radiative rate transmission from the emitter. These changes depend heavily on the sizes, shapes and types of nanoantennas studied. For this reason, the complete experimental characterization of interactions between nano-objects and fluorescent molecules, and more generally the study of light-matter interactions at the nanoscale, is a topic of great interest for more than a decade [121–124]. However, the determination of the influence of different physical changes created by the antenna is not that trivial, because the enhancement of fluorescence measured is an intricate combination of the enhancements in excitation intensity and the emission intensity of the molecules.

In this chapter, we present the experimental procedures for fluorescence characterization developed within our laboratory, which comprises combining the studies of fluorescence correlation spectroscopy and the measurements of fluorescence lifetime. This procedure allows to discriminate the relative excitation and emission gains contributing to the overall enhancement of fluorescence. We mention in the last section that using a low quantum yield effect provides a better fluorescence enhancement effect.

3.1 Fluorescence Correlation Spectroscopy (FCS)

The ability to track a chemical reaction on the scale of a single molecule gives access to information hidden in the overall averages of thousands of molecules. Among the many existing techniques based on the contrast of fluorescence, fluorescence correlation spectroscopy (FCS), introduced in 1972 by Madge, Elson and Webb [125], is probably the most effective method of high resolution spatial and temporal analysis of extremely low concentrated biomolecules [126]. Unlike other methods of fluorescence, in FCS the first parameter of interest is not the mean fluorescence intensity itself, but rather the temporal fluctuations in fluorescence intensity. These fluctuations appear predominantly as the translational diffusion of molecules through the focal point of excitation laser providing information about the translation diffusion coefficient and the average number of molecules in the observation volume(Fig 3.1).

However, the amount of information available in FCS is not limited to the diffusion coefficients and local concentration of molecules. A large range of processes, including the time characteristics extending from nanosecond to the second, can be studied (molecular brightness, confined and anomalous diffusion, determination of various molecular interactions, conformational changes, etc [126]).

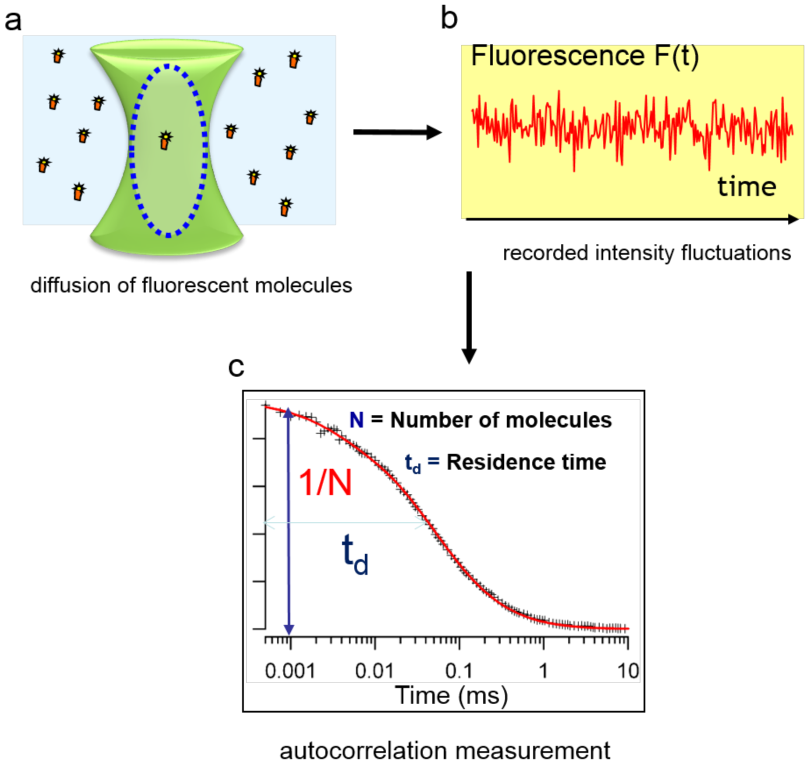

Figure 3.1: Schematic diagram of FCS processes. The diffusion of molecules inside the detection volume (a) are measured as intensity fluctuation (b) and autocorrelated (c) to quantify the number of molecules and diffusion time.

To detect a particular species of fluorescent particle, autocorrelation analysis is performed. Fluorescence intensity signal fluctuations are quantified by temporally autocorrelating the recorded intensity signal. It provides the self-similarity of a time signal and highlights characteristic time constants of the underlying processes [126].

The number of molecules within the focal volume at any time is governed by Poissonian distribution. On that basis the root mean square fluctuation of the particle number N is given by

$$\frac{\sqrt{\langle(\delta N)^2\rangle}}{\langle N\rangle} = \frac{\sqrt{\langle(N-\langle N\rangle)^2\rangle}}{\langle N\rangle} = \frac{1}{\sqrt{\langle N\rangle}} \tag{3.1}$$

The fluorescence signal emitted by the molecules in focal volume is recorded photon by photon. Assuming constant excitation power, the fluctuations of the fluorescence signal are defined as the deviations from the temporal average of the signal:

$$\delta F(t) = F(t) - \langle F(t)\rangle \tag{3.2}$$

where $\langle F(t)\rangle = \frac{1}{T}\int_0^T F(t)dt$ is the temporal average over time T.

By considering that all the fluctuations arise only from changes in the local concentration ∂C inside the effective focal volume V_{eff}, the variation can be written as

$$\delta F(t) = \kappa \int_V I_{ex}(\bar{r}).S(\bar{r}).\delta(\sigma.q.C(\bar{r},t)).dV \tag{3.3}$$

The parameters involved here are basically describing the probability of exciting a fluorophore inside the focal spot and detecting the emitted fluorescence photon due to the final detection efficiency of the setup

κ : overall detection efficiency
$I_{ex}(r)$: spatial distribution of the excitation energy with the maximum amplitude I_0
$S(r)$: optical transfer function of the objective pinhole combination. This determines the spatial collection efficiency of the setup and it is a dimensionless quantity
$\delta(\sigma.q.C(\bar{r},t))$: dynamics of the fluorophore on the single-particle level
    $\delta\sigma$: = fluctuations in the molecular absorption cross-section
    δq : = fluctuation in quantum yield
    $\delta C(\bar{r},t)$: = fluctuation in the local concentration at time t.

Equation 3.3 can be further simplified by combining the convolution factor of the two dimensionless spatial optical transfer functions $I_{ex}(\bar{r})/I_0 * S(\bar{r})$ into a single function

$$W(\bar{r}) = e^{-2(x^2+y^2)/(r_0^2)}.e^{-2(x^2)/(z_0^2)} \tag{3.4}$$

It describes the spatial distribution of the emitted light approximated by a three dimensional Gaussian, which is decayed to $1/e^2$ at r_0 in lateral direction and for $z = z_0$ in axial direction. The remaining parameters κ, σ and q can be combined with the excitation intensity amplitude I_0

to give a parameter to determine the photon count rate per molecule per second $\eta_0 = I_0.\kappa.\sigma.q$.

η_0 can be a measure for the signal-to-noise ratio of the measurement and give a quick comparison regarding the quality of different optical setups. Now the equation 3.3 can be modified as

$$\delta F(t) = \int_V W(\bar{r})\delta(\eta C(\bar{r}, t)).dV \tag{3.5}$$

The normalized autocorrelation function is defined as:

$$G(\tau) = \frac{\langle \delta F(t).\delta F(t+\tau)\rangle}{\langle F(t)\rangle^2} \tag{3.6}$$

where τ is the lag time to check the self similarity of the signal. Substituting equation 3.5 into equation 3.6 we get:

$$G(\tau) = \frac{\int\int W(\bar{r})W(\bar{r}')\langle\delta(\eta C(\bar{r}, t))\delta(\eta C(\bar{r}', t+\tau))\rangle dVdV'}{(\int W(\bar{r})\langle\delta(\eta C(\bar{r}, t))\rangle dV)^2} \tag{3.7}$$

we can now separate the fluctuation term as $\delta(\eta C(\bar{r}, t)) = C\delta\eta + \eta\delta C$. To simplify equation 3.7 we assume that the fluorophore's fluorescence properties are not changing with the observation time i.e. $\delta\eta = 0$, we get

$$G(\tau) = \frac{\int\int W(\bar{r})W(\bar{r}')\langle\delta C(\bar{r}, 0))\delta C(\bar{r}', \tau)\rangle dVdV'}{\left(\langle C\rangle\int W(\bar{r})dV\right)^2} \tag{3.8}$$

The term $\langle\delta C(\bar{r}, 0))\delta C(\bar{r}', \tau)\rangle$ is called the number density autocorrelation term [126]. If we consider only particles that are freely diffusing in three dimensions with the diffusion coefficient D, it can be calculated as

$$\langle\delta C(\bar{r}, 0))\delta C(\bar{r}', \tau)\rangle = \langle C\rangle\frac{1}{(4\pi D\tau)^{-\frac{3}{2}}}.e^{-\frac{(\bar{r}-\bar{r}')^2}{4D\tau}}$$

and

$$\begin{aligned} G(\tau) &= \frac{\int\int W(\bar{r})W(\bar{r}')\langle C\rangle \frac{1}{(4\pi D\tau)^{-\frac{3}{2}}}.e^{-\frac{(\bar{r}-\bar{r}')^2}{4D\tau}}\,dV\,dV'}{\left(\langle C\rangle \int W(\bar{r})dV\right)^2} \\ &= \frac{1}{(C)\,(4\pi D\tau)^{-\frac{3}{2}}}\frac{\int\int W(\bar{r})W(\bar{r}').e^{-\frac{(\bar{r}-\bar{r}')^2}{4D\tau}}\,dV\,dV'}{\left(\int W(\bar{r})dV\right)^2} \end{aligned} \tag{3.9}$$

Considering the relationship between the lateral diffusion time τ_D, which a molecule spends in the focal volume and the diffusion coefficient D

$$\tau_D = \frac{r_0^2}{4.D} \tag{3.10}$$

and, the definition of effective focal volume V_{eff},

$$V_{eff} = \frac{(\int W(\bar{r})dV)^2}{\int W^2(r)dV} = \pi^{\frac{3}{2}}.r_0^2.z_0 \tag{3.11}$$

one can calculate the autocorrelation function for one freely diffusing species of molecules:

$$G(\tau) = \frac{1}{V_{eff}\,\langle C\rangle}.\frac{1}{\left(1+\frac{\tau}{\tau_D}\right)}.\frac{1}{\sqrt{1+(\frac{r_0}{z_z})^2.\frac{\tau}{\tau_D}}} = \frac{1}{N}.\frac{1}{\left(1+\frac{\tau}{\tau_D}\right)}.\frac{1}{\sqrt{1+s^2.\frac{\tau}{\tau_D}}} \tag{3.12}$$

where $N = V_{eff}\,\langle C\rangle$ is the number of molecules inside the effective focal volume and $s = \frac{r_0}{z_z}$ is the ratio of transversal to axial dimensions of the analysis volume.

Now as we record the fluorescence signal as the fluctuation in intensity F(t) in time domain, we introduce one more correlation factor $G^2(\tau)$, taking this into consideration and using equations 3.2, 3.6 and 3.12:

$$G^2(\tau) = \frac{\langle F(t).F(t+\tau)\rangle}{\langle F(t)\rangle^2} = 1 + \frac{\langle \delta F(t).\delta F(t+\tau)\rangle}{\langle F(t)\rangle^2} = 1 + \frac{1}{N}.\frac{1}{\left(1+\frac{\tau}{\tau_D}\right)}.\frac{1}{\sqrt{1+s^2.\frac{\tau}{\tau_D}}} \tag{3.13}$$

For performing experiments at high concentration we need to take care of background signals as well, the autocorrelation function including the background noise and triplet state (dark state) effect can be given as [3, 39, 127]:

$$G^2(\tau) = 1 + \frac{1}{N}.\left(1-\frac{\langle B\rangle}{\langle F\rangle}\right)^2\left[1+n_T\exp\left(-\frac{\tau}{\tau_{b_T}}\right)\right]\frac{1}{\left(1+\frac{\tau}{\tau_D}\right)}.\frac{1}{\sqrt{1+s^2.\frac{\tau}{\tau_D}}} \tag{3.14}$$

where $\langle B \rangle$ is the background noise, n_T is the amplitude of the triplet state population, τ_{b_T} is the triplet state blinking time.

3.2 Time Correlated Single Photon counting (TCSPC)

The lifetime of standard fluorophores are generally between several hundred picoseconds and few nanoseconds. Thus, the techniques for measuring fluorescence lifetime really developed with the advent of high-speed and sensitive detectors and high repetition rate mode-locked picosecond (ps) or femtosecond (fs) laser light sources [128]. In general Time-correlated fluorescence spectroscopy is a very powerful analysis tool and to use it fully one must record the time dependent intensity profile of the emitted light. For fluorescence lifetimes as short as e.g. 500 ps, the recorded signal must be resolved to the extent that the exponential decay can be represented by some tens of samples i.e. the sampling time has to be $\sim 10\times$ lower than the typical decay time to be measured. Hence the transient recorder required would have to sample at e.g. 50 ps time steps. This is very hard to achieve with regular electronic transient recorders. Time correlated single photon counting (TCSPC) makes it possible to extend the data collection over multiple cycles, using periodic excitation (e.g. from a femtosecond laser). From these collected data over many cycles, the single cycle decay profile can be reconstructed [129].

The TCSPC is based on the the time correlated registration of fluorescence signal single photons. The excitation pulse provides the reference for the timing. Assuming that the condition of single photon probability is met a collective set of registered photons over multiple cycles would represent the time decay similar to that one would have obtained from a single shot time-resolved analog recording. The figure 3.2 illustrates how the histogram is formed over multiple cycles [129].

3.2.1 Experimental Realization

The experimental setup is based on the principle of an inverted microscope (Zeiss Axiovert 35 M) as shown in Fig 3.3. In the FCS measurements, the excitation is performed with a HeNe laser in a continuous wavelength of 633 nm. For measures of lifetime using TCSPC a second excitation channel with a picosecond laser diode operating at 636 nm (PicoQuant LDH-P-635, 80 MHz repetition rate) is used. The power of the excitation beam is controlled by a half-wave plate ($\lambda/2$) adjoining to a polarizer beam splitter. A single mode optical fiber (Thorlabs P3-630A-FC-5) ensures a perfect spatial overlap between the continuous HeNe laser and diode laser picosecond. Both excitation beams therefore follow the same optical path output, which guarantees the same focal point of excitation for the FCS experiments and fluorescence life-time measurement.

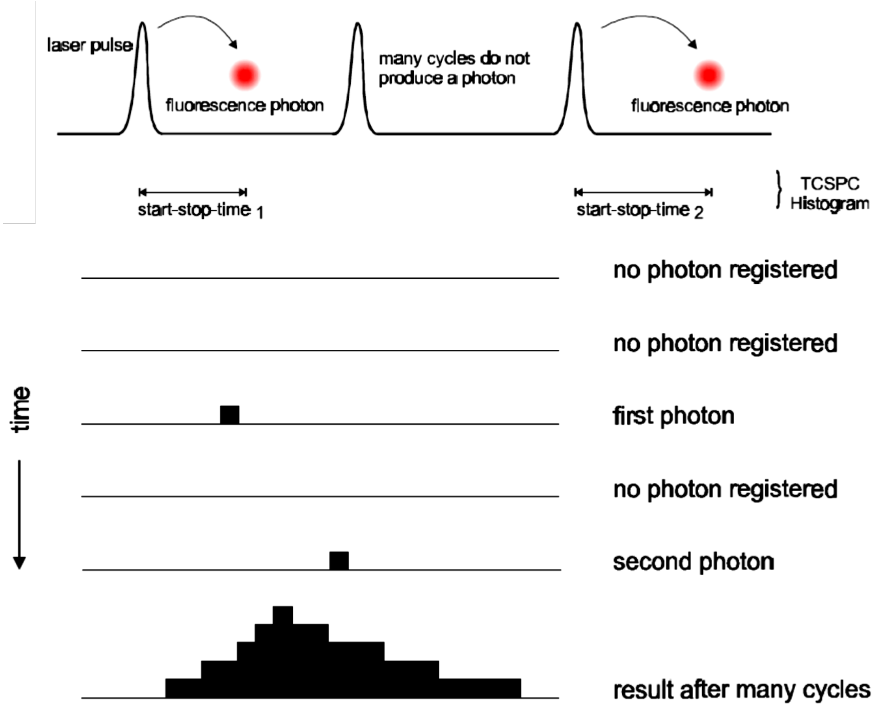

Figure 3.2: Histogram formation in TCSPC [129]

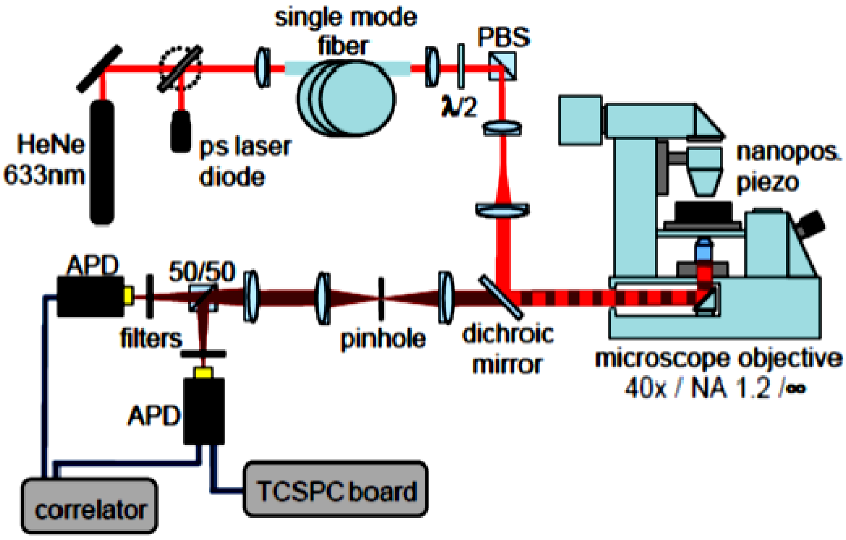

Figure 3.3: Schematic of the Experimental setup used for FCS and TCSPC

A dichroic mirror (Omega Filters XF2072) designed to work at an incidence of 45 degrees and reflects the pump beam and transmits only the fluorescence signal ($\lambda \approx 670\ nm$). After reflection from the dichroic mirror, the incident beam is focused on the sample with a high numerical aperture microscope objective(Zeiss C-Apochromat, magnification x 40, NA 1.2) which also collects the fluorescence signal from the sample. For FCS measurements at 633 nm, we mainly have used the fluophore Alexa Fluor 647 (A647, Invitrogen, Carlsbad CA, Quantum efficiency = 30% in aqueous solution), the absorption / emission peaks are respectively located around 650 and 668 nm. The photo-stability and good performance of the Alexa Fluor 647 make it a good fluorescent marker, widely used in biology. After excitation, the fluorescence signal of Alexa 647 molecules traverse through the microscope tube lens (focal length f = 160 mm) and is then filtered by a confocal pinhole placed in the image plane of the microscope objective. After confocal pinhole, the fluorescence signal is split 50/50 using a beam-splitter and focused on two avalanche photodiodes (Micro Photon Devices by PicoQuant MPD-5CTC, with a dead time of 50 ns and active surface of 50 μm) placed behind the fluorescence filters 670 ± 20 nm. The fluorescence signal fluctuation is then analysed by correlating the signals using a correlator ALV 6000. The analysis of data is done for determining the number of molecules, the translational diffusion time, the amplitude and the lifetime of the triplet state and the counting rate per molecule (CRM). For the measurements of lifetimes of fluorescence, the photodiode is coupled to a single photon counting module correlated in time (PicoQuant PicoHarp 300). The time resolution of our experimental setup for measurements of long fluorescence lifetime is 120 ps. A photograph of the experimental setup is available in Figure 3.4. Finally, to point out, a DPSS laser at a wavelength of 488 nm is also available on our mounting.

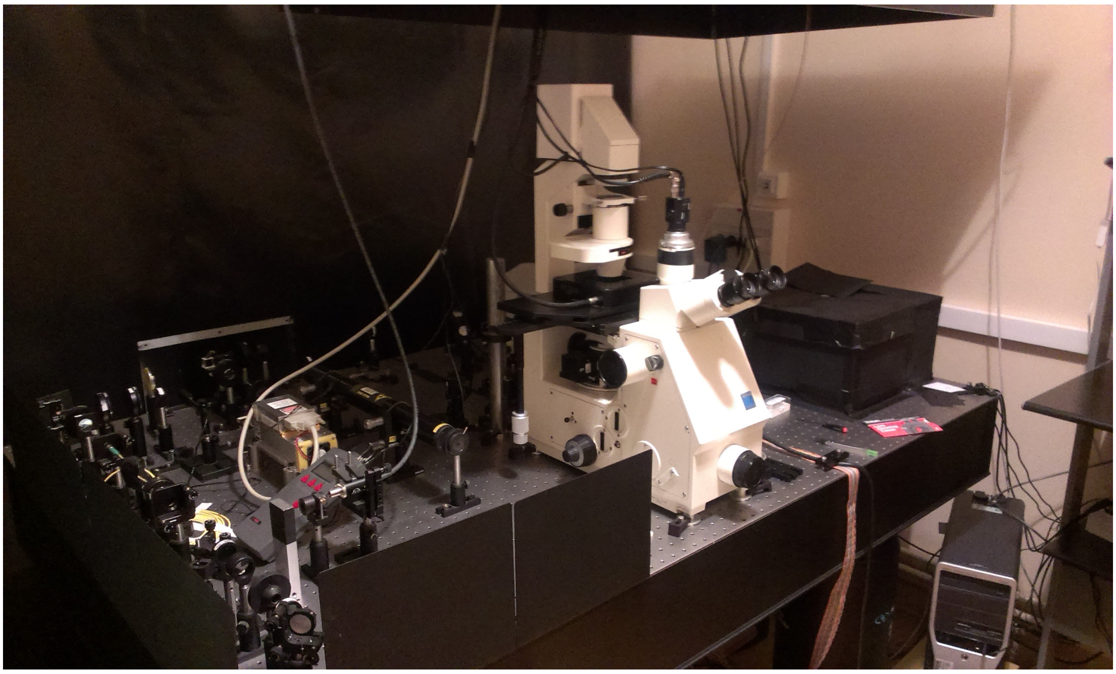

Figure 3.4: Photograph of Experimental setup used for FCS and TCSPC.

3.3 Fluorescence characterization procedure in the vicinity of nanoantenna

To introduce our characterization procedure in a few words, we implement FCS to reliably quantify the detected number of molecules and the fluorescence count rate per molecule CRM, which is recorded as the excitation power I_{exc} is raised. Global analysis of the CRM vs. I_{exc} curve, combined to lifetime measurements using time correlated single photon counting (TCSPC) alongside the FCS setup, gives the relative contribution of emission and excitation gains in the overall fluorescence enhancement [124].

The fluorescence enhancement η_F in the vicinity of nanoantenna is introduced as the ratio of the detected fluorescence rate per molecule due to the nanoantenna CRM_{ant} and in open solution CRM_{sol} at a fixed excitation power, that is $n_F = CRM_{ant}/CRM_{sol}$. To understand the physical origin of the increase in the fluorescence brightness we begin by expressing the fluorescence rate per molecule CRM. We treat the fluorophore as 3 level system. Under steady state condition CRM is given by [3]

$$CRM = \kappa\phi \frac{\sigma I_{exc}}{1 + I_{exc}/I_{sat}} \tag{3.15}$$

where κ is the light collection efficiency, $\phi = k_{rad}/k_{tot}$ the quantum yield and $I_{sat} = \frac{k_{tot}}{\sigma}\frac{1}{1+k_{isc}/k_d}$ is the saturation intensity. The photokinetic rates are noted as follows: σI_{exc} stands for the excitation rate, where σ denotes the excitation cross-section.k_{rad} and k_{nrad} are the rate constants for radiative emission and non-radiative deexcitation from excited singlet state to ground state. k_{isc} and k_d are the rate constants for inter-system crossing to the dark state and relaxation to the ground state respectively. The total deexcitation rate from the excited singlet state is noted as $k_{tot} = 1/\tau_{tot}$ is the excited state lifetime.

In the low excitation regime $I_e \ll I_s$, we get

$$CRM = \kappa\phi\sigma I_{exc} \qquad (I_{exc} \ll I_{sat}) \tag{3.16}$$

which indicates that the fluorescence rate per molecule is proportional to the collection efficiency, the quantum yield and the excitation intensity. Eq. 3.16 is the one commonly used in fluorescence spectroscopy and microscopy applied to life sciences [128, 130]. When we go into the saturation regime $(I_{exc} \gg I_{sat})$ eq. 3.15 gives

$$CRM = \kappa\phi\sigma I_{sat} = \kappa k_{rad} \qquad (I_{exc} \gg I_{sat}) \tag{3.17}$$

which indicates that the fluorescence rate per molecule at saturation is determined only by the radiative rate and the collection efficiency and is independent on the excitation rate.

We see that in the weak excitation regime, the CRM is linearly proportional with I_{exc} and by assuming that the nanoantenna does not modify significantly the fluorophore's absorption cross section (σ) , the fluorescence enhancement factor can be given as

$$\eta_F = \frac{CRM^*}{CRM} = \frac{\kappa^*}{\kappa}\frac{\phi^*}{\phi}\frac{I_e^*}{I_e} \qquad (I_{exc} \ll I_{sat}) \tag{3.18}$$

The superscript * denotes the presence of the nanoantenna.

3.4 Low quantum yield effect

In this section we are going to point out the influence of the emitter's quantum yield ($\phi = k_{rad}/(k_{rad}+k_{nrad})$) effect on the fluorescence enhancement factor. Which will lead us to the understanding of taking the advantage of low quantum yield effect to get higher fluorescence emission enhancement. We will take a closer look on how to choose ϕ for the reference solution (without the antenna) so as to maximize the fluorescence enhancement. To proceed further we assume hereafter the weak excitation regime ($I_{exc} \ll I_{sat}$), since in the saturation regime, the fluorescence enhancement does not depend directly on ϕ.

Nanoantenna modifies the quantum yield to $\phi^* = k^*_{rad}/(k^*_{rad}+k^*_{nrad}+k^*_{abs})$, a new nonradiative decay route k^*_{abs} is introduced to take into account the ohmic losses into the metal and nonradiative energy transfers to the free electrons in the metal [130]. It is also assumed that the nonradiative rate k_{nrad} is not affected by the antenna in a significant manner.

From equation 3.18 we can reach to

$$\eta_F = \frac{\kappa^*}{\kappa}\frac{k^*_{rad}}{k_{rad}}\frac{I_e^*}{I_e}\frac{1}{(1-\phi)+\phi\zeta} \tag{3.19}$$

where $\zeta = (k^*_{rad}+k^*_{abs})/k_r$ By considering a poor emitter $\phi \ll 1$ and $\phi\zeta \ll 1$ we get

$$\eta_F = \frac{\kappa^*}{\kappa}\frac{k^*_{rad}}{k_{rad}}\frac{I_e^*}{I_e} \qquad (\phi \ll 1) \tag{3.20}$$

and in the case of a perfect emitter $\phi \simeq 1$, eq. 3.19 give us

$$\eta_F = \frac{\kappa^*}{\kappa} \frac{I_e^*}{I_e} \qquad (\phi \simeq 1) \tag{3.21}$$

here we assume that the antenna has large efficiency i.e. $k^*_{rad} \gg k^*_{abs}$. We see that for a perfect emitter, the enhancement in fluorescence at weak excitation intensity is accounted by the product of the gain in collection efficiency and excitation intensity. On the other hand, in the case of poor emitter it is larger by a factor k^*_{rad}/k_{rad}. This indicates that, to maximize η_F, one should preferentially select emitters with rather low quantum yields [130].

We have mostly used Alexa 647 fluorophore in the experiments done in this thesis. It has 30% of quantum yield, in order to further decrease the quantum yield to fully exploit the low quantum yield enhancement effect we have used methyl viologen as a chemical quencher.

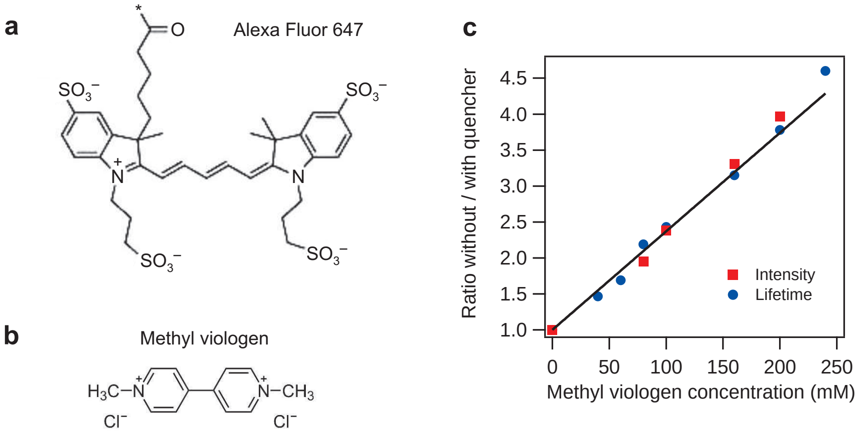

Figure 3.5: Stern-Volmer plot of the fluorescence intensity and fluorescence lifetime ratios versus the methyl viologen concentration.

Fig 3.5(a),(b) presents the chemical structure of the Alexa dye and the chemical quencher, methyl viologen. The quenching mechanism of Alexa Fluor 647 upon addition of methyl viologen is expected to be charge transfer [131]. To investigate the quenching effect, we recorded the evolution of total fluorescence intensity I_f and the fluorescence lifetime τ while the methyl viologen concentration $[MV^{2+}]$ is increased, and compare the results to the reference intensity I_{f0} and lifetime τ_0 when no quencher is present. For a standard dynamic quenching of A647 fluorescence, the intensity and lifetime ratios are expected to follow the Stern-Volmer relationship [131]:

$$\frac{I_{f0}}{I_f} = \frac{\tau_0}{\tau} = 1 + k_q \tau_0 [\mathrm{MV}^{2+}] \tag{3.22}$$

where k_q is the quenching rate. Figure 3.5 presents our experimental results, which follow nicely the Stern-Volmer linear trend. This confirms the dynamic quenching of A647 by the methyl viologen with a rate of $k_q = 1.4 \times 10^{10}\ \mathrm{s}^{-1}.\mathrm{M}^{-1}$ in the case of our experiments. It also indicates that aggregate formation between A647 and methyl viologen remains negligible at these concentrations. Fig. 3.6 shows the trend of CRM versus power variation measurement for different concentration of methyl viologen. We have found that using 200 mM concentration of MV saturates the CRM at around $13\mu W$ power. We have used 200 mM of MV at $10\mu W$ power in order to keep the low saturation regime criteria valid in our experiments.

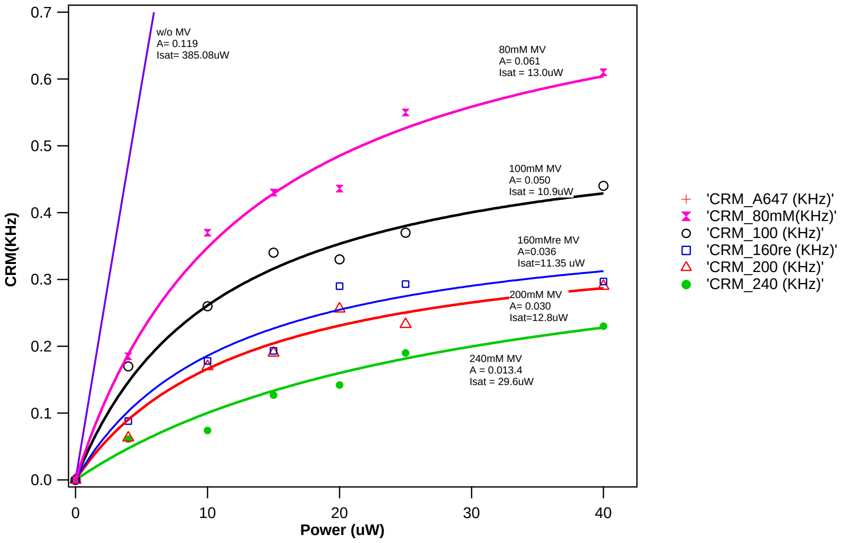

Figure 3.6: Fluorescence brightness per molecule (CRM) versus the power variation at different concentration of methyl viologen.

4 NanoAntenna-in-box design to enhance single molecule fluorescence detection

In this chapter we introduce a novel “antenna-in-box” platform, based on a gap-antenna inside a nanoaperture, which combines both enhancement and background screening, offering unprecedented single molecule sensitivity at ultrahigh sample concentrations. The rationale behind this design is that in any nanoantenna experiment on molecules in solution, the observed fluorescence is a sum of two contributions: the enhanced fluorescence from the few molecules in the nanoantnenna gap region (hot spot) and a flourescence background from several thousands of molecules within the diffraction-limited confocal volume (in our case at the concentration of $15\mu M$ of Alexa 647 fluor, we had 1 molecule in the hotspot and 4600 molecules in the confocal volume). The different components of our antenna-in-box therefore have complementary roles. A central gap-antenna creates the hot spot for enhancement and a surrounding nanoaperture screens the background by preventing direct excitation of molecules diffusing away from the central gap region. Our findings combining huge fluorescence enhancement and ultra-small detection volume renders our “antenna-in-box” device ideal for the design of massively parallel sensing platforms for single molecule analysis at micromolar concentrations. This work has been done in collaboration with Prof. Niek Van Hulst of Molecular Nanophotonics group, ICFO, Spain and Prof. María García-Parajo and Mattheiw Mivelle of Single Molecule Biophotonics group, ICFO, Spain.

4.1 Fabrication of Nanoantenna-in-box

Arrays of Nanoantenna with a pitch of 5 μm (Fig. 4.1a) were milled by Focused Ion Beam (FIB) (Zeiss Auriga 60 FIB-SEM, 1-nm-resolution GEMINI scanning electron microscope (SEM), equipped with Orsay Optics 2.5-nm-resolution Cobra ion column) on 50-nm-thick gold films deposited by thermal evaporation (Oerlikon Leybold Univex 350). It was done in ICFO, Spain by Matthew Mivelle. Adhesion between the gold film and the glass coverslip substrate was ensured by a 3-nm-thick titanium layer deposited by electron-beam evaporation. Figure 4.1 presents the scanning electron microscopy images of the fabricated nanoantennas with smallest gap sizes. The half-sphere diameter is 76 nm with gap sizes varying from 12 to 40 nm. The nanoaperture dimensions are 290 × 100 nm^2. Characteristic dimensions are directly given on the SEM images, confirming sizes of about 12 nm for the smallest gaps.

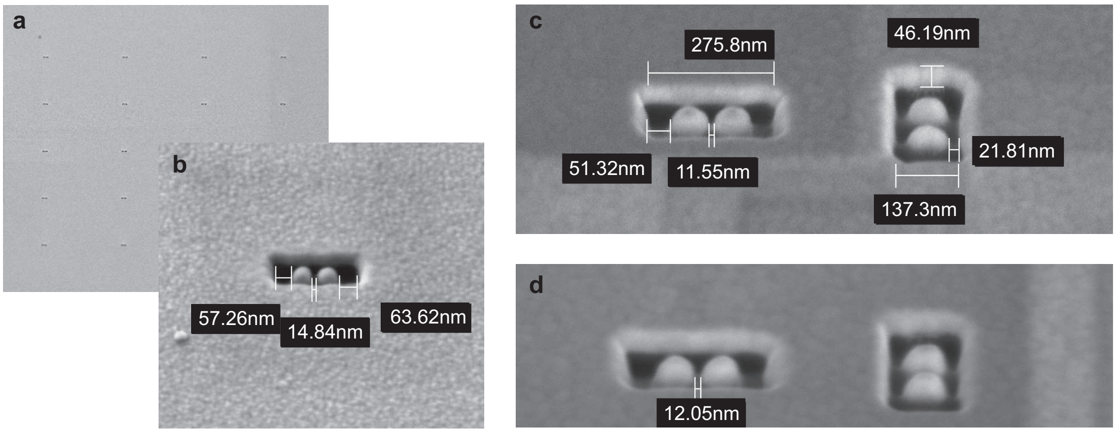

Figure 4.1: (a) Scanning electron microscopy image of an array of nanoantennas with 5 μm pitch. (b-d) Close-up view of some fabricated nanoantennas.

4.2 Numerical Simulations

Three-dimensional numerical modelling on nanoantenna-in-box was based on the finite-difference time-domain(FDTD) method using Rsoft Fullwave version 6.0. The model considers a computational space of $0.36 \times 0.2 \times 0.1 \mu m^3$ with 0.75 nm mesh size and perfect matched-layer boundary conditions on all faces. The gold antenna (refractive index = 0.183 + 2.974i) was located on a glass substrate (refractive index = 1.52) and the upper medium was water. The particle constituting the antenna was treated as a half-sphere of diameter 76 nm, the gap size was 15 nm, the aperture dimensions were $290 \times 100\ nm^2$, and the gold film thickness was 50 nm. Excitation at 633 nm was launched from the glass side. Electromagnetic intensity was measured and averaged in the gap region over the plane located 10 nm inside the antenna from the glass interface.

Figure 4.2 a and b investigate the influence of the box aperture surrounding the dimer antenna. The dimensions of the rectangular box aperture have been optimized numerically so as to screen the fluorescence contribution from the molecules diffusing away from the antenna hot spot without reducing too much the local intensity enhancement inside the hot spot. A compromise was found for a size of $290 \times 100 nm^2$. In that case, the presence of the box aperture dampens the intensity enhancement in the gap region by a factor of two from 160 to 80. Figure 4.2 c and d consider the influence of the excitation wavelength. The dielectric properties of gold are modeled according to the values in [132]. Data in fig. 4.2d provides the successive computations with fixed excitation wavelength. In this case the local excitation intensity enhancement, averaged over the gap region, is computed which reveals a plasmon resonance centered at 740 nm.

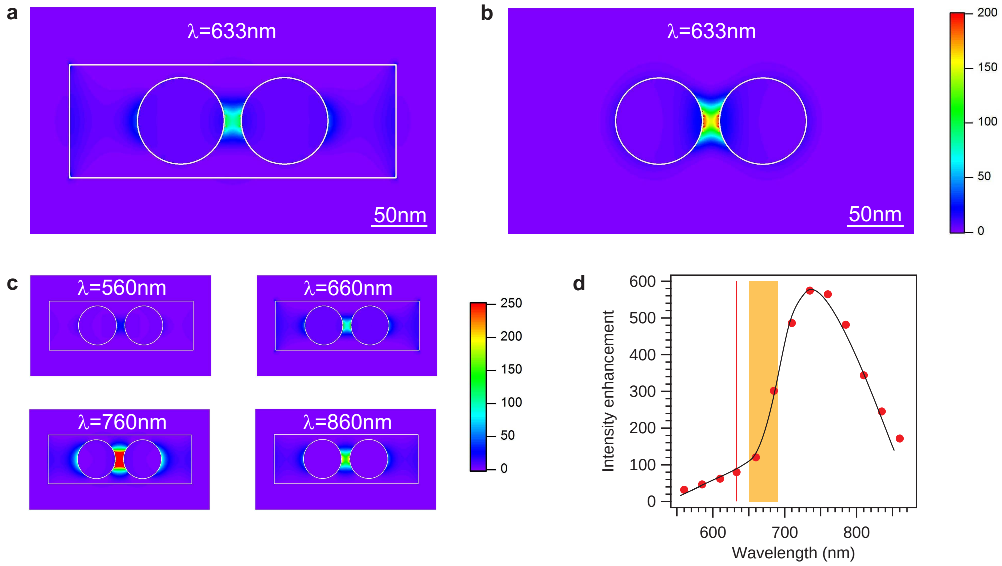

Figure 4.2: Finite-difference time-domain computation of excitation intensity enhancement for the 15 nm gap antenna in a plane 10 nm inside the antenna from the glass interface for the gap antenna inside the aperture box (a) and the gap antenna alone on glass substrate (b). The incoming light is horizontally polarized at a wavelength of 633 nm. (c) Evolution of the electric field intensity distribution with the wavelength. (d) Intensity enhancement averaged in the gap region over the plane 10 nm inside the antenna from the glass interface as a function of the excitation wavelength for the antenna surrounded by the aperture box. The red bar indicates the laser wavelength used experimentally, and the area shaded in orange shows the spectral range used for fluorescence integration. The black line is a guide to the eyes.

4.3 Experimental Setup and Methodology

The experimental set-up is based on a confocal inverted microscope with a Zeiss C-Apochromat 40x 1.2NA water-immersion objective. For FCS measurements, the excitation source is a CW He-Ne laser operating at 633 nm. Accurate positioning of the nanoantenna at the laser focus spot is obtained with a multi-axis piezoelectric stage (Polytech PI P-517.3CD). A dichroic mirror (Omega Filters 650DRLP) and a long pass filter (Omega Filters 640AELP) separate the fluorescence light from the epi-reflected laser and elastically scattered light. A 30 μm confocal pinhole defines a detection volume calibrated to 0.5 fL. After the confocal pinhole, the detection is performed by two avalanche photodiodes (Micro Photon Devices by PicoQuant MPD-5CTC) with 670 ± 20 nm fluorescence bandpass filters. The fluorescence intensity temporal fluctuations are analyzed with a hardware correlator (Flex02-12D/C correlator.com, bridgewater NJ with 12.5 ns minimum channel width). Each individual FCS measurement is obtained by averaging 10 runs of 5 s duration for the nanoantennas and 50 runs of 5 s for the confocal reference.

Chemicals

We performed experiments on Alexa647 fluorescence molecules (Invitrogen) at micromolar concentrations in a water-based phosphate buffered saline (PBS) solution, with 200 mM of Methyl Viologen (1,1'-dimethyl-4,4'-bipyridinium dichloride, Sigma-Aldrich). This concentration of methyl viologen quenches the Alexa647 quantum yield from 30% to 8%. Double stranded DNA constructs (51 base pairs) labelled with Atto647N at varying distances from the restriction site (CTGCAG) were purchased from IBA. Following PstI enzyme (Invitrogen) digestion, sequences 1 and 2 yielded 11-base-pair and 40-base-pair dsDNA-labelled constructs, respectively. The PstI cleavage reaction on 1 μg dsDNA was carried out at 37°C in bufferH(Invitrogen) for 1 h, followed by inactivation of the enzymes at 65°C for 20 min. Sequence 1: 5' CGCACTGAACAGCATATGACACGCGATAGGCTATCCTGCA ↓ GTACGCTCAGG 3'. Sequence2: 5' CGCACTGAACAGCATATGACACGCGATAGGCTATCCTGCA ↓ GTACGCTCAGG 3'. The protein A labelled with A647 was used as purchased from Invitrogen, and diluted in PBS buffer. A polysorbate surfactant (Tween 20, Sigma-Aldrich) was used at 1% concentration to avoid protein adsorption to the metal surfaces.

FCS analysis procedure

The analysis of the FCS data considers two species with different fluorescence brightness: N^* molecules in the dimer hot spot volume with brigthness Q^*, and N_0 background molecules with brightness Q_0 diffusing away from the hot spot. The fluorescence intensity correlation function can be written (see pages 75-81 of [3]):

$$G(\tau) = \frac{\langle F(t).F(t+\tau)\rangle}{\langle F(t)^2\rangle} = 1 + \frac{N^* Q^{*2} G_d^*(\tau) + N_0 Q_0^2 G_{d0}(\tau)}{N^* Q^* + N_0 Q_0} \tag{4.1}$$

where $G_d^*(\tau)$ and $G_{d0}(\tau)$ are the normalized functional forms of the correlation function for each species taken individually based on a three dimensional Brownian diffusion model:

$$G_{di}(\tau) = \frac{1 + n_{T,i} \exp\left(-\frac{\tau}{\tau_{b_T,i}}\right)}{(1+\tau/\tau_{d,i})\sqrt{1+s_i^2\tau/\tau_{d,i}}} \tag{4.2}$$

$n_{T,i}$ stands for the amplitude of the dark state population, and $\tau_{b_T,i}$ the dark state blinking time, $\tau_{d,i}$ the mean residence time (set by translational diffusion) and s_i the ratio of transversal to axial dimensions of the analysis volume. Equation 4.1 indicates that the different fluorescent species contribute to the amplitude of $G(\tau)$ in proportion to the square of their relative fluorescence brightness. As a consequence of the stochastic nature of FCS, the presented fluorescence data are spatially averaged over all the possible molecule orientations and positions inside the nanoantenna hot spot.

For the FCS analysis in the case of the nanoantenna, the parameters N_0, Q_0 for the molecules diffusing away from the hot spot are fixed according to the values found for a rectangular aperture without a dimer nanoantenna inside. N_0 is deduced from the number of molecules observed with the rectangular aperture corrected by a factor of 0.7× to account for the volume taken by the nanoparticle dimer. Q_0 is the fluorescence brightness found for the aperture, which is 4× enhanced as compared to the open solution reference. The shape parameter is also fixed to s = 0.2 to allow for direct comparison between diffusion times. This parameter was found to have a negligible influence on the estimates for N^* and Q^* which are the main goal of the experiment. Lastly, at $10\mu W$ excitation power the background noise originating from the back-reflected laser light and from gold autofluorescence is below 1 kHz, which is negligible as compared to the count rates per molecule in the nanoantennas.

4.4 Experimental Results

Enhanced Single Molecule Analysis with Nanoantenna-in-box

For direct observation of single molecule diffusion events, the nanoantennas are covered by a solution containing the fluorescent dyes and the chemical quencher. The molecules constantly diffuse in a Brownian fashion around the nanoantenna, thus the configuration is virtually not limited by photobleaching. The fluorescence signal F is analysed by FCS (see chapter 3 for details of the methodology) to quantify the detection volume and fluorescence brightness per molecule [33, 56]. For a homogeneous sample with a single fluorescent species, the amplitude of the correlation function G scales with the inverse of the average number of molecules in the detection volume N, and provides access to the fluorescence brightness per molecule $Q = \langle F \rangle / N$. In the case of the nanoantenna, the FCS curves are analyzed with a model considering two species with different brightness using Equation 4.1: N^* molecules in the hot spot volume with brightness Q^*, and N_0 background molecules with brightness Q_0 diffusing away from the hot spot. An important feature of FCS is that the different fluorescent species contribute to the amplitude of G in proportion to the square of their fluorescence brightness [3]. Hence, a large fluorescence enhancement in the hot spot improves the signal-to-background contrast in FCS by a quadratic manner.

Confocal experiments at 15 μM concentration collect a large fluorescence signal with reduced temporal fluctuations (Fig. 4.3a,b). The FCS analysis measures an average number of $N_{sol} = 4630$ molecules, corresponding to the 15 μM concentration and the 0.5 fL detection volume calibrated independently. The brightness per molecule in the presence of the quencher is $Q_{sol} = 760/4630 = 0.17$ kHz. In contrast, the fluorescence time traces for nanoantennas (Fig. 4.3c) have lower intensity levels but larger relative fluctuations. FCS data display remarkably higher correlation amplitudes, shorter diffusion times and excellent signal-to-noise characteristics (Fig. 4.3d). Such features can only be obtained by monitoring a small number of molecules with high apparent brightness from a small detection volume. In the case of excitation polarization parallel to the dimer axis, we obtain an average number of $N^* = 0.96$

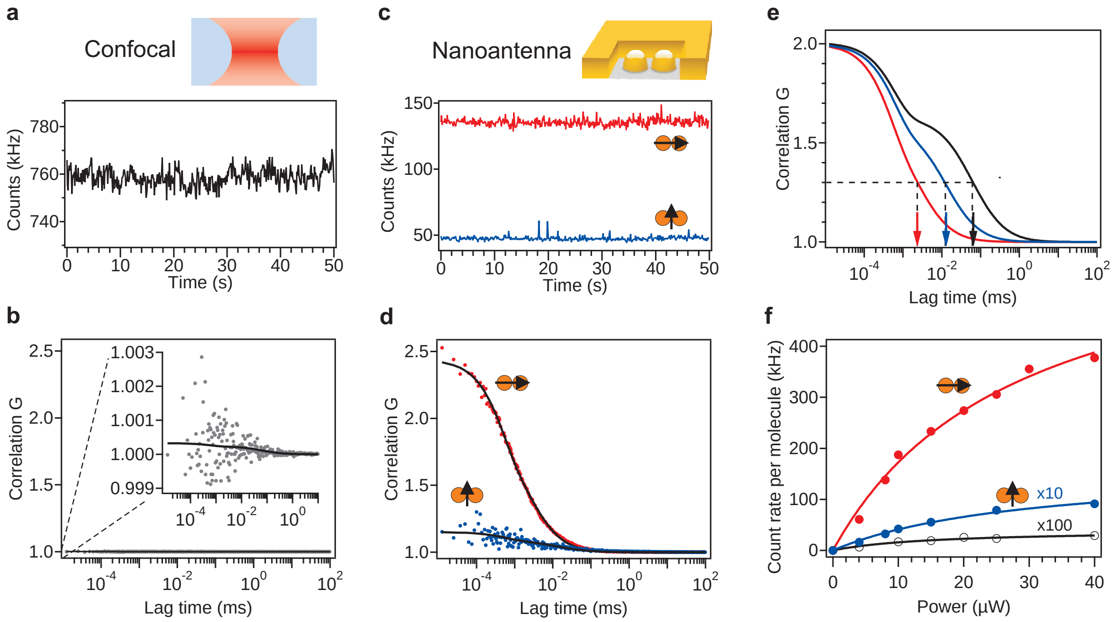

Figure 4.3: **Enhanced single molecule analysis with an "antenna-in-box"**. (a) Fluorescence time trace and (b) FCS correlation function for the reference confocal setup. Due to the large number of molecules in the confocal volume, the correlations are almost hidden with amplitudes close to one (the insert provides a close-up view). (c) and (d) display the time traces and correlation functions for a nanoantenna with 15 nm gap size, with the excitation polarization set parallel (red) or perpendicular (blue) to the nanoantenna. For all data in (a-d), Alexa Fluor 647 concentration is 15.5 μM, and 200 mM of methyl viologen is used as a chemical quencher. The excitation power is constant at 10 μW. (e) Normalized FCS curves for the nanoantenna with parallel (red) and perpendicular (blue) polarization orientation. The reference FCS curve for the diffraction-limited confocal set-up is shown in black. Arrows indicate the average residence times for molecules in the observation volumes. (f) Fluorescence count rates per molecule versus the excitation power. The data for the nanoantenna with perpendicular polarization (blue) and the reference confocal set-up (black) are multiplied respectively by 10x and 100x to allow visualization in the same plot.

molecules in the hot spot with brightness $Q^* = 128.7$kHz. These values correspond to a fluorescence enhancement of $Q^*/Q_{sol} = 758$, and a detection volume reduction of $N_{sol}/N^* = 4820$, or equivalently a hot spot volume of 104 zL (1zL = 10^{-21}L). The influence of the excitation laser polarization (Fig. 4.3c,d) confirms that the fluorescence signal stems from the nanoantenna hot spot.

Nanoantennas have excellent temporal resolutions. Normalized FCS curves for nanoantennas with parallel and perpendicular polarizations are shown in Fig. 4.3e in comparison to the confocal reference. In case of parallel excitation polarization, the average residence time for molecules in the hot spot amounts to only 2.4 μs, nearly two orders of magnitude shorter than the confocal reference. This huge reduction in time scales highlights the distinction between molecules in the hot spot and molecules away in the confocal volume. Moreover, it indicates that molecular adhesion to the nanoantenna remains minimal in our case. The “antenna-in-box” transforms a poor-quantum-yield dye into a very bright emitter: we detect count rates above 300 kHz per molecule with the nanoantenna (Fig. 4.3f), while for the confocal setup A647 fluorescence saturates to values below 1 kHz with methyl viologen, or 25 kHz without quencher [56]. Importantly, the count rates with the nanoantenna significantly exceed those obtained with a high-quantum-yield emitter in a confocal microscope.

While the experiments with antenna-in-box offers the best performance, it is complementary and informative to compare the antenna-in-box (Fig 4.3) to the two cases, one with box aperture alone (Fig 4.4) and second the gap-antenna alone (Fig 4.5). We took special care to ensure that all these cases have the identical experimental conditions. As mentioned in the case of antenna-in-box for the other two cases also we used Alexa Fluor 647 of concentration $15.5\mu M$, 200 mM of methyl viologen as chemical quencher, and $10\mu W$ as the excitation power. Table 5.1 summarizes and compares all FCS results for all these case.

Figure 4.4 presents the experimental results obtained while investigating the box aperture without the gap antenna. The excitation polarization is set along the main axis of the rectangular aperture to provide a direct comparison with the antenna-in-box with parallel excitation and ensure maximum fluorescence enhancement and volume reduction [133]. Without the plasmonic enhancement induced by the gap antenna, the fluorescence time trace and the FCS correlogram have lower levels as compared to the antenna-in-box (see Fig. 4.3c,d). For the box aperture alone, we obtain an average number of $N_{box} = 45.9$ molecules with brightness $Q_{box} = 0.75$kHz. These values correspond to a fluorescence enhancement of $Q_{box}/Q_{sol} = 4.4$, and a detection volume reduction of $N_{sol}/N_{box} = 101$, and are in good agreement with earlier work on rectangular nanoapertures [133].

The experimental results obtained with the gap antenna without the metal box are summarized in Fig. 4.5. In the case of gap antenna without the metal box there is not screening induced by the box. We see a fluorescence time trace with higher level as compared to the antenna-in-box case (see Fig. 4.3c). This effect comes from the direct excitation of a larger number of

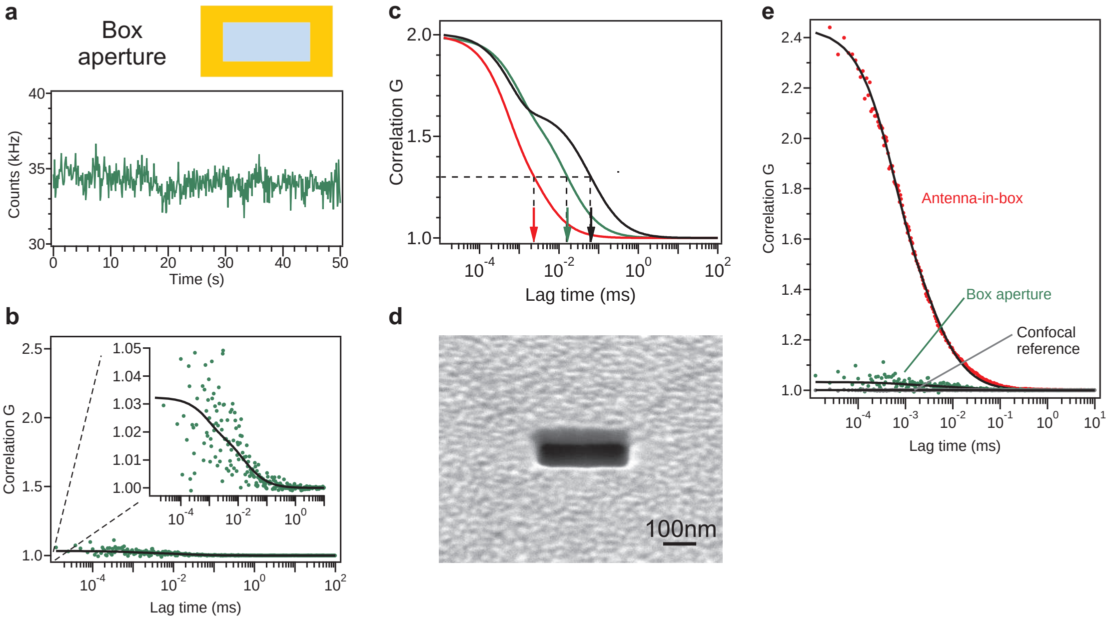

Figure 4.4: **Experiments with a box nanoaperture without gap antenna**. The experimental conditions are the same as in the case of antenna-in-box: Alexa Fluor 647 concentration is 15.5 μM, and 200 mM of methyl viologen is used as a chemical quencher. The excitation power is 10 μW, and the excitation polarization is set along the rectangle major axis. (a) Fluorescence time trace and (b) FCS correlation function of the raw data. (c) Normalized FCS curves for the antenna-in-box (red), the nanoaperture box (green) and the reference diffraction-limited spot (black). Arrows indicate the average residence times for molecules in the observation volumes. (d) SEM image of a fabricated nanoaperture. (e) Comparison between the raw correlation functions obtained with the antenna-in-box, the box aperture and the confocal reference, taken under same experimental conditions.

N_0 background molecules within the diffraction-limited confocal volume that diffuse away from the central hot spot region. The FCS correlogram amplitude in this case turns out to be 100× lower than the case of antenna-in-box (Fig. 4.5b), although the antennas have similar (~ 15 nm) gap sizes and a similar (~ 15 μM) fluorophore concentration is taken. This is a direct consequence of the increased value of the number of background molecules N_0 on the value of $G(0)$ (see Eq. 4.1), and demonstrates the crucial need of the box for background screening. The influence of the excitation laser polarization confirms that the fluorescence signal stems from the nanoantenna hot spot. In case of parallel excitation polarization, the correlation time goes down to 3.2 μs, which approaches the residence time found in the hot spot of the antenna-in-box. When the polarization is turned to perpendicular, the correlation time increases to 34 μs, and becomes closer to the confocal reference.

In the case of the gap antenna alone, special care is needed to recover the fluorescence enhancement and volume reduction from the FCS data. From the fluorescence level measured while the excitation polarization is set perpendicular to the antenna, we estimate the number

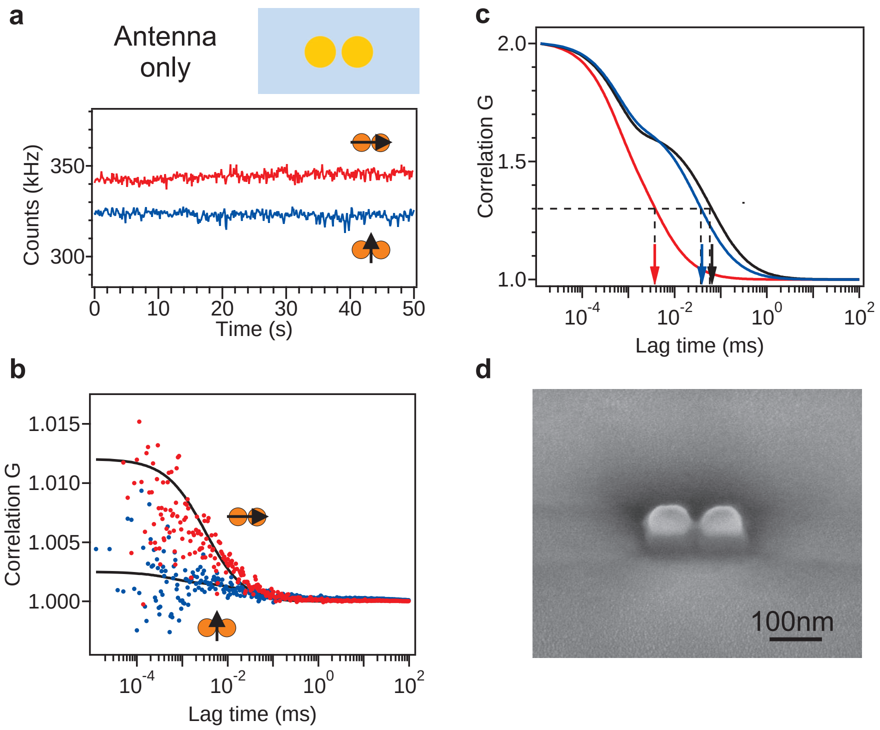

Figure 4.5: **Experiments with a nanoantenna without box (15 nm gap)**, under identical conditions as in the cases of antenna-in-box and box-only: Alexa Fluor 647 concentration 15.5 μM, with 200 mM methyl viologen and 10 μW excitation power. (a) Fluorescence time traces and (b) raw FCS correlation functions for the two excitation polarizations of the antenna. (c) Normalized FCS curves for the antenna with parallel (red) and perpendicular (blue) polarization orientation. The reference curve for the confocal set-up is shown in black. (d) SEM image of a fabricated gap antenna.

of background molecules to $N_0 \simeq 320/0.17 \simeq 1850$, and we assume that the brightness Q_0 of the background molecules is the same as the brightness $Q_{sol} = 0.17$ kHz of molecules in solution. Using these values and Eq. 1, we obtain an average number of $N^* = 0.9$ molecules in the hot spot with brightness $Q^* = 32$kHz in the case of parallel excitation polarization. These findings translate into a fluorescence enhancement of $Q^*/Q_{sol} = 190$, and a detection volume reduction of $N_{sol}/N^* = 5140$. Both experimental results stand in correct agreement with the values inferred from the experiments with the antenna-in-box. However, because of the lack of background screening induced by the box, the signal-to-background discrimination is less straightforward, and significant corrections to retrieve N^* and Q^* are required in the case of antenna-without-box.

	Solution Reference (confocal)	Box Aperture	Antenna-in-box		Antenna alone (no box)	
			Parallel Excitation	Perpendicular Excitation	Parallel Excitation	Perpendicular Excitation
Display	Fig. 4.3	Fig. 4.4	Fig. 4.3	Fig. 4.3	Fig. 4.5	Fig. 4.5
$G(0)-1$	0.00031	0.032	1.42	0.19	0.012	0.002
N	4630	45.9	0.96	6.37	0.9	1850
τ_d (μs)	61	14	2.1	12.9	3.2	34
n_T	0.43	0.49	0.67	0.69	0.54	0.51
τ_{b_T} (μs)	0.6	0.75	0.5	0.6	0.5	0.6
Q (kHz)	0.17	0.75	128.7	5.5	32	0.17
Fluorescence Enhancement		4.4	758	32.2	190	1
Volume Reduction		101	4823	727	5140	2.5

Table 4.1: **Fitting parameter results for the FCS curves**, taken under identical conditions (Alexa Fluor 647 concentration 15.5 μM, with 200 mM of methyl viologen used as a chemical quencher, the antenna gap size is 15 nm, and the excitation power is 10 μW). For the nanoantennas, the data shown here correspond to the molecules in the hot spot. For the antenna-in-box, the data for the background molecules is deduced from to the observations with the rectangular aperture without gap antenna corrected by a factor of 0.7x to account for the volume occupied by the gold hemispheres. For the antenna alone, the data for the background molecules is deduced from to the observations with the perpendicular polarization orientation (see Section 4 for discussion). Following the standard definition for the FCS correlation function, the quantity $G(0)-1$ quantifies the amplitude of the fluorescence correlations.

Gap size influence over Fluorescence Enhancement and Volume reduction

Local field enhancement critically depends on the antenna gap sizes. The gap sizes designed during the FIB fabrication ranging from 40 nm down to 15 nm by increments of 5 nm, serves as an input parameter to calculate the Fluorescence enhancement and volume reduction. Figure 4.6 shows the average enhancement factor and volume reduction found as a function of the gap size used for the FIB design. These values provide the standard specifications that can be expected for a given antenna design and the FIB used in our study. Results of the average fluorescence enhancement factor with gap sizes of 15, 20, 25, 30 and 40 nm are 610 ± 340, 130 ± 80, 36 ± 6, 17 ± 3, and 8.5 ± 3.

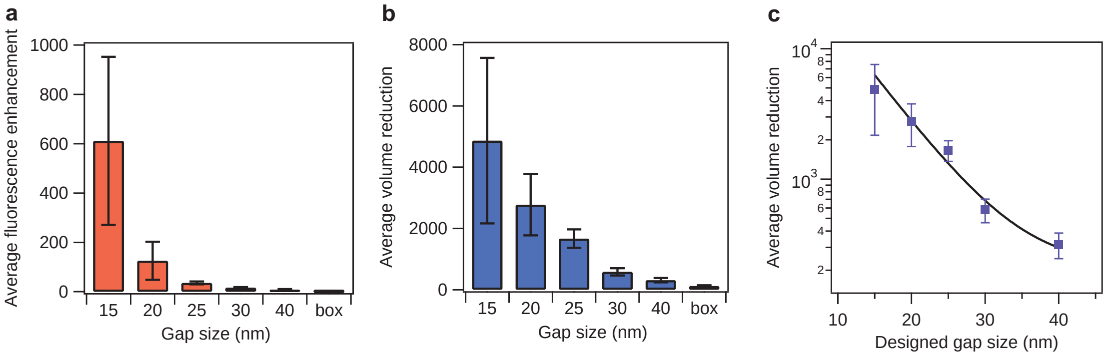

Figure 4.6: (a) Mean fluorescence enhancement factor and volume reduction (b) as a function of the gap size used for the FIB design. Error bars indicate the standard deviation for the measurements. (c) is the same as (b) in logarithmic scale for the vertical axis. The black line is a numerical fit using a single exponential function found to provide the best fitting upon χ^2 minimization.

Slight variation in gap size from antenna to antenna due to the FIB fabrication procedure (can be seen in SEM imaging, Fig. 4.1) results in the variation of the gap size actually milled from antenna to antenna, as indicated by the statistical dispersion of the FCS results (Fig 4.6). As expected, the statistical variation becomes more prominent as the gap size is reduced and the enhancement factor increase.

We use the interpolation of the average volume reduction as a function of the designed gap size parameter used for FIB to quantify the actual antenna gap size from the FCS measurements for each antenna (Fig. 4.6c). We use a single exponential function to interpolate the experimental points in Fig. 4.6c, with a weighing proportional to the data standard deviation. The single exponential model is empirically deduced from χ^2 minimization (for a single exponential model, we obtain $\chi^2 = 2.40$, while a double-exponential model yields $\chi^2 = 2.46$ and a power law model gives $\chi^2 = 3.84$). We thus obtain the relationship : $R_V = 78170 \times \exp(-0.17g) + 210$, where $R_V = N_{sol}/N^*$ is the volume reduction and g the actual antenna gap size. The constant is related to the volume reduction induced by the box aperture. Using this equation, we relate the volume reduction R_V measured for each antenna to a gap size g. We emphasize this procedure is independently confirmed by SEM imaging (Fig. 4.1c,d), and provides an alternative quantification of the gap size.

We performed experiments on 59 nanoantennas with gap sizes ranging from 12 to 40 nm. Fig 4.7a and b presents the scatter plots of the fluorescence enhancement as a function

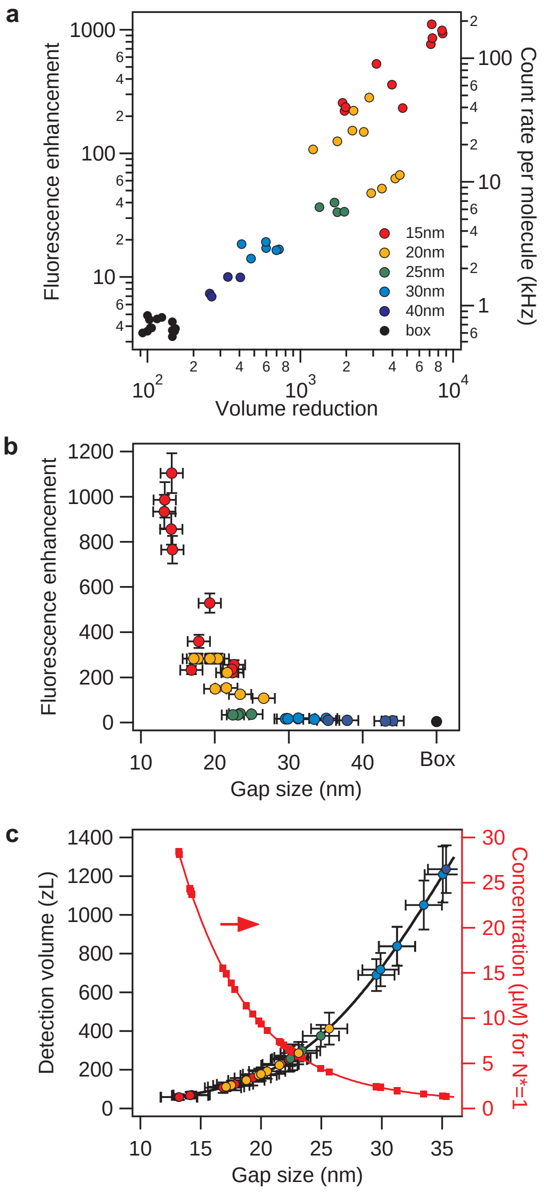

Figure 4.7: **Fluorescence enhancement and volume reduction as function of nanoantenna gap size.** (a) Scatter plot of fluorescence enhancement versus volume reduction as compared to the diffraction-limited confocal set-up. The marker colour indicates the gap size used for the FIB process. (b) Scatter plot of the fluorescence enhancement factor as a function of gap size calibrated by FCS. (c) Detection volume and concentration for which there is, on average, an individual molecule in the nanoantenna detection volume. Lines are guide to the eyes, and follow an exponential trend.

of volume reduction and gap size for all these nanoantennas. Clear correlation between fluorescence enhancement and volume reduction consistent with field localization in the gap region is observed. The nanoantennas with smallest gap sizes yield the highest fluorescence enhancement and volume reduction, up to 1100x enhancement factor and 8550x volume reduction compared to confocal excitation. The effective detection volume measured with FCS is plotted in Fig. 4.7c as a function of gap size. A record-beating confinement is obtained with a volume down to 58 zL for a gap size of 12 nm. Remarkably, this detection volume is four orders of magnitude smaller than the diffraction limit.

Fluorescence spectra analysis

To investigate the nanoantenna's influence on the fluorescence spectrum, the fluorescence beam after the confocal pinhole was sent to a spectrograph (Horiba iHR320) equipped with a Peltier-cooled CCD detector. The raw spectrum is normalized by the number of molecules given by FCS, which allows to directly compare the fluorescence spectra computed back to *per single molecule* and quantify the fluorescence enhancement as a function of emission wavelength.

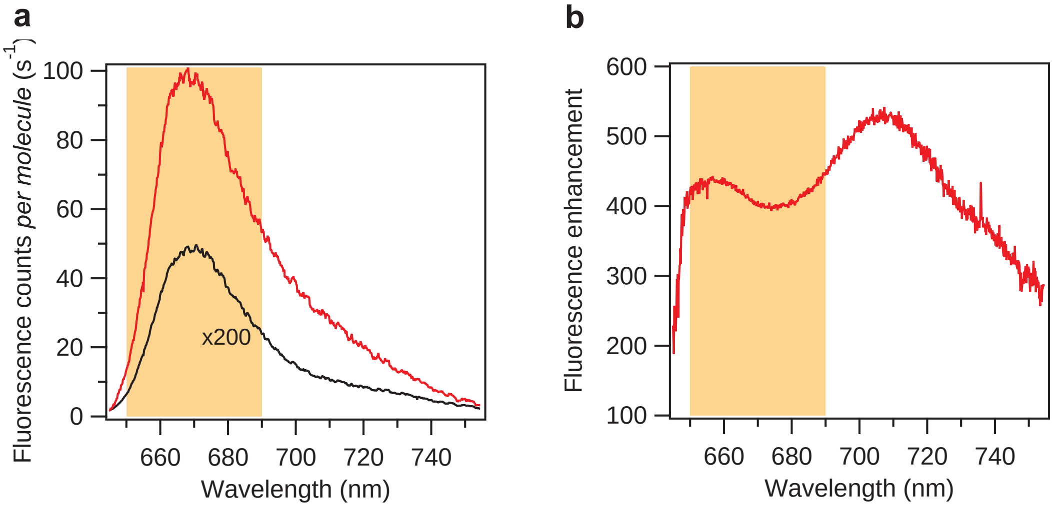

Figure 4.8: **Spectral analysis of the fluorescence enhancement.** (a) Fluorescence spectra normalized by the number of molecules detected by FCS for the nanoantenna with 15 nm gap (red) and the reference solution (black, multiplied by 200 for display). (b) Fluorescence enhancement factor vs. emission wavelength deduced from the data in (a). The areas shaded in orange indicate the spectral range used for fluorescence integration in the data presented in the main document, and corresponds to the peak emission of alexa Fluor 647.

Figure 4.8a presents fluorescence spectra per A647 molecule, showing count rates per molecule enhanced by more than two orders of magnitude over the whole emission spectrum. Careful comparison of the spectra shapes indicates a broadening of the spectrum tail above 690 nm. This feature is better visualized by computing the spectral enhancement factor which is the ratio of the fluorescence spectra per molecule found respectively with the nanoantenna and the diffraction-limited setup (Fig. 4.8b). A spectral resonance around 710 nm is apparent, which qualitatively corresponds to the resonance feature expected from the numerical simulations (Fig. 4.2). This further confirms the plasmonic origin of the fluorescence enhancement, and provides guidelines for the further optimization of the nanoantenna performance.

Fluorescence lifetime analysis and decay race discussion

Fluorescence lifetime measurements are performed by time-correlated single photon counting (TCSPC). The experimental setup for this is already discussed in Chapter 3. The excitation source is switched to a picosecond pulsed laser diode operating at 636 nm (PicoQuant LDH-P-635, repetition rate 80 MHz). A single-mode optical fiber (Thorlabs P3-630A-FC-5) ensures a perfect spatial overlap between the pulsed laser diode and the CW HeNe laser used for FCS. This guarantees the same excitation spot for FCS and TCSPC and almost same wavelength. The photodiode output is coupled to a fast time-correlated single photon counting module (PicoQuant PicoHarp 300). The overall temporal resolution of our setup for fluorescence lifetime measurements is 120 ps FWHM.

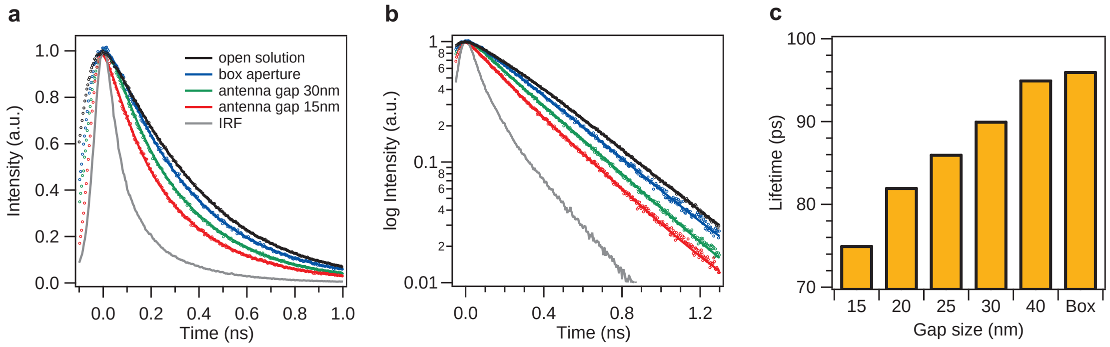

Figure 4.9: (a) Normalized fluorescence decay traces. Solid lines correspond to bi-exponential fits. The light gray decay trace shows the instrument response function (IRF). (b) is the same as (a) in logarithmic scale for the vertical axis. (c) Lifetime of the fast component of the decay trace as a function of the gap size.

As for FCS, the TCSPC data contains the respective fluorescence contributions from two sets of molecules: N^* molecules in the dimer hot spot volume with brightness Q^*, and N_0 background molecules with brightness Q_0 diffusing away from the hot spot. Therefore, we use a bi-exponential function to model the fluorescence decay traces, and take into account the convolution by the instrument response function (IRF) which bears also a double exponential decay : $IRF(t) \propto A_1 \exp(-k_1 t) + A_2 \exp(-k_2 t)$ with $A_1 = 0.516$, $A_2 = 0.484$, $k_1 = 5.7\ 10^9\ \mathrm{s}^{-1}$ and $k_2 = 20.7\ 10^9\ \mathrm{s}^{-1}$.

Figure 4.9a,b shows the normalized experimental decay traces in linear and logarithmic scales, lines are bi-exponential fits convoluted by the IRF. Two characteristic decay times are clearly visible for the antennas with smallest gap dimension: a fast decay that we assign to molecules in the vicinity hot spot, and a longer decay corresponding to the molecules diffusing away from the hot spot. A significant narrowing of the decay traces is observed with the nanoantenna as compared to the confocal reference (Fig. 4.9c): the fast decay time amounts to 75 ps for antennas with 15 nm gap, while the mono-exponential decay time of Alexa Fluor 647 in presence of 200mM of methyl viologen is 270 ps in the confocal detection case. We point out that for TCSPC each set of molecules contributes to a proportion linear to the product $N \times Q$, while for FCS the contribution is weighted by the square of the brightness $N \times Q^2$ (see Eq. 4.1). Therefore, the contrast between the fluorescence from molecules in the hot spot and the fluorescence from molecules away inside the confocal volume is lower by more than one order of magnitude for TCSPC as compared to FCS. This effect complicates the assignment of the fast decay time to the only N^* molecules in the hot spot, and partly explains why we observe only a moderate lifetime reduction of $\sim$ 4x while lifetime reductions exceeding ten-fold would be expected from the measured fluorescence enhancement factors.

We focus on the case of a nanoantenna with 15 nm gap and infer the relative enhancement factors of the quantum yield and the radiative, non-radiative and total decay rates in the case of Alexa Fluor 647 with 200 mM methyl viologen. We consider the average fluorescence enhancement factor deduced from FCS measurements $\eta_F = 610$ (Fig. 4.6a) and also assume the local excitation intensity enhancement to be given from the numerical simulations to $\eta_{exc} = 80$ (Fig. 4.2). These values indicate that the quantum yield enhancement amounts to $\eta_\phi = \eta_F / \eta_{exc} = 7.6$ (here we also consider that the nanoantenna does not provide any gain in the collection efficiency, which is fair for a structure acting as a dipole antenna; we also checked this point by back focal plane imaging). A Stern-Volmer analysis discussed in Chapter 3 indicates that the quantum yield of Alexa Fluor 647 is reduced by 4x in presence of 200 mM of methyl viologen, hence we consider that the quantum yield for the reference molecules in solution in the case of our experiments is $\phi_{sol} = 30/4 = 7.5\%$. The quantum yield enhancement factor of $\eta_\phi = 7.6$ thus means the quantum yield of the emitter inside the hot spot is boosted by the antenna up to a value of $\phi^* = \eta_\phi \phi_{sol} = 57\%$.

To estimate the relative enhancements of the radiative, non-radiative and total decay rates, we first set the normalized radiative decay rate in solution to $k_{r,sol} = 1$. The quantum yield of $\phi_{sol} = 7.5\%$ means that the (normalized) total decay rate is $k_{tot,sol} = k_{r,sol}/\phi_{sol} = 13.3$ and that the non-radiative rate (dominated by methyl viologen quenching) is $k_{nr,sol} = k_{tot,sol} - k_{r,sol} = 12.3$. Based on time-reversal argument, the radiative rate enhancement is expected to be equal to the excitation intensity enhancement *computed at the emission wavelength* $\eta_{rad} = \eta_{exc}(\lambda_{em})$, and thus the radiative rate with the antenna becomes $k_r^* = \eta_{exc}(\lambda_{em}) k_{r,sol} = 180$ (see Fig. S2). Knowing the quantum yield and the radiative rate in the antenna, we can deduce the total decay rate $k_{tot}^* = k_r^* / \phi^* = 315$. Here, we obtain that the expected lifetime reduction is $k_{tot}^* / k_{tot,sol} = 23.7$ (due to the low contrast inherent to the TCSPC method, we could measure only a lifetime reduction of 4x, but this value is limited by the difficulty to extract the fluorescence contribution from the hot spot). Finally, the non-radiative decay rate with the nanoantenna is estimated to $k_{nr}^* = k_{tot}^* - k_r^* = 135$, among which a value of

12.3 is related to methyl viologen quenching and 123 to ohmic losses to the metal. Table S3 summarizes the different estimated values. Altogether, these figures offer a physically realistic picture of the fluorescence enhancement phenomenon inside a nanogap antenna.

	k_r	k_{nr}	k_{tot}	ϕ
Solution	1	12.3	13.3	0.075
Antenna	180	123	315	0.57

Table 4.2: Estimated values for the radiative rate k_r, non-radiative rate k_{nr}, total decay rate k_{tot} and quantum yield ϕ in the case of Alexa Fluor 647 with 200 mM methyl viologen. The gap size of the nanoantenna is 15 nm. All rates are normalized so that $k_r = 1$ in the case of the solution reference.

FCS experiments without chemical quencher

In order to find out the contrast between the effect of nanoantenna-in-box design with and without quencher, we performed the similar experiment in a without-quencher environment. In the absence of chemical quencher, the quantum yield of Alexa Fluor 647 in water solution is around 30%. Thus the enhancement factor for quantum yield brought by the nanoantenna can never exceed 3.3-fold, and the overall fluorescence enhancement is expected to be lower as compared to the experiments conducted with methyl viologen. Lower fluorescence enhancement factors complicate the FCS analysis, as it becomes more difficult to extract the information from the hot spot over the very large background fluorescence from molecules diffusing away from the hot spot. However, thanks to the quadratic weighing of the FCS correlation functions with the fluorescence brightness Q^*, we found it possible to perform FCS and extract hot spot information even without chemical quencher.

	Solution Reference	Rectangular Aperture	Nanoantenna Parallel Exc.	Nanoantenna Perpendicular Exc.
N	1439	12.0	1.3	3.6
τ_d (μs)	60	11.4	1.6	7.6
n_T	0.4	0.5	0.9	0.85
τ_{b_T} (μs)	5	0.9	0.5	0.8
Q (kHz)	1.1	3.4	68.2	5.3
Fluorescence enhancement		3.1	62	4.8
Volume reduction		120	1083	403

Table 4.3: Fitting parameters of the FCS curves for Fig. 4.10 (Alexa Fluor 647 concentration is 5 μM, no methyl viologen, the antenna gap size is 15 nm, and 10 μW excitation power). The data indicated for the nanoantenna correspond to the molecules in the nanoantenna hot spot.

Figure 4.10 and Table 4.3 summarize our main results for a nanoantenna with 15 nm gap. These findings are to be compared to the use of methyl viologen (Fig. 4.3). The enhancement

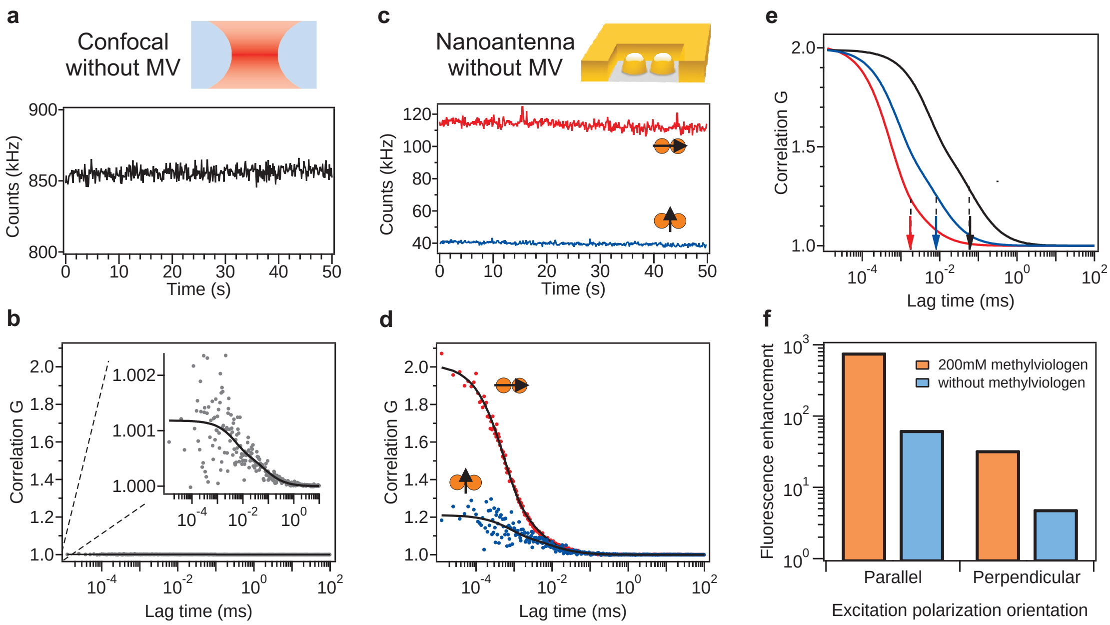

Figure 4.10: **Experiments without chemical quencher**. (a) Fluorescence time trace and (b) FCS correlation function for the reference confocal setup. (c) and (d) display the time traces and correlation functions for a nanoantenna with 15 nm gap size, with the excitation polarization set parallel or perpendicular to the nanoantenna. Alexa Fluor 647 concentration is 5 μM. The excitation power is 5 μW for (a,b) to avoid saturating the photodiodes, and 10 μW for (c,d). (e) Normalized FCS curves for the nanoantenna with parallel (red) and perpendicular (blue) polarization orientation, and the diffraction-limited spot (black). (f) Comparison of the fluorescence enhancement factor found respectively with and without the chemical quencher.

factor is 62 for the excitation polarization along the dimer axis, approximately one order of magnitude lower than with methyl viologen. Remarkably, the diffusion times τ_d appear similar in the measurements with and without methyl viologen for all configurations (confocal, box aperture, antenna). This forms a supplementary indication that there is no aggregation effect between the fluorescent dye and methyl viologen at the concentrations involved in this study. We also point out that in the absence of chemical quencher, nanoantennas with gap sizes larger than 25 nm provide FCS data comparable to the box aperture. In other words, no useful information about the hot spot can be extracted from the antenna data in the case of large gaps without chemical quencher, because the enhancement factors are too low.

The fluorescence enhancement factor is an intuitive metric that appears commonly used as a figure of merit for a practical antenna realization. However, it is not an intrinsic property of the antenna, and critically depends on several experimental parameters, such as the setup collection efficiency, emitter's quantum yield and excitation intensity [130]. For instance, ultra-high enhancement factors can be obtained while using low quantum yield emitters, as indicated in this work and previously reported in [60, 134, 135]. It should be kept in mind that the final goal in the detection of molecules or the generation of single photons is to realize bright sources out of single quantum emitters [83]. Thus the figure of merit is not the enhancement factor (the gain) but the fluorescence count rate per emitter (the signal).

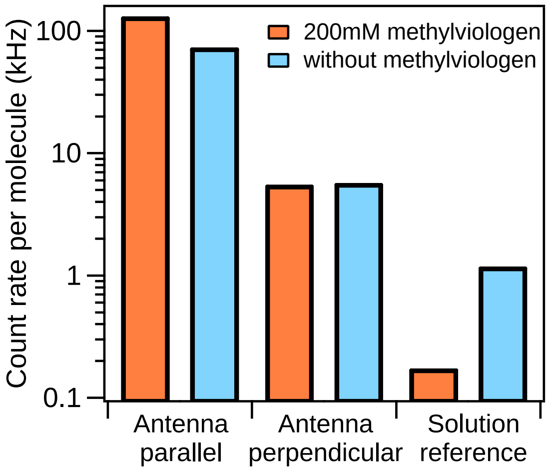

Figure 4.11: Comparison of the detected fluorescence brightness per molecule for the different experimental configurations with and without the chemical quencher. The excitation power is 10 μW at 633 nm, the fluorescence is integrated over the 650-690 nm range.

To investigate the performance of our nanoantenna design, Figure 4.11 compares the detected count rates per molecule for the different experimental configurations with and without the chemical quencher. Remarkably, the brightest count rate is found in the case of the low quantum yield emitter and the nanoantenna. These results appear of high relevance for the development of advanced single molecule sensing, bright single-photon sources for quantum information processing, and light emitting devices.

4.5 Applications of Nanoantenna-in-box

Molecular concentration determination

We tested the “antenna-in-box” for measuring local sample concentrations in the micromolar regime. We used two nanoantennas of different gaps, one with 14 nm and other with 18 nm gap. Then series of FCS curves were recorded on the same nanoantenna for increasing concentrations of the Alexa Fluor 647 probe (Fig. 4.12). The number of molecules in the gap region N^* follows nicely a linear relationship with the fluorophore concentration (Fig. 4.12b), validating the FCS analysis. The slope of the curve quantifies the observation volume to 70 zL for the 14 nm gap and 128 zL for the 18 nm gap.

Importantly, we show here that our design can accurately quantify the number of detected molecules inside the hot spot and the concentration can be raised above 20 μM while still having less than one molecule detected in the hot spot.

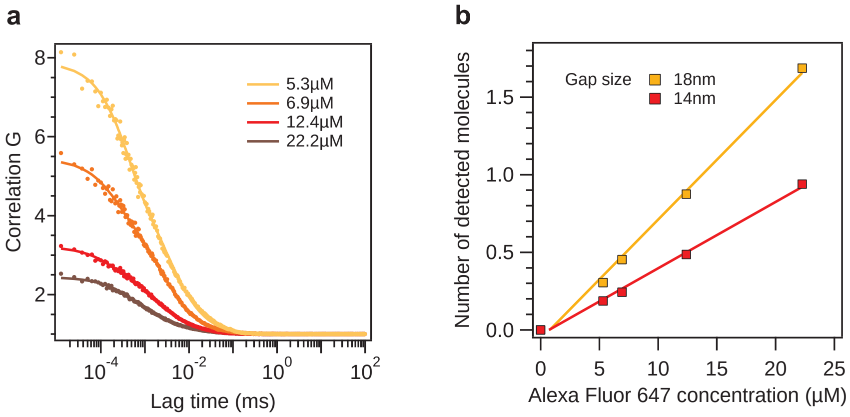

Figure 4.12: **Local concentrations measured at physiological conditions with an "antenna-in-box".** (a) Fluorescence correlation functions for decreasing concentrations of fluorescent probes, for a nanoantenna of 14 nm gap. (b) Number of detected molecules versus the molecular concentration for two nanoantennas of different gap sizes.

Applicability to biomolecular samples

The antenna-in-box platform can be successfully applied to investigate a broad range of biomolecules. Table 4.4 lists the different samples used and their fluorescent label. We consider the cellular protein Annexin 5b labeled with Cyanine5 fluorescent dye, double stranded DNA constructs of 11, 40 and 51 base pairs (bp) labeled with Atto647N, and the cell wall surface protein Protein A labeled with Alexa Fluor 647. Annexins, DNA and Protein A are widely used in biological research and pharmaceutical applications at industrial scale. The choice of fluorescent labels (Alexa 647, Cyanine5 and Atto647N) covers the most commonly used probes for the red spectral region. The samples also include the use of the restriction enzyme PstI to cleave the 51bp DNA construct into shorter strands (see Chemicals in section 4.3).

The reference data corresponding to the confocal case is shown in Fig. 4.13a, and a graphical comparison with/without antenna is shown in the case of Annexin 5b in Fig. 4.13b. Figure 4.14a compares the correlation functions obtained with the different molecular samples on an "antenna-in-box" of 15 nm gap size. A gradual shift of the correlation data to longer times is observed as the molar mass of the sample is increased. Figure 4.14b plots the average residence time in the nanoantenna volume versus the molecular hydrodynamic radius. For the different samples tested, the average residence time in the nanoantenna is found to increase proportionally to the hydrodynamic radius.

For proteins larger than the antenna gap size, exclusion effects and significant deviations from

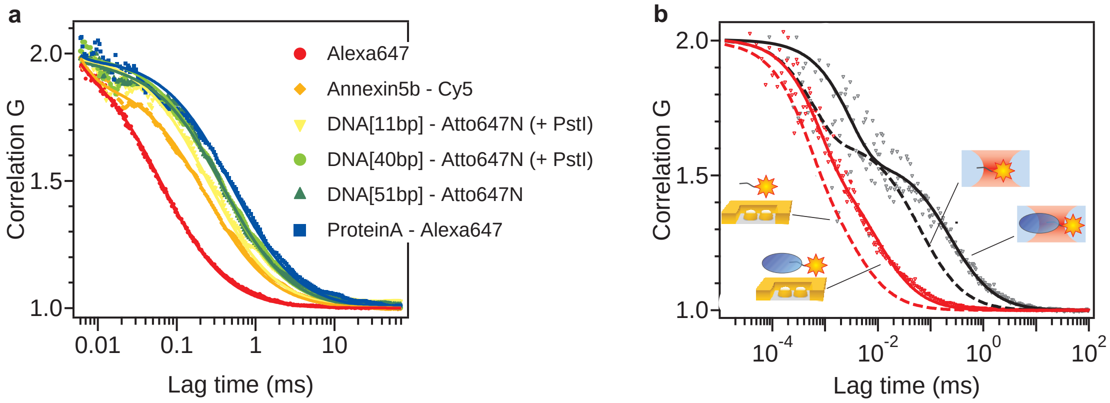

Figure 4.13: (a) Normalized FCS curves measured in confocal illumination setup. (b) Normalized FCS curves for Annexin A5b labeled with Cyanine-5. Red curves are for the “antenna-in-box” with 15 nm gap size, black curves show the reference data for the confocal set-up. The dashed lines are the reference correlation functions for the free dye.

the linear trend are expected. The observed linear dependence also indicates that our data are not compromised by photobleaching, local heating or surface binding. While in most experiments dealing with fluorescence dyes or certain biomolecules, molecular adhesion to the metal remains minimal, some diffusing proteins might exhibit unspecific binding to the antenna. We explored this effect and in fact found that protein A exhibits unwanted adhesion to the antenna. We conveniently solved this problem by adding a polysorbate surfactant in the solution containing the sample. Figure 4.15 compares the experimental data obtained on Protein A - Alexa647 samples respectively with and without polysorbate surfactant (Tween 20, Sigma-Aldrich) at 1% concentration. The other experimental conditions are identical between both cases: nanoantenna 15 nm gap, protein A concentration 1 μM, excitation power 10 μW. At 1 μM concentration of fluorescent probe, we await about 0.2 molecules in the nanoantenna detection volume. Without Tween 20, the fluorescence time trace shows several intense bursts, and the FCS data bears long correlation time, typically around 10 ms or more. These features indicate significant sticking of the protein A sample to the nanoantenna surface.

These obtained data are used to calibrate the hydrodynamic radius (used as horizontal axis in Fig. 4.14b). FCS quantifies the translational diffusion time τ_d, which relates to the diffusion coefficient D by $\tau_d = w^2/4D$, where w is the transversal waist (radius) of the confocal detection volume, calibrated independently to $w = 275$ nm. The hydrodynamic radius R_h is then given by the Stokes-Einstein equation:

$$D = \frac{k_B T}{6\pi\eta R_h} \tag{4.3}$$

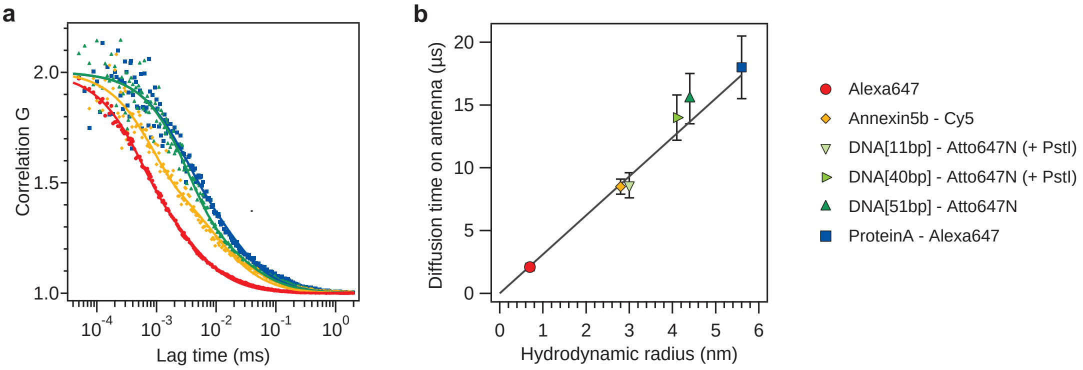

Figure 4.14: **Applicability of the “antenna-in-box” to detect and discriminate individual biomolecules at 10 μM concentrations.** (a) Normalized fluorescence correlation functions measured on an ”antenna-in-box” of 15 nm gap size, with excitation polarization parallel to the antenna axis. The samples are Alexa Fluor 647 free dye (red, molar mass 1.3 kDa), Annexin 5b (orange, molar mass 36 kDa), 51 base pairs double stranded DNA (green, molar mass 32.1 kDa) and Protein A (blue, molar mass 56 kDa). The points correspond to experimental data and the solid lines to a numerical fit. (b) Average residence times in the nanoantenna observation volume versus the molecular hydrodynamic radius for the different biomolecules. The black line is the trend expected from Brownian diffusion.

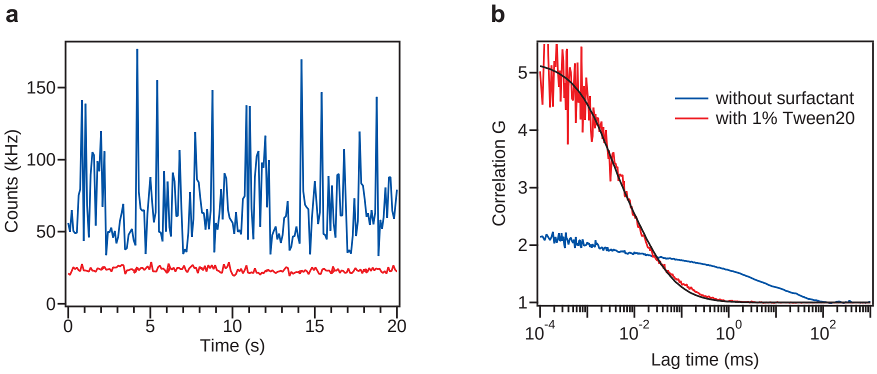

Figure 4.15: **Influence of the surfactant for protein A studies.** (a) Fluorescence time trace (binning time 100 ms) and (b) FCS correlation function for a nanoantenna with 15 nm gap size acquired on Protein A - Alexa647 sample respectively without surfactant (blue curves) and with 1% of Tween 20. Protein A concentration is 1 μM, and there is no methyl viologen used here. The excitation power is 10 μW, with polarization parallel to the nanoantenna axis.

where k_B is Boltzmann’s constant, T the absolute temperature, and η the solvent’s viscosity. From the Stokes-Einstein equation, it is straightforward to relate the FCS diffusion time to the hydrodynamic radius:

$$\tau_d = \frac{3\pi\eta w^2}{2k_B T} R_h \tag{4.4}$$

Sample	Molar mass (kDa)	Confocal transient time (μs)	Hydrodynamic radius (nm)	Nanoantenna transient time (μs)
Alexa647	1.3	61	0.7	2.1
Annexin5b-Cyanine5	36	240	2.8	8.5
DNA[11bp]-Atto647N (+PstI)	7.5	258	3.0	8.6
DNA[40bp]-Atto647N (+PstI)	25.3	360	4.1	14
DNA[51bp]-Atto647N	32.1	385	4.4	15.5
Protein A-Alexa647	56	490	5.6	18

Table 4.4: Molecular constructs detected with the “antenna-in-box”. see Fig 4.14.

The “antenna-in-box” can thus be readily used to determine relative diffusion coefficients at high physiologically relevant concentrations, and to distinguish between different fluorescent species based on their diffusion properties. We note that these studies were performed in the absence of the quencher to avoid potential chemical reactions with the protein.

Fast FCS

Nanoantennas enable fast correlation analysis with improved accuracy thanks to the high count rates per molecule. The key parameter to determine the statistical noise in the FCS data is not the total detected fluorescence, but instead the product of the fluorescence brightness per molecule Q times the square root of the total experiment acquisition time T_{tot} [136]. To demonstrate the gain brought by the nanoantenna, 100 successive FCS measurements of $T_{tot} = 5$ s duration were performed. Figure 4.16a and b display FCS curves obtained after only 5 s integration respectively with the confocal set-up and the nanoantenna. The grey shaded regions represent the standard deviation, and black lines are mean values. A striking reduction in the noise distribution with the nanoantenna is clearly apparent by comparing Fig. 4.16a and b. Figure 4.16c presents experimental histograms for the normalized amplitude of the correlation function $G(0)$ obtained after 5 s integration time. In the case of the confocal setup, $G(0)$ is estimated by averaging the first 50 channels of the correlator (lag times up to 1 μs), while for the nanoantenna $G(0)$ is estimated only from the first correlator channel with lag time 12.5 ns. Despite this much shorter channel width, the histograms found with the nanoantenna have still muchg narrower statistical distribution thanks to the large fluorescence enhancement brought by the antenna. Since the statistical accuracy in FCS curves scales as the product $Q\sqrt{T_{tot}}$, a thousand-fold Q increase with a nanoantenna amounts to a potential

10^6-fold reduction of the experiment duration, while preserving the statistical quality of the FCS data. Such striking reduction of the integration time opens the way for ultrafast single molecule FCS analysis and screening for huge libraries of compounds within a limited time.

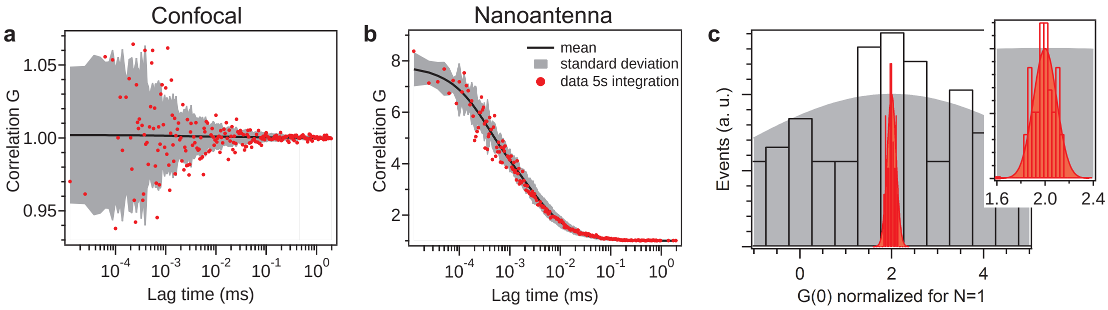

Figure 4.16: (a) Fluorescence correlation curves for the confocal set-up and the nanoantenna (b) with data points corresponding to the FCS curves obtained after only 5 s integration. The grey shaded regions represent the standard deviation obtained after repeating the experiment 100 times, black lines are mean values. The Alexa Fluor 647 concentration is 5 μM, with 200 mM methyl viologen and 10 μW excitation power. (c) Experimental histograms and Gaussian fits for the normalized amplitude of the correlation function $G(0)$ obtained after 5 s integration time with the nanoantenna (red) or the confocal set-up (grey).

4.6 Conclusion

Using the dominant fluorescence emission from the nanoantenna gap region together with background screening afforded by the surrounding box, we isolated detection volumes down to 58 zL, accompanied by a 1100-fold fluorescence enhancement. The “antenna-in-box” concept represents an optically efficient, and robust platform for performing a wide variety of biochemical studies with single molecule resolution at physiologically-relevant high concentrations. This preludes a new class of nanoscale biomolecular studies to investigate enzymatic reactions [45, 46], and nanoscale composition of live cell membranes [20, 137].

5 Self Assembly of gold nanoparticles for enhanced single molecule detection

In order to achieve our goal to reduce the effective detection volume and enhance the fluorescence signal at high concentrated solution, gold nanoparticles have a strong appeal for practical applications to detect fluorescent molecules in solution owing to their large availability, low intrinsic cost, and tunable spectral response. However, two technical issues are challenging the applications: (i) the large contributions in the fluorescence signal from molecules tens of nanometer away from the nanoparticles and (ii) molecular binding to the metal. Quantifying the near-field volume where the electric field intensity is enhanced together with the average fluorescence enhancement over this volume is of high interest, yet quantitative estimates for fluorescent molecules in solution are still lacking.

This chapter is divided into two sections. In the first section we demonstrate the use of individual spherical gold nanoparticles to perform enhanced single molecule fluorescence analysis in solutions at high (micromolar) concentrations. In the next section we show the experimental outcomes on dimers and trimers of gold nanoparticles of diameter 80 nm.

5.1 Individual Gold nanoparticles

We use individual spherical gold nanoparticles to perform enhanced single molecule fluorescence analysis in solutions at high (micromolar) concentrations. Figure 5.1a and b present a schematic of the experimental configuration together with a numerical computation of the electric field intensity near a 80 nm gold nanoparticle illuminated at 633 nm. Nanoparticles diameters ranging from 60 to 150 nm are used to tune the local surface plasmon resonance (LSPR) across the fluorescence excitation and emission spectra (Fig. 5.1c). At the targeted concentration of fluorescent molecules of 10 μM, the 0.5 fL confocal detection volume (diffraction-limited) contains about 3000 molecules, while only a few molecules are expected to be in the sub-attoliter near-field volume around the nanoparticle. Hence, the collected fluorescence signal is a sum of two contributions: the enhanced fluorescence from a few molecules in the nanoparticle near-field plus a fluorescence background from several thousands of freely

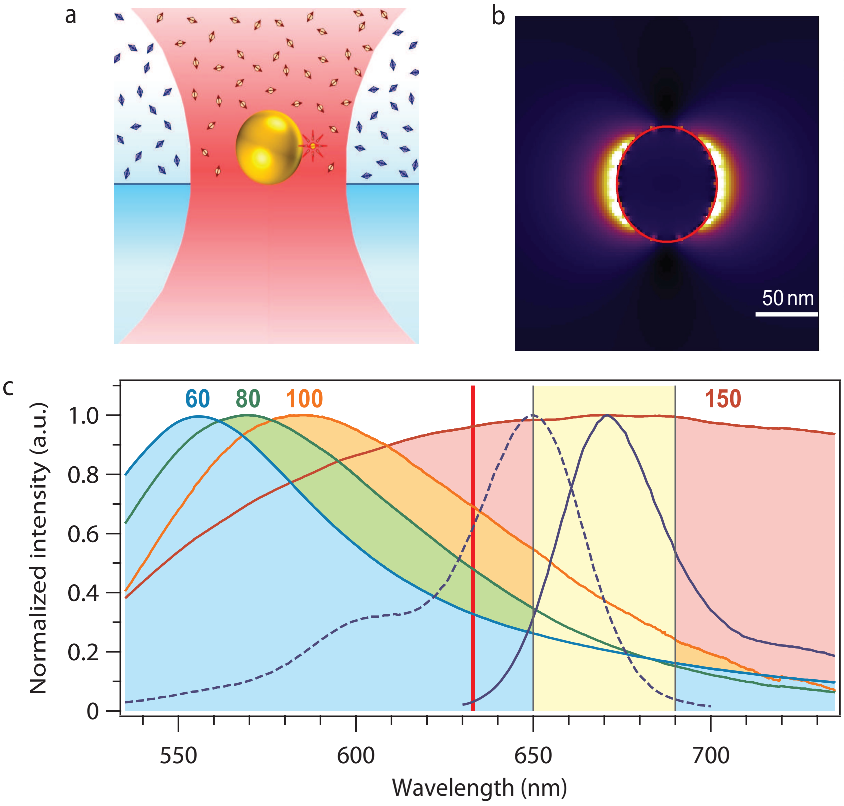

Figure 5.1: (a) Gold nanoparticle on a glass substrate for enhanced single molecule analysis at high concentrations. (b) Finite-difference time-domain computation of excitation intensity enhancement near a 80 nm gold nanoparticle. The incoming light is horizontally polarized at a wavelength of 633 nm. (c) Normalized experimental scattering cross-section of the nanoparticles (color-shaded curves, the label on top on the graphs indicates the nanoparticle diameter in nm). The dashed and solid dark blue lines indicate the normalized absorption and emission spectra of Alexa Fluor 647 dye. The vertical lines indicate the 633 nm laser line used for excitation and the 650-690 nm region used for fluorescence detection.

diffusing molecules within the confocal volume. To discriminate between these contributions, we use emitters with low quantum yield and take advantage of the higher fluorescence enhancement factors obtained with them [60, 62]. We add 200 mM of methyl viologen to the solution containing the Alexa Fluor 647 dyes to quench the dye quantum yield to 8%. Using methyl viologen to reduce the quantum yield plays very crucial role in background screening as we have also seen in the case of nanoantenna-in-box case in chapter 4. Although in the case of metal nanoparticles this becomes even more important owing to the fact that there is no metal aperture box surrounding the antenna as in the case of antenna-in-box to provide further background screening.

5.1.1 Materials and Methods

We use commercial gold nanoparticles (BBI Solutions) of calibrated diameters ranging from 60 to 150 nm with a typical dispersion below 10% in diameter [82]. The nanoparticles are diluted in pure water, dispersed and dried on a glass coverslip. The dilution is optimized to isolate single nanoparticles, which is confirmed by SEM images (Fig. 5.2) and also with confocal laser scanning and checking the invariance on the fluorescence results upon turning the linear polarization orientation of the excitation laser beam. The nanoparticle sample is covered by the solution containing Alexa Fluor 647 fluorescent dyes at micromolar concentrations together with 200 mM of methyl viologen (1,1'-Dimethyl-4,4'-bipyridinium dichloride). The experimental set-up is based on a confocal inverted microscope with a 40x 1.2NA water-immersion objective. The excitation source is a He-Ne laser at 633 nm with 10 μW excitation power. The details of the experimental setup can be found in the Chapter 3. Positioning the nanoparticle at the laser focus spot is obtained with a three-axis piezoelectric stage.

The analysis of the FCS data considers two species with different fluorescence brightness: N^* molecules in the nanoparticle near-field with brightness Q^*, and N_0 background molecules with brightness Q_0 diffusing away in the confocal volume. For the FCS analysis in the case of the nanoantenna, the number of emitters and brightness N_0, Q_0 for the molecules diffusing away from the hot spot are fixed according to the values found at the glass-water interface without nanoparticle, corrected by a factor of $C = 1-(d/w)^2$ to account for the screening induced by the nanoparticle (d is the nanoparticle diameter, w=280 nm is the laser beam waist at focus). Typically, C amounts to 0.95 to 0.87 for the nanoparticles of size 60 to 100 nm. In the FCS analysis, we also set $s = 0.2$, as this parameter was found to have a negligible influence on the estimates for N^* and Q^* which are the main goals.

5.1.2 FCS analysis in the near-field of a single metal nanoparticle

As we have discussed, in the case of single gold nanoparticles it is crucial to treat the background signal and extract the enhanced fluorescence signal stemming from the nanoparticle near field from the background generated in the confocal volume. Below we provide a another

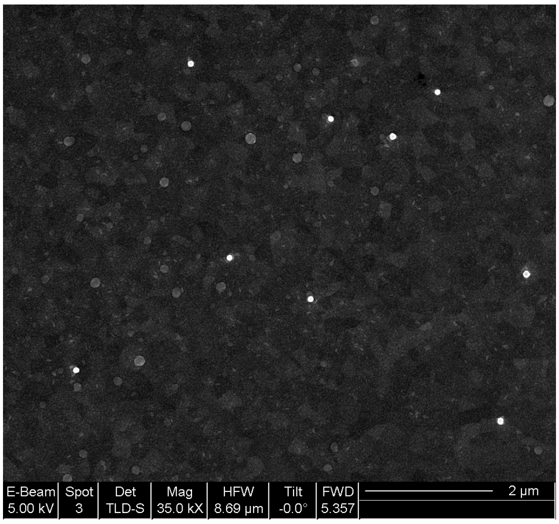

Figure 5.2: Scanning electron microscopy image of 80 nm diameter gold nanoparticles deposited on a glass coverslip with ITO coating.

method to tackle this issue.

The temporal fluctuations $F(t)$ of the fluorescence intensity signal are recorded to compute the autocorrelation

$$G(\tau) = \frac{\langle F(t).F(t+\tau)\rangle}{\langle F(t)\rangle^2} \tag{5.1}$$

where τ is the delay (lag) time, and $\langle . \rangle$ stands for time averaging. Here the fluorescence signal comes from two different regions within the confocal volume: one from the N^* molecules near the nanoparticle and second from the N_0 molecules tens of nanometers away from the nanoparticle. The contribution from the latter can be elegantly accounted for as a background correction factor, if the number of molecules in the confocal volume is high enough so as to cancel almost all correlations.

At concentrations exceeding several micromolar, Eq. (5.1) can be approximated by [3, 127].

$$G(\tau) = 1 + \frac{1}{N^*}\left(1 - \frac{B}{F}\right)^2 \left[1 + n_T \exp\left(-\frac{\tau}{\tau_{b_T}}\right)\right] g(\tau) \tag{5.2}$$

with

$$g(\tau) = \frac{1}{(1+\tau/\tau_d)\sqrt{1+s^2\tau/\tau_d}} \tag{5.3}$$

and

$$B = N_0 \times CRM_0 \tag{5.4}$$

Here $F = N^* \times CRM^* + N_0 \times CRM_0$ is the total detected fluorescence intensity, B the background noise, n_T the dark state amplitude, τ_{b_T} the dark state blinking time, τ_d the mean translational diffusion time, s the ratio of transversal to axial dimensions of the analysis volume, CRM_0 the average count rate per molecule in the confocal volume without the nanoparticle and CRM^* the count rate per molecule in the near field vicinity of the nanoparticle.

For very small durations of counting interval compared to diffusion time ($\tau << \tau_d$), Equation (5.2) can be expressed as

$$G(0) = 1 + \left(1 - \frac{B}{F}\right)^2 \frac{1 + n_T}{N^*} = 1 + \left(\frac{1}{1 + \frac{N_0}{N^*} \times \frac{CRM_0}{CRM^*}}\right)^2 \frac{1}{N^*} \tag{5.5}$$

In the denominator of the equation above, one can recognize the fluorescence enhancement factor $\eta_F = CRM^*/CRM_0$, together with a factor N_0/N^* which accounts for the detection volume reduction. As the nanoparticle volume is negligible respective to the confocal volume and as the focus is set close to the glass-water interface, we approximate N_0 as the half of the number of molecules N_{conf} for the diffraction-limited confocal volume. Hence the ratio N_0/N^* becomes $N_0/N^* = N_{conf}/2N^* = R_v/2$, where R_v is the reduction in the confocal detection volume achieved in the near-field of the nanoparticle. Henceforth, Eq. (5.3) can be modified as

$$G(0) = 1 + \left(\frac{1}{1 + R_v/2\eta_F}\right)^2 \frac{R_v}{N_{conf}} \tag{5.6}$$

For single gold nanoparticles, the value of R_v is obtained from the numerical simulations.The values of R_v for 150 nm is 360, for 100 nm is 1100, for 80 nm is 2000 and for 60 nm is 5300. Now the near-field volume around the nanoparticle V^* can be quantified as

$$V^* = \frac{\left(\int |E|^2 dV\right)^2}{\int |E|^4 dV} = 4\pi w^2 d \tag{5.7}$$

where the electric field amplitude polarised along the x-axis around the nanoparticle is approximated by

$$E(x, y, z) = E_{max} \exp\left(-\frac{x}{2d}\right) \exp\left(-\frac{y^2 + z^2}{w^2}\right) \tag{5.8}$$

From the value of $G(0)$ measured by FCS and the computed value of R_v, we can deduce the value of η_F by inverting Eq. (5.6)

$$\eta_F = \frac{\left[(G(0) - 1)N_{conf}\right]^{1/2} (R_v/2)}{R_v^{1/2} - \left[(G(0) - 1)N_{conf}\right]^{1/2}} \tag{5.9}$$

This expression provides an estimate for the value of the fluorescence enhancement factor η_F

based on the FCS amplitude and the simulated value of R_v.

Lastly, to check the validity of this approach, we calculate the background value as $B = F - N^* CRM^* = F - \left(N_{conf}/R_v\right)\left(\eta_F CRM_0\right)$. After this we do the noise correction during the fitting of the experimental data based on the three-dimensional Brownian diffusion model as given in Eq. (5.2) and Eq. (5.3). We obtain the corrected values of number of molecules ($\tilde{N}^*$) and the count rate per molecule ($\widetilde{CRM}^*$) and calculate back the experimental values of volume reduction, $\tilde{R_v} = N_{conf}/\tilde{N}^*$ and fluorescence enhancement, $\tilde{\eta}_F = \widetilde{CRM}^*/CRM$. Finally we compare the estimated values (R_v and η_F) with the experimental values ($\tilde{R_v}$ and $\tilde{\eta}_F$).

5.1.3 Results and Discussion

Confocal experiments on a solution at 4.5 μM fluorophore concentration yield a large fluorescence intensity with reduced temporal fluctuations (Fig. 5.3(a)), corresponding to a weak correlation amplitude of 8×10^{-4} (Fig. 5.3(b)). Fitting the confocal FCS data indicates an average number of $N_{conf} = 1330$ molecules with a diffusion time of 65 μs, as expected for the 0.5 fL detection volume calibrated previously and the 4.5 μM concentration. The brightness per molecule at 10 μW excitation power with 200 mM methyl viologen is $Q_{conf} = 0.14$ kHz. Experimental results are summarized in Tab. 5.1. FCS measurements were taken for several individual gold nanoparticles of diameter ranging from 60 to 150 nm to quantify the fluorescence enhancement factor and the near-field detection volume. The results are summarized in the graphs presented in Fig. 5.4(a) and 5.4(b), together with estimates of the near-field detection volume derived from finite-difference time-domain simulations using the approach described in [138]. At least 10 different nanoparticles are tested for each diameter. The error bars displayed in Fig. 5.4 indicate the standard deviations of our measurements.

Performing FCS experiments with a 80 nm spherical gold nanoparticle provides correlation amplitudes about 12 times higher with significantly improved signal-to-noise ratio. FCS analysis quantifies an average number of $N^* = 0.74$ molecules in the 80 nm nanoparticle near-field with brightness $Q^* = 8.9$kHz. This molecular brightness corresponds to a fluorescence enhancement of $Q^*/Q_{sol} = 64$ times. Given the calibrated Alexa concentration of 4.5 μM, we relate the $N^* = 0.74$ molecules in the nanoparticle near-field to a detection volume of 270 zL (1zL = 10^{-21}L), or equivalently a detection volume reduction of $N_{sol}/N^* = 1800$ times as compared to the diffraction-limited confocal volume. Moreover, a clear reduction of diffusion time down to 11 μs is observed with the nanoparticle, which confirms that the translational diffusion events take place from a sub-diffraction volume.

Figure 5.4(a) clearly indicates an optimum diameter around 80 nm for the highest fluorescence enhancement factor. Remarkably, the 150 nm nanoparticle diameter for which the LSPR wavelength coincides with the peak fluorescence emission wavelength (Fig. 5.1(d)) does not provide the highest fluorescence enhancement. We find that the optimum fluorescence enhancement appears when the emission wavelength is red-shifted from the LSPR wavelength. This follows from the trade-off that must be found between radiative and non-radiative rates

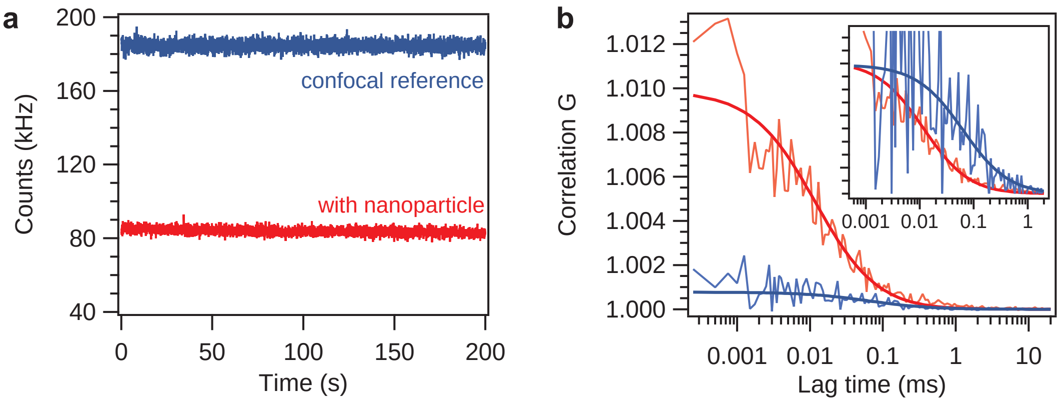

Figure 5.3: (a) Fluorescence time trace and (b) FCS correlation functions for the reference confocal (blue) and the 80 nm nanoparticle (red). Alexa Fluor 647 concentration is 4.5 μM, with 200 mM of methyl viologen as chemical quencher. Thick lines are numerical fit of the data using Eq. (1). The insert displays normalized FCS traces.

	Solution reference	80nm nanoparticle
$G(0)-1$	8×10^{-4}	9.6×10^{-3}
N	1330	0.74
Q (kHz)	0.14	8.9
τ_d (μs)	65	11

Table 5.1: Fitting parameter results for the FCS curves in Fig.5.3(b).

enhancement to achieve high fluorescence enhancement [139]. As predicted numerically [140, 141], the peak wavelength for enhanced non-radiative decay rate coincides with the LSPR wavelength but then drops rapidly towards the red side of the LSPR, while the radiative rate has a longer tail towards the red. Consequently, the quantum yield bears a more pronounced enhancement for wavelengths red-shifted as compared to the LSPR (see figure 5.9.

Validity check of FCS analysis approach and influence of dye concentration

We perform a series of experiments to record FCS curves for increasing concentrations of fluorescent probe (Fig. 5.6(a)) using 100 nm diameter gold nanoparticle set at the microscope focus. We obtain that the number of molecules in the near-field region N^* follows a linear relationship with the fluorophore concentration (Fig. 5.6(b)). It demonstrates that our approach can accurately quantify the number of detected molecules in the concentration regime exceeding 20 μM, and provide single molecule sensitivity at relevant physiological

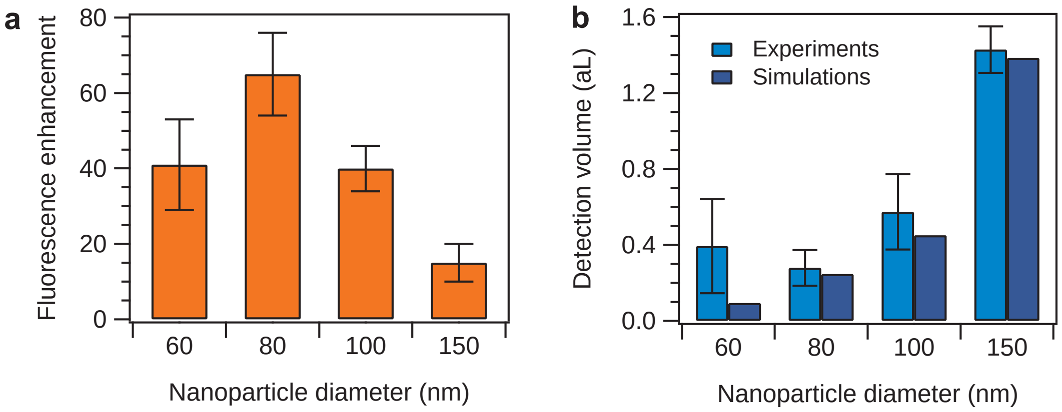

Figure 5.4: (a) Fluorescence enhancement for different diameters of gold nanoparticle and near-field detection volume (b).

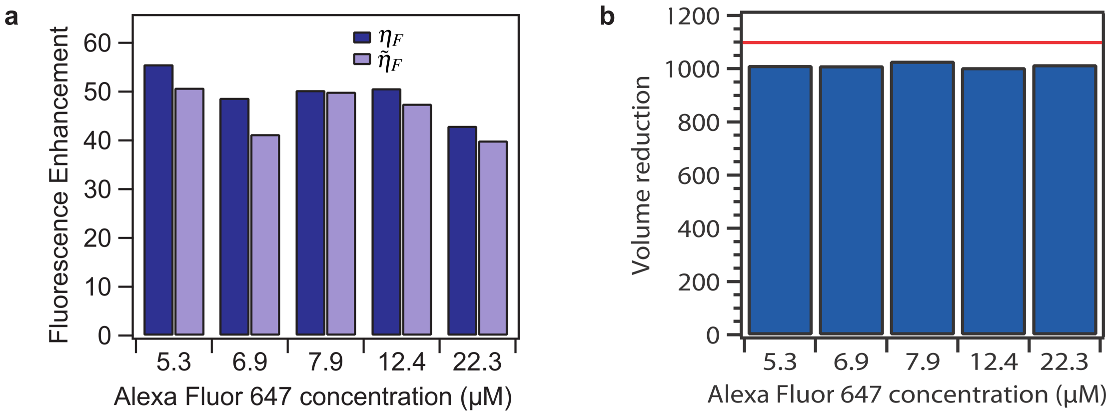

Figure 5.5: (a) Fluorescence enhancement factor for 100 nm gold nanoparticle as function of fluorophore concentration for the two methods. (b) Volume reduction as function of fluorophore concentration for 100 nm gold nanoparticle (red line corresponds to the simulated value of volume reduction).

concentrations.

The estimated values of η_F according to Eq. (5.9) and the fitted values after background correction, $\tilde{\eta_F}$, are compared for these concentrations and plotted as Fig.5.5a. It is apparent that the values are quite correlated for a wide range of high concentration of fluorophore and converge to similar values within experimental errors.

After quantifying the average number of molecules in confocal mode solution, N_{conf}, and in the near field of nanoparticle, N^* (after background correction) we compute the reduction in volume for the range of concentrations shown in Fig. 5.5b and compare it with the simulated volume reduction for 100 nm gold nanoparticle ($R_v = 1100$). We find it to be consistent for the

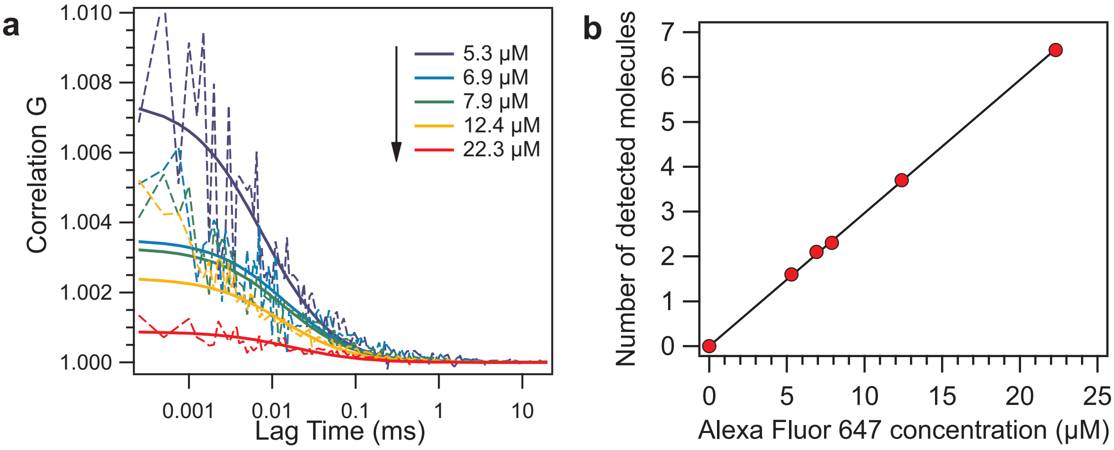

Figure 5.6: (a) Fluorescence correlation functions for increasing concentrations of fluorescent probes using a 100 nm diameter gold nanoparticle. (b) Number of detected molecules in the nanoparticle near-field versus the molecular concentration.

dataset of varying concentrations and it proves that we can efficiently use the background correction methodology to quantify the fluorescence enhancement factor and volume reduction. As an integration of our previous related study, we have found that the approach is also valid with gold nanoparticles of diameters 60, 80 or 150 nm.

Excitation Power dependence

The fluorescence count rates per molecule measured by FCS are plotted as function of excitation power in Fig 5.7 for the two cases of (i) open solution (no nanoparticle), (ii) 100 nm gold nanoparticle. It is apparent that the nanoparticles influentially enhance the fluorescence emission. The experimental points are numerically fitted following the general model of the fluorescence count rate $CRM = AI_e/(I + I_e/I_s)$, where I_e is the excitation power, I_s the saturation power, and A is a constant proportional to the molecular absorption cross section, quantum yield, and setup collection efficiency. After fitting, the parameters are A = 1.3 kHz/μW and $I_s = 15\mu W$. In the experiments, we used 10 μW excitation power to avoid entering into the saturation regime.

Quantum Efficiency Enhancement

Below the fluorescence saturation regime, three effects can contribute to the observed fluorescence enhancement [124]: An increase local excitation intensity, an increase in the effective quantum efficiency and an increase in the collection efficiency due to modification of the radiation pattern thanks to the antenna redirection. The latter phenomenon can be excluded as the nanoparticle diameter is much below the half of the wavelength, the nanoparticle is

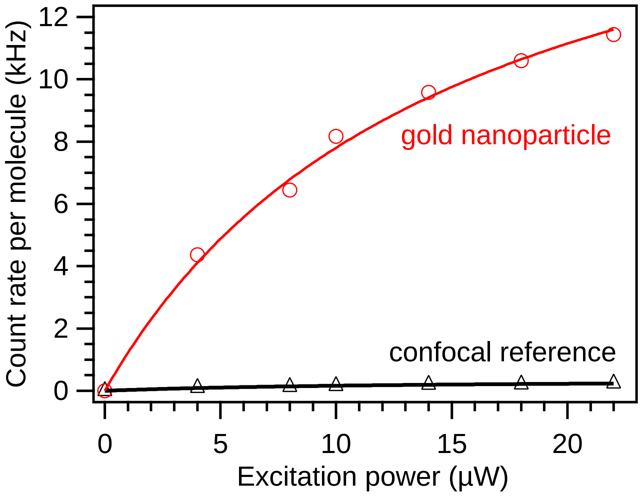

Figure 5.7: Fluorescence count rate per molecule detected in the case of 100 nm gold nanoparticle and confocal reference (open solution).

expected to radiate as a dipole, thereby not providing any significant directivity gain [56]. To quantify the excitation intensity enhancement, we have performed numerical simulations of the excitation electric field intensity using finite difference time domain FDTD method. Typical results are displayed in Fig 5.8, and indicate excitation enhancement higher that 20-fold in the near field of the nanoparticle.

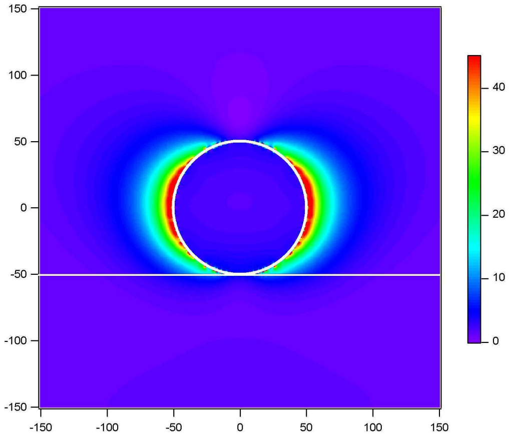

Figure 5.8: Finite-difference time-domain computation of excitation intensity enhancement near a 100 nm gold nanoparticle on a glass substrate. The incoming light is horizontally polarized at a wavelength of 633 nm and incoming from below the nanoparticle. Horizontal and vertical dimensions are in nm.

To get more insight on the enhancement of the quantum efficiency, we have performed numerical simulations based on the method described in [140]. We consider a point dipole source set a 10 nm distance from the nanoparticle (this distance provides the highest quantum efficiency enhancement as a trade-off between radiative enhancement and quenching losses to the metal [139,141]). The results are averaged to represent an isotropic (random) orientation of the dipole emitter. Figure 5.9 summarizes our results, and indicate an optimum diameter of about 100 nm to maximize the quantum efficiency enhancement. We obtain a quantum efficiency gain of about 3-fold in the spectral region used for fluorescence detection, which in product of the 20-fold excitation intensity enhancement comes in good agreement with the 50-fold detected fluorescence enhancement.

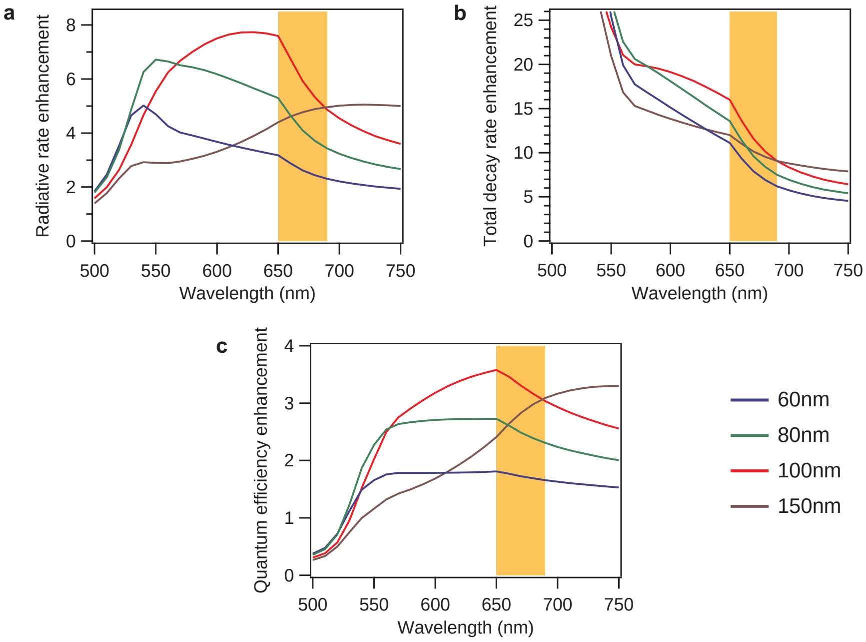

Figure 5.9: Numerical computations of the radiative rate enhancement (a), the total decay rate enhancement (b) and the quantum efficiency enhancement (c), for a dipole of random orientation set at 10 nm distance from the nanoparticle surface. The color coding of the traces are common to all graphs, and the orange shaded region represents the spectral range used for fluorescence detection. The reference quantum yield of the emitter is 7.5%, which corresponds to our experiments in the presence of 200 mM of methyl viologen.

5.2 Gold nano-dimers and trimers

In the previous section we investigated single gold nanoparticle's antenna properties in order to get enhanced fluorescence signal and smaller detection volume. In this section we are analysing the self assembly of gold nano-dimers and trimers following the similar approach.

5.2.1 Sample Preparation

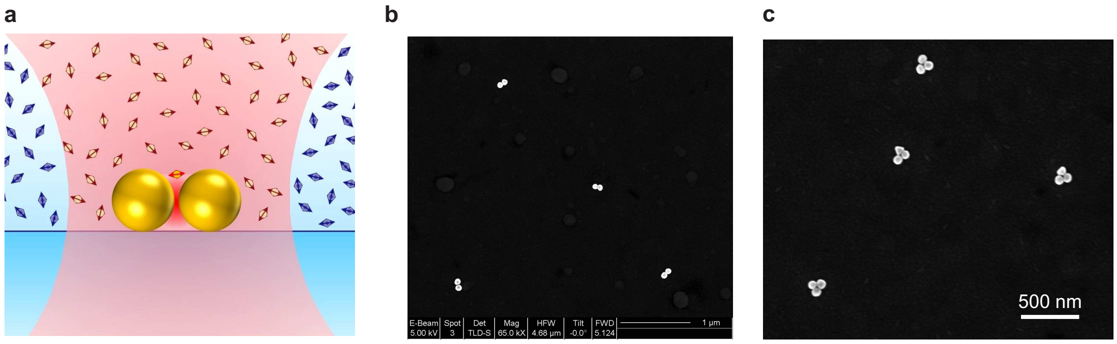

Figure 5.10: (a) Schematic of dimer antenna of gold nanoparticles of diameter 80 nm. (b) and (c) shows the SEM images of dimers and trimers respectively.

We have used the commercial gold nanoparticles (BBI Solutions) of 80 nm diameter as mentioned earlier in the case of single nanoparticle experiment. The nanoparticles are diluted in pure water , dispersed and dried on an ITO (Indium Tin Oxide) cover slide to obtain dimers and trimers. Figure 5.10a represents the schematic of the experimental configuration in case of the dimers. Figure 5.10b and c, shows the SEM images of dimers and trimers respectively. Fig 5.11 displays the wide field view of SEM image showing several dimers. To perform the FCS experiments, we have used 15 μM concentration of solution containing Alexa Fluor 647 fluorescent dyes together with 200 mM of methyl viologen. The excitation source and power has been kept same as in the case of earlier gold nanoparticle experiments (633 nm He-Ne laser and 10 μW power). Positioning of the dimers and trimers at the laser focus spot is obtained with a three-axis piezoelectric stage. We have performed correlative measurements on dimers and trimers by finding them with SEM and then making marks with FIB method to track them on our confocal microscope setup (for details about our setup see Chapter 3). Since the self assembly of these dimers and trimers have more or less no control, we see variations from one antenna to another, which can be seen in the results provided in the coming section. In order to define the gap-size in the case of dimers and trimers we have used Poly(ethylene glycol) methyl ether thiol (PEG) (Sigma Aldrich) with average molecular weight of 800, as capping agent to the gold nanoparticles. The solution of PEG and gold nanoparticles are diluted together and dispersed and dried on ITO cover slide. We assume that PEG replaces the citrate cover on the gold nanoparticles with thiol agent to bind on the surface of gold nanoparticle. PEGylated gold nanoparticles are reported to have higher average volume diameters depending of their molecular weight [142]. In our case we use PEG thiol with molecular weight (M_n) 800 which has a spacer arm of 6.3 nm that provides 6 nm additional surface on the nanoparticles.

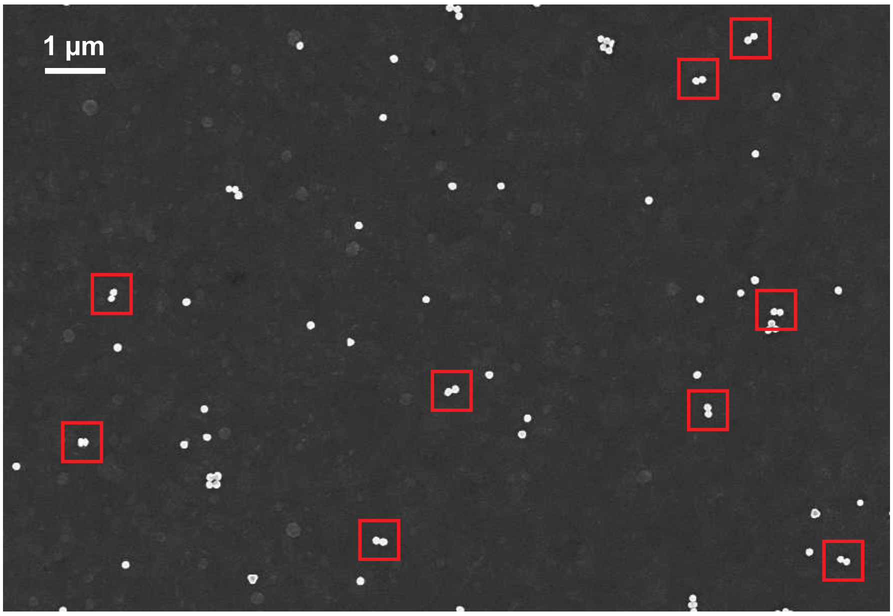

Figure 5.11: SEM image of the self-assembled dimer nanoparticle antennas on ITO substrate. Several dimer antennas are readily identified (highlighted by red boxes).

We have done FCS measurements on five different cases: Dimers (no PEG), Dimers(with PEG), Trimers(no PEG), Trimers(with PEG) and aggregates of gold nanoparticles. We have compared these results with the earlier study of 80 nm gold monomer.

5.2.2 Numerical simulation and spectral analysis

Three dimensional numerical modelling on dimer antennas of 80 nm diameter with a gap size of 6 nm is done based of Mie theory by Nicolas Bonod and Brain Stout of CLARTE group of Institut Fresnel. The 633 nm excitation light is sent parallel to the dimer axis. Figure 5.12a shows the results. For trimers, Finite difference time domain (FDTD) computation of excitation intensity enhancement was performed using Rsoft Fullwave version 6.0. The gold trimer antenna (refractive index = 0.183+2.974i) was located on a glass substrate (refractive index = 1.52). The excitation at 633 nm was launched from the glass side with perpendicular(Fig 5.12b) and parallel polarization (Fig 5.12c). Electromagnetic intensity was measured and averaged in the gap region of trimers.

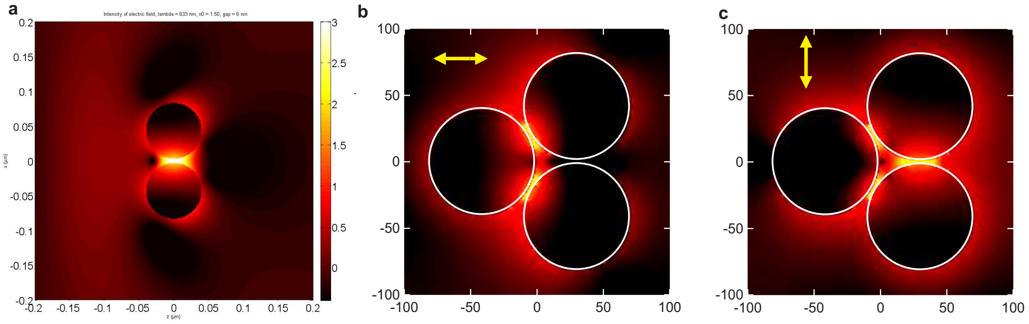

Figure 5.12: **Numerical modelling on dimer and trimer** (a)Mie theory numerical simulation of excitation intensity enhancement inside the 6 nm gap size dimer antenna. (b) and (c) shows the FDTD simulation of excitation intensity enhancement near trimer antenna with perpendicular and parallel excitation polarization, respectively.

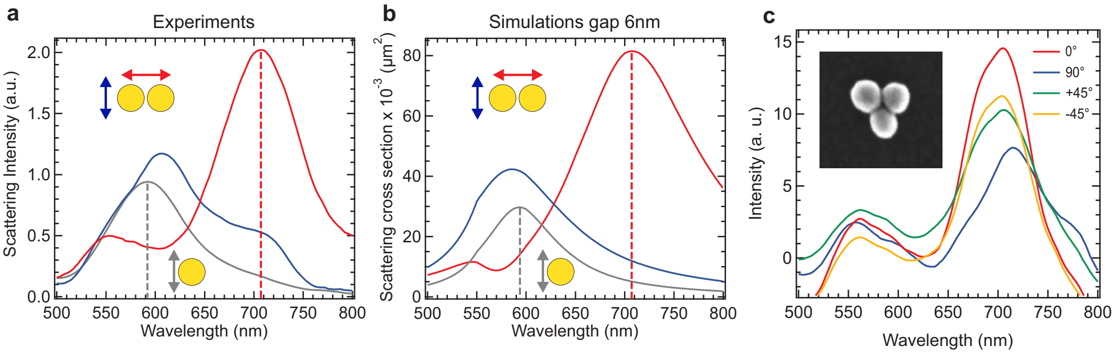

Figure 5.13: **Spectral analysis of Dimers and Trimers** (a)spectral measurements on a typical dimer with excitation parallel(red) and perpendicular (blue) and on monomer of 80 nm diameter (black) (b)Shows the simulated results for a dimer of gap 6 nm. (c) spectra analysis on a trimer at four different excitation polarization angles.

Figure 5.13 displays the spectral analysis of dimers and trimers. We find very good agreement between the experimental and simulated results in case of dimers having gap-size 6 nm (Fig. 5.13a and b). For excitation parallel to the dimer axis (red curve) we see an LSPR peak around 710 nm, whereas in case perpendicular polarization (blue curve) we get almost similar resonance conditions as monomer (black curve). For trimers, the spectral measurements have been done for four excitation polarization (Fig. 5.13c) showing similar behavior, which confirms the symmetry of the trimer antenna. We see two well resolved resonance conditions in this case.

To determine the gap size from the longitudinal plasmon resonance (LSPR) wavelength, computation based of Mie theory is shown in figure 5.14. It displays the LSPR wavelength for a

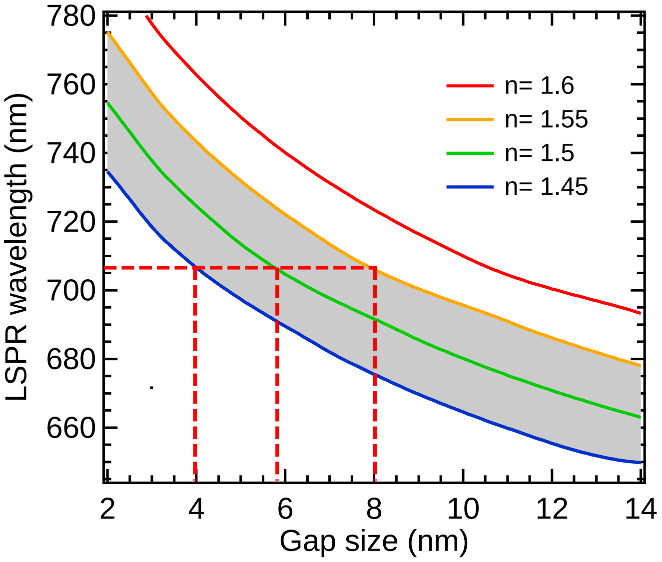

Figure 5.14: LSPR wavelength for a dimer of 80 nm nanoparticles as function of gap size, computed according to Mie Theory.

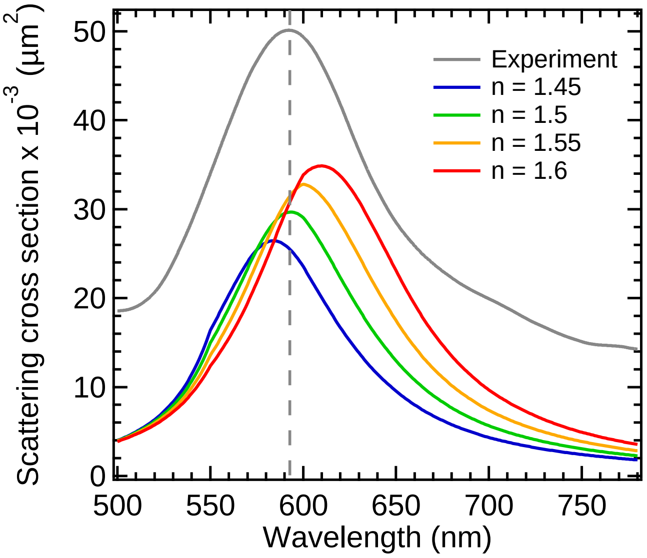

Figure 5.15: Determination of the effective refractive index n_{eff} used in Mie theory computations so as to match the LSPR wavelength of a single 80 nm gold nanoparticles. The experimental scattering spectra (averaged over an ensemble of nanoparticles) is plotter in gray and vertically shifted.

dimer of 80 nm nanoparticles as function of gap size for different effective refractive indexes. We find out that the case of $n_{eff} = 1.5$ is the one that matches best the experimental observations for the scattering spectrum of the dimer (Fig. 5.13a). The dashed horizontal lines indicate the spectral interval of the experimentally observed LSPR values, which corresponds to the gap size estimate of 6±2 nm. In case of single gold nanoparticle of 80 nm, Mie theory computation is done to match the local surface plasmon resonance (LSPR) wavelength (Fig. 5.15). The case $n_{eff} = 1.5$ shows the best match to the experimental data. Additionally, this finding is confirmed by the average between the refractive index of water superstrate (n = 1.33) and the ITO substrate (n = 1.81) at 600 nm.

We performed the spectral analysis on the dimers with PEG spacers in order to find out the influence of PEG environment (see figure 5.16). We see a blue shift in the resonance peak as compared to the dimer antenna without PEG. This blue shift indicates a large gap size of ~ 14 nm according to the calibration graph in Fig. 5.14 and the PEG refractive index of 1.46.

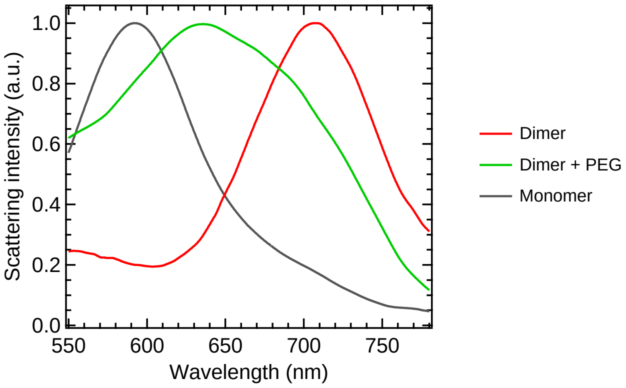

Figure 5.16: Normalized dark-field scattering spectra in the presence of a supplementary PEG spacer surrounding the 80 nm nanoparticles (green line). A significant blue-shift is observed as compared to the dimer antenna without PEG(red line).

5.2.3 FCS analysis in the near field of gold nano-dimers and trimers

For the analysis of FCS data we start with the same consideration of two species with different fluorescence brightness: N_0 background molecules with brightness Q_0 diffusing away from the hot spot of dimer and N^* molecules in the dimer hot spot volume with brightness Q^*. The amplitude of the fluorescence intensity correlation function for $\tau = 0$ can be written as [3]:

$$G(0) = 1 + \frac{N_0 Q_0^2 + N^* Q^{*2}}{N_0 Q_0 + N^* Q^*}(1 + n_T) \tag{5.10}$$

where n_T gives the triplet state amplitude. For total fluorescence intensity signal

$$F = N_0 Q_0 + N^* Q^* \tag{5.11}$$

we get;

$$G(0) = 1 + \frac{N_0 Q_0^2 + (F - N_0 Q_0) Q^*}{F^2}(1 + n_T) \tag{5.12}$$

From here we get

$$Q^* = \frac{F^2\left(\frac{G(0)-1}{1+n_T}\right) - N_0 Q_0^2}{F - N_0 Q_0} \tag{5.13}$$

and

$$N^* = \frac{F - N_0 Q_0}{Q^*} = \frac{(F - N_0 Q_0)^2}{F^2\left(\frac{G(0)-1}{1+n_T}\right) - N_0 Q_0^2} \tag{5.14}$$

Dimers

For dimers we consider $N_\parallel$ and $Q_\parallel$ are the number of molecules and brightness in the hot-spot when the dimer is excited with polarization parallel to the dimer axis. Similarly $N_\perp$ and $Q_\perp$ are the number of molecules and brightness in the hot-spot when the dimer is excited with polarization perpendicular to the dimer axis. In the case of perpendicular excitation we assume that two single 80 nm gold nanoparticles are being excited collectively. Hence we can write $N_\perp = 2 \times N^*_{np}$ and $Q_\perp = Q^*_{np}$ where N^*_{np} and Q_{np^*} are the number of molecules and brightness in the case of single nanoparticle. From our earlier results we know, for 80 nm particle: Reduction volume = $1750\times = R_{v,np}$ and Fluorescence enhancement = $65\times = \eta_{F,np}$. Hence in the case of dimer for perpendicular polarization:

$$N^*_\perp = 2 \times \frac{N_{conf}}{R_{v,np}} \tag{5.15}$$

$$Q^*_\perp = \eta_{F,np} \times Q_{conf} \tag{5.16}$$

where N_{conf} and Q_{conf} are the number of molecules and brightness in the case of confocal reference. From here we can find out the background molecules N_0 and the corresponding brightness Q_0 following the trends of equations 5.11, 5.13 and 5.14

$$N_0 = \frac{(F_\perp - N^*_\perp Q^*_\perp)^2}{F_\perp^2(\frac{G_\perp(0)-1}{1+n_T}) - N_\perp Q_\perp^{*2}} = \frac{(F_\perp - 2\frac{N_{conf}}{R_{v,np}}\eta_{F,np}Q_{conf})^2}{F_\perp^2(\frac{G_\perp(0)-1}{1+n_T}) - 2\frac{N_{conf}}{R_{v,np}}\eta_{F,np}^2 Q_{conf}^2} \tag{5.17}$$

$$Q_0 = \frac{F_\perp^2(\frac{G_\perp(0)-1}{1+n_T}) - N_\perp Q_\perp^{*2}}{(F_\perp - N^*_\perp Q^*_\perp)} = \frac{F_\perp^2(\frac{G_\perp(0)-1}{1+n_T}) - 2\frac{N_{conf}}{R_{v,np}}\eta_{F,np}^2 Q_{conf}^2}{(F_\perp - 2\frac{N_{conf}}{R_{v,np}}\eta_{F,np}Q_{conf})} \tag{5.18}$$

And by knowing the values of N_0 and Q_0 we can find out the number of molecules $N_{\|}^*$ and brightness $Q_{\|}^*$ in the hot spot for parallel polarization;

$$N_{\|}^* = \frac{(F_{\|} - N_0 Q_0)^2}{F_{\|}^2 (\frac{G_{\|}(0)-1}{1+n_T}) - N_0 Q_0^2} \tag{5.19}$$

$$Q_{\|}^* = \frac{F_{\|}^2 (\frac{G_{\|}(0)-1}{1+n_T}) - N_0 Q_0^2}{(F_{\|} - N_0 Q_0)} \tag{5.20}$$

This is our goal to find out number of molecules and brightness in the hot spot when the dimer is excited with a polarization parallel to the dimer axis.

Trimers

In the case of trimers, to find the values of N^* and Q^*, we set the values of N_0 and Q_0 according to the values found at the glass-water interface without nanoparticle, corrected by a factor of $C = 1 - 3 * (d/2w)^2$ to account for the screening induced by the nanoparticle (d = nanoparticle diameter, w = 280 nm is the laser beam waist at focus). Typically the value of C is 0.938 in this case. Hence $N_0 = C \times N_{conf}/2$ and $Q_0 = C \times Q_{conf}$. From here we calculate the values of N^* and Q^* following the equations 5.13 and 5.14.

5.2.4 Results and Discussion

FCS experiments on a solution of 15 μM fluorophore concentration yield a large fluorescence intensity with reduced temporal fluctuations in confocal case (see in Fig 5.17b, the upper trace in black) which corresponds to a weak correlation amplitude of $\simeq 3 \times 10^{-4}$ (Fig 5.17c). Fitting the confocal FCS data indicates an average number of $N_{conf} = 3600$ molecules with a diffusion time of 64 μs, as expected for the 0.5 fL detection volume calibrated previously. The brightness per molecule at 10 μW excitation power with 200 mM methyl viologen is $Q_{conf} = 0.19$ kHz. Figure 5.17b (lower graph) shows the fluorescence time traces for dimer excited with parallel (red) and perpendicular (blue) polarization. Similarly Figure 5.20b displays the time traces in case of four different excitation polarization for trimers. We see large fluctuations in the time traces in comparison to the confocal case.

FCS data (Figure 5.17c and Figure 5.20c) display remarkably higher correlation amplitudes, shorter diffusion times and excellent signal-to-noise characteristics. Such features can only be obtained if a small number of molecule are being observed with high apparent brightness from a small detection volume. Table 5.2 contains the fitting parameter results of all the FCS data shown in Fig 5.17c and 5.20c. In the case of dimer with excitation polarization parallel to the dimer axis, we obtain an average number of $N^* = 0.49$ molecules in the hotspot with brightness

$Q^* = 115.6$ kHz. These values corresponds to a fluorescence enhancement of $Q^*/Q_{conf} = 608$ and a detection volume reduction of $N_{conf}/N^* = 7800$. The influence of excitation laser polarization confirms that the fluorescence signal stems form the dimer antenna's hot spot. These dimer antennas show excellent temporal resolution. In the inset of Fig 5.17c, we see the normalized FCS curves in comparison to the confocal reference. In the case of parallel excitation polarization, the average residence time for molecules in the hot spot amounts to only 2.1 μs, nearly two orders of magnitude shorter than the confocal reference. This huge reduction in time scales highlights the distinction between the molecules in the hot spot and molecules away in the confocal volume. It also indicates that the molecular adhesion to the dimer antenna remains minimal in this case.

	Solution	Dimer(without PEG)		Trimer(with PEG)			
	Reference (confocal)	Parallel Excitation	Perpendicular Excitation	0° Excitation	90° Excitation	+45° Excitation	-45° Excitation
$G(0)-1$	0.00030	0.048	0.007	0.035	0.022	0.031	0.02
N	3600	0.49	4.26	0.78	1.61	1.56	1.44
τ_d (μs)	64	2.1	10	2.0	1.7	1.65	1.6
Q (kHz)	0.19	115.6	11.4	62	41.5	45.3	41.5
Fluorescence Enhancement		608	60	326	197.5	238.3	207.5
Volume Reduction		7800	900	4586	2232.6	2308	2500

Table 5.2: Fitting parameter results for the FCS curves shown in Fig 5.17c and Fig 5.20c

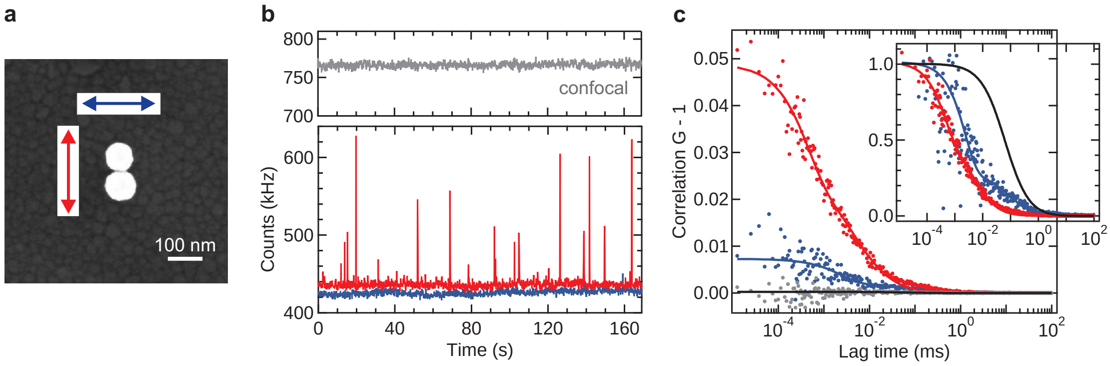

Figure 5.17: (a)SEM image of a typical dimer (without PEG) used in the experiment , with the excitation polarization set parallel (red arrow) and perpendicular (blue arrow) (b) and (c) shows the time traces and correlation functions in the case of the two polarization and confocal measurement (in black) respectively.

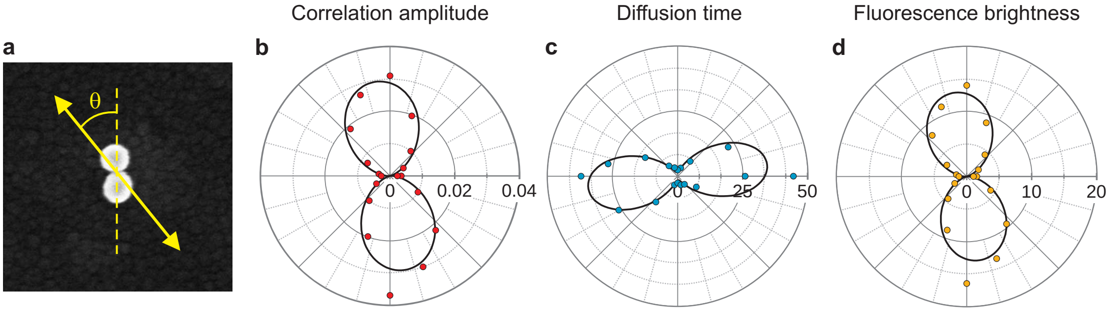

Figure 5.18: (a) it shows the angular variation, θ, of the excitation polarization set from the dimer axis. (b),(c) and (d) represent the variation of correlation amplitude, diffusion time and fluorescence brightness with changing θ.

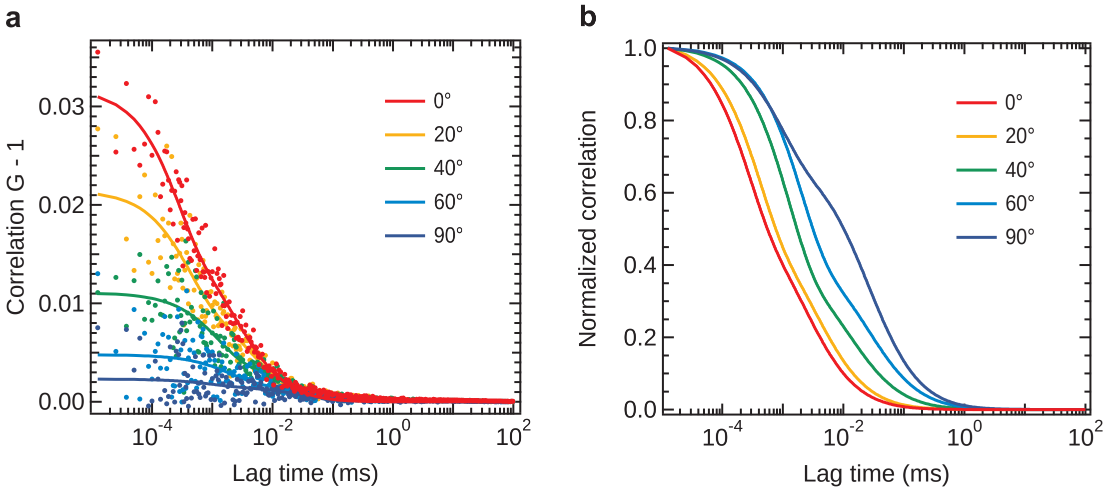

Figure 5.19: Figure shows the (a) FCS curves and (b) the normalized FCS curves for different angles θ as measured in 5.18.

Angular measurement on dimer and trimer antenna

We performed the FCS measurement on dimer antenna (without PEG) with varying the angle of excitation polarization with respect to the dimer axis (Fig 5.18a). We see a dipolar behavior for the correlation amplitude, diffusion time and fluorescence brightness (Fig 5.18b,c and d). This experiment proves the stability of our FCS measurements and intensify the fact that the molecules are passing through the hot-spot and the FCS signal is coming from the hot-spot. Also, it proves that there is a minimum of molecular sticking going on during the experiment. Figure 5.19a gives the FCS curve for various angles showing that in parallel case (0°) the amplitude is maximum (means lowest number of molecule in the detection volume) and as we tend to the perpendicular case it starts decreasing and finally going to minimum at 90°. Fig 5.19b displays the temporal variation for various angles. In the case of trimers (fig. 5.20c), we see reduced effect of polarization angle variation giving the idea that the symmetrical structure of trimers play and important role here and the fluorescence signal stems from the central region between the three spherical nanoparticles.

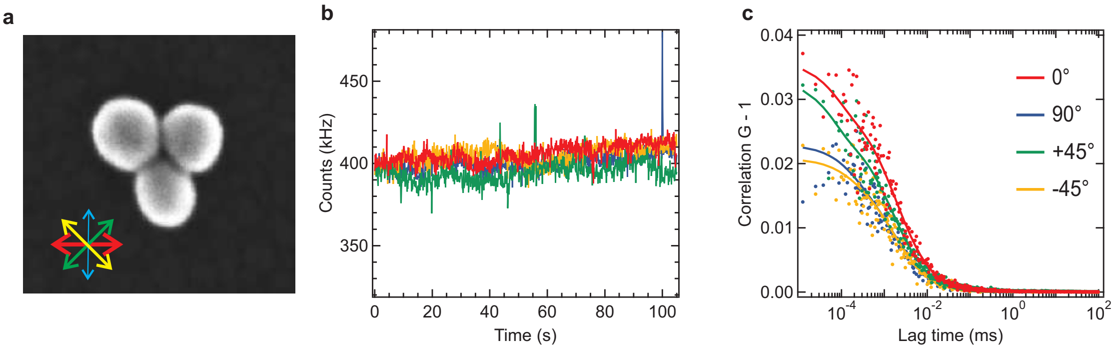

Figure 5.20: (a) SEM image of a typical trimer (with PEG) used in FCS measurements (b) and (c) show Fluorescence intensity time traces and FCS curves taken at four different excitation polarization angles.

Fluorescence Enhancement and Volume reduction

We have used gold dimers with and without PEG and trimers with and without PEG to perform various FCS measurements. Figure 5.21 displays the results obtained by performing experiments on various dimers and trimers. Fig 5.21b displays the six different cases: Dimer, Dimer(with PEG), Trimer, Trimer(with PEG), Aggregates and monomer. In case of dimers without PEG we find out that depending of their gap size and orientation of excitation polarization we can get fluorescence enhancement as high as 600× and as low as 174×, similarly the maximum the volume reduction we get is 10633× and the minimum is 2067×. Using the PEG to control the gap size of dimers turns out to be working in a complicated manner. They seem to be preventing the molecules to enter into the hot-spot. Although in the case of trimer we find out that using PEG provides stability in the experiments, still not clear with the point that how it influences the fluorescence enhancement and volume reduction. FCS experiments on aggregates provides very poor results. Single gold nanoparticles of 80 nm diameter results from earlier experiments are used here for the comparison. Table 5.3 summarizes the average results in all the six cases with the standard deviation for fluorescence enhancement and volume reduction measurements.

5.3 Conclusion

Colloidal nanoparticles represent an inexpensive and versatile platform to perform a wide variety of biochemical assays in solution with single molecule resolution at the biologically relevant micromolar concentration regime. In the first section, we perform FCS measurements

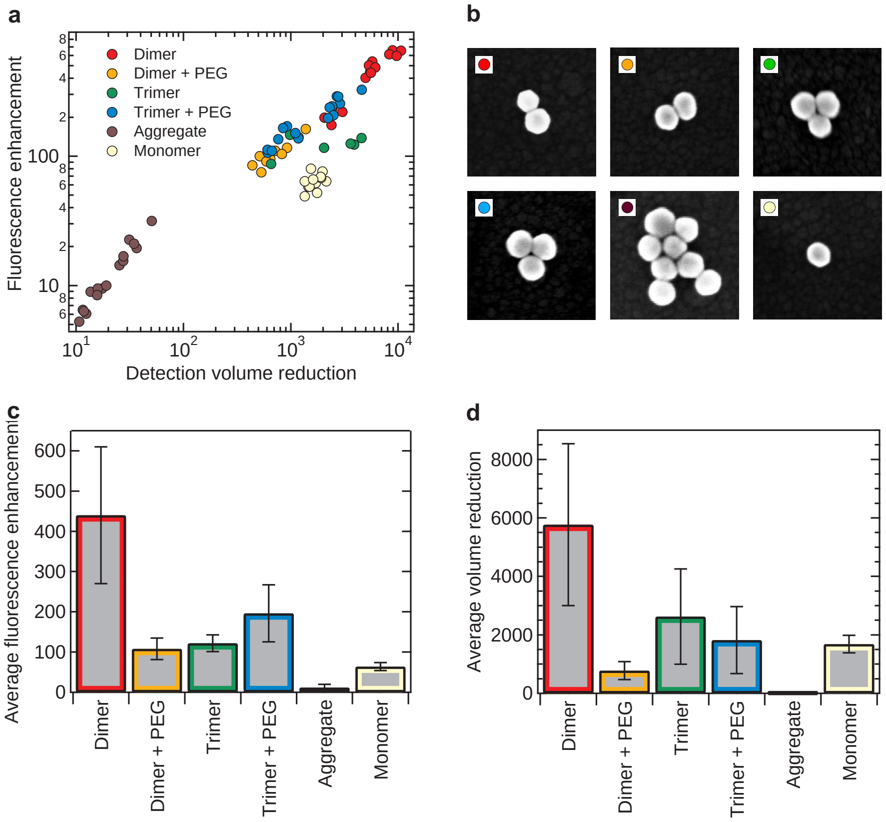

Figure 5.21: **Fluorescence enhancement and volume reduction:** (a) Scatter plot of fluorescence enhancement versus volume reduction for six different case as shown in (b) Dimer without PEG (red), Dimer with PEG (orange), Trimer without peg(green), trimer with PEG (blue), Aggregate (brown) and monomer (yellow) (c) and (d) Average fluorescence enhancement for the six cases respectively

	$\eta_{F,avg}$	sdev(η_F)	$R_{v,avg}$	sdev(R_v)
Dimer (no PEG)	440	170	5800	2800
Dimer (with PEG)	110	27	780	310
Trimer (no PEG)	120	21	2630	1630
Trimer (with PEG)	200	71	1820	1150
Aggregates	12	8	21	12
Monomer	64	10	1690	300

Table 5.3: Tabulated results for the FCS measurement in case of six different self assemblies (see Fig 5.21b. Here $\eta_{F,avg}$ represents average Fluorescence Enhancement, sdev(η_F) gives the standard deviation of Fluorescence enhancement measurement, $R_{v,avg}$ gives the value of Average volume reduction and sdev(R_v) give the standard deviation of volume reduction measurement.

on single gold nanoparticles of sizes ranging from 60 nm to 150 nm. We found out that for 80 nm gold nanoparticles we can get 60× enhancement in the fluorescence signal using a low quantum yield fluorescent species. We also get the detection volume down to 270 zL(three orders of magnitude beyond the diffraction barrier) in a micormolar solution. These quantitative measurements of near field detection volume and fluorescence enhancement factor have been extended to the study of dimers and trimers in the next section. Although the experiment is still in its primary stage, the results we have got are very promising. We can get a dimer antenna enhancing the fluorescence signal by 440× on average inside a detection volume which is reduced by a factor of 5800× on average.

Conclusion and Perspective

Monitoring single molecule at the physiologically relevant micromolar concentration regime imposes to rethink the optical microscope apparatus to break the diffraction limit. This difficulty can be accounted as one of the main limitations for the broad applicability of optical single-molecule detection in biology and medicine [8, 10]. The ability to reliably fabricate nanostructrues to confine and enhance the light into nanoscale volumes paves the way to overcome the diffraction challenge, and several methods based on zero-mode waveguides or plasmonic antennas have been reviewed in this first chapter of this thesis. Optical antennas are trending as attractive optical element to manipulate and control light-matter interaction at the single-emitter level reaching nanoscale resolution in a variety of innovative ways, giving them the potential to be used in a broad range of research.

The properties of fluorescence emission of a fluorophore, depend on the local environment. In order to enhance the fluorescence signal, the process of tailoring the local environment can be very useful. In particular, the emission of fluorescence from a molecule can be greatly enhanced near nanoantenna's plasmonic environment. The physical origin of this enhancement due to antenna, lies in the changes of electromagnetic environment by enhancing the excitation intensity and/or by tailoring the radiation pattern and/or by increasing the radiative rate transmission from the emitter. These changes depend heavily on the sizes, shapes and types of nanoantennas studied. For this reason, the complete experimental characterization of interactions between nanoantennas and fluorescent molecules, and more generally the study of light-matter interactions at the nanoscale, is becoming a topic of great interest [121–124]. However, we have to keep it in mind that the determination of the influence of different physical changes created by the antenna is not that trivial, because the enhancement of fluorescence measured is an intricate combination of the enhancements in excitation intensity and the emission intensity of the molecules. The experimental procedures used in our lab for fluorescence characterization tackles this issue efficiently, combining the studies of fluorescence correlation spectroscopy (FCS) and the measurements of fluorescence lifetime using time correlated single photon counting (TCSPC). This procedure allows to discriminate the relative excitation and emission gains contributing to the overall enhancement of fluorescence.

Focused Ion Beam (FIB) milled Nanoantenna-in-box design (Chapter 4) significantly shows the pathway to perform single molecule fluorescence study at micromolar concentration very efficiently. Using the dominant fluorescence emission from the nanoantenna gap region together with background screening afforded by the surrounding box, we isolated detection volumes down to 58 zL, accompanied by a 1100-fold fluorescence enhancement. By changing the local sample concentration we showed that our design can accurately quantify the number of detected molecules inside the hot spot and the concentration can be raised above 20 μ M while still having less than one molecule detected in the hot spot. We investigated different biomolecules labeled with different fluorophores viz the cellular protein Annexin 5b labeled with Cyanine5 fluorescent dye, double stranded DNA constructs of 11, 40 and 51 base pairs (bp) labeled with Atto647N, and the cell wall surface protein Protein A labeled with Alexa Fluor 647. We concluded that the “antenna-in-box” can be readily used to determine relative diffusion coefficients at high physiologically relevant concentrations, and to distinguish between different fluorescent species based on their diffusion properties. This preludes a new class of nanoscale biomolecular studies to investigate enzymatic reactions [45, 46], and nanoscale composition of live cell membranes [20, 137].

Colloidal nanoparticles (Chapter 5) represent an inexpensive and versatile platform to perform a wide variety of biochemical assays in solution with single molecule resolution at the biologically relevant micromolar concentration regime. In the first section, we perform FCS measurements on single gold nanoparticles of sizes ranging from 60 nm to 150 nm. We found out that for 80 nm gold nanoparticles we can get 60× enhancement in the fluorescence signal using a low quantum yield fluorescent species. We also get the detection volume down to 270 zL(three orders of magnitude beyond the diffraction barrier) in a micormolar solution. These quantitative measurements of near field detection volume and fluorescence enhancement factor have been extended to the study of dimers and trimers in the next section. Although the experiment is still in its primary stage, the results we have got are very promising. We can get a dimer antenna enhancing the fluorescence signal by 440× on average inside a detection volume which is reduced by a factor of 5800× on average.

The results in this thesis demonstrate the potential of optical antennas, fabricated by top-down ("antenna-in-box” platform) and bottom-up approach (colloidal synthesis of antennas using gold nanoparticles), to confine light and detect single molecule fluorescence at biologically relevant high concentrations regime. Moreover, the plasmonic approach can benefit from other approaches using advanced microscopy techniques [19, 20], dielectric-based antennas [83, 84], microfluidics [85, 86], or optical fibre probes [87–89]. All these techniques, and their combination, significantly expand the single molecule toolbox. The application to biological problems is an emerging and exciting field, which is promising to reveal new insights on biological functions and dynamics.

Bibliography

[1] Jose M Moran-Mirabal and Harold G Craighead. Zero-mode waveguides: subwavelength nanostructures for single molecule studies at high concentrations. Methods (San Diego, Calif.), 46(1):11–7, September 2008.

[2] K T Samiee, M Foquet, L Guo, E C Cox, and H G Craighead. lambda-Repressor oligomerization kinetics at high concentrations using fluorescence correlation spectroscopy in zero-mode waveguides. Biophysical journal, 88(3):2145–53, March 2005.

[3] Ch Zander, J Enderlein, and R A Keller, editors. Single Molecule Detection in Solution-Methods and Applications. Wiley-VCH Verlag GmbH & Co. KGaA, 2002.

[4] N L Thompson, T P Burghardt, and D Axelrod. Measuring surface dynamics of biomolecules by total internal reflection fluorescence with photobleaching recovery or correlation spectroscopy. Biophysical journal, 33(3):435–54, March 1981.

[5] Kai Hassler, Marcel Leutenegger, Per Rigler, Ramachandra Rao, Rudolf Rigler, Michael Gösch, and Theo Lasser. Total internal reflection fluorescence correlation spectroscopy (TIR-FCS) with low background and high count-rate per molecule. Optics express, 13(19):7415–23, September 2005.

[6] T E Starr and N L Thompson. Total internal reflection with fluorescence correlation spectroscopy: combined surface reaction and solution diffusion. Biophysical journal, 80(3):1575–84, March 2001.

[7] H Blom, L Kastrup, and C Eggeling. Fluorescence fluctuation spectroscopy in reduced detection volumes. Current pharmaceutical biotechnology, 7(1):51–66, February 2006.

[8] Maria F. Garcia-Parajo. Optical antennas focus in on biology. Nature Photonics, 2(4):201–203, April 2008.

[9] Jérome Wenger and Hervé Rigneault. Photonic methods to enhance fluorescence correlation spectroscopy and single molecule fluorescence detection. International journal of molecular sciences, 11(1):206–21, January 2010.

[10] Phil Holzmeister, Guillermo P Acuna, Dina Grohmann, and Philip Tinnefeld. Breaking the concentration limit of optical single-molecule detection. Chemical Society reviews, 43(4):1014–28, February 2014.

[11] Philip Tinnefeld. Single-molecule detection: Breaking the concentration barrier. Nature nanotechnology, 8(7):480–2, July 2013.

[12] Nathalie P. de Leon, Brendan J. Shields, Chun L. Yu, Dirk E. Englund, Alexey V. Akimov, Mikhail D. Lukin, and Hongkun Park. Tailoring Light-Matter Interaction with a Nanoscale Plasmon Resonator. Physical Review Letters, 108(22):226803, May 2012.

[13] AG Curto, TH Taminiau, and Giorgio Volpe. Multipolar radiation of quantum emitters with nanowire optical antennas. Nature …, 4:1750, April 2013.

[14] Jon a Schuller, Edward S Barnard, Wenshan Cai, Young Chul Jun, Justin S White, and Mark L Brongersma. Plasmonics for extreme light concentration and manipulation. Nature materials, 9(3):193–204, March 2010.

[15] D Punj, P Ghenuche, S B Moparthi, J de Torres, V Grigoriev, H Rigneault, and J Wenger. Plasmonic antennas and zero-mode waveguides to enhance single molecule fluorescence detection and fluorescence correlation spectroscopy toward physiological concentrations. WIREs Nanomed Nanobiotechnol, 6:268–282, 2014.

[16] P.-F. Lenne, E. Etienne, and H. Rigneault. Subwavelength patterns and high detection efficiency in fluorescence correlation spectroscopy using photonic structures. Applied Physics Letters, 80(22):4106, 2002.

[17] H Rigneault and P-f Lenne. Fluorescence correlation spectroscopy on a mirror. JOSA B, 20(10):2203–2214, 2003.

[18] Stefan W Hell. Toward fluorescence nanoscopy. Nature biotechnology, 21(11):1347–55, November 2003.

[19] Lars Kastrup, Hans Blom, Christian Eggeling, and Stefan Hell. Fluorescence Fluctuation Spectroscopy in Subdiffraction Focal Volumes. Physical Review Letters, 94(17):1–4, May 2005.

[20] Christian Eggeling, Christian Ringemann, Rebecca Medda, Günter Schwarzmann, Konrad Sandhoff, Svetlana Polyakova, Vladimir N Belov, Birka Hein, Claas von Middendorff, Andreas Schönle, and Stefan W Hell. Direct observation of the nanoscale dynamics of membrane lipids in a living cell. Nature, 457(7233):1159–62, February 2009.

[21] Anatoli Ianoul, Donna D Grant, Yanouchka Rouleau, Mahmud Bani-Yaghoub, Linda J Johnston, and John Paul Pezacki. Imaging nanometer domains of [beta]-adrenergic receptor complexes on the surface of cardiac myocytes. Nat Chem Biol, 1(4):196–202, September 2005.

[22] Bärbel I de Bakker, Frank de Lange, Alessandra Cambi, Jeroen P Korterik, Erik M H P van Dijk, Niek F van Hulst, Carl G Figdor, and Maria F Garcia-Parajo. Nanoscale organization of the pathogen receptor DC-SIGN mapped by single-molecule high-resolution fluorescence microscopy. Chemphyschem : a European journal of chemical physics and physical chemistry, 8(10):1473–80, July 2007.

[23] Bärbel I de Bakker, Andrea Bodnár, Erik M H P van Dijk, György Vámosi, Sándor Damjanovich, Thomas a Waldmann, Niek F van Hulst, Attila Jenei, and María F Garcia-Parajo. Nanometer-scale organization of the alpha subunits of the receptors for IL2 and IL15 in human T lymphoma cells. Journal of cell science, 121(Pt 5):627–33, March 2008.

[24] Dusan Vobornik, Daniel S. Banks, Zhengfang Lu, Cécile Fradin, Rod Taylor, and Linda J. Johnston. Fluorescence correlation spectroscopy with sub-diffraction-limited resolution using near-field optical probes. Applied Physics Letters, 93(16):–, 2008.

[25] Michael Herrmann, Nicole Neuberth, Jörg Wissler, José Pérez, Dietmar Gradl, and Andreas Naber. Near-field optical study of protein transport kinetics at a single nuclear pore. Nano Letters, 9(9):3330–3336, 2009. PMID: 19591452.

[26] Carlo Manzo, Thomas S van Zanten, and Maria F Garcia-Parajo. Nanoscale fluorescence correlation spectroscopy on intact living cell membranes with NSOM probes. Biophysical journal, 100(2):L8–10, January 2011.

[27] Mathieu Mivelle, Thomas S van Zanten, Lars Neumann, Niek F van Hulst, and Maria F Garcia-Parajo. Ultrabright bowtie nanoaperture antenna probes studied by single molecule fluorescence. Nano letters, 12(11):5972–8, November 2012.

[28] Pascal Anger, Palash Bharadwaj, and Lukas Novotny. Enhancement and Quenching of Single-Molecule Fluorescence. Physical Review Letters, 96(11):3–6, March 2006.

[29] Sergei Kühn, Ulf Hå kanson, Lavinia Rogobete, and Vahid Sandoghdar. Enhancement of Single-Molecule Fluorescence Using a Gold Nanoparticle as an Optical Nanoantenna. Physical Review Letters, 97(1):1–4, July 2006.

[30] T. H. Taminiau, F. D. Stefani, F. B. Segerink, and N. F. van Hulst. Optical antennas direct single-molecule emission. Nature Photonics, 2(4):234–237, March 2008.

[31] Thomas S van Zanten, Maria J Lopez-Bosque, and Maria F Garcia-Parajo. Imaging individual proteins and nanodomains on intact cell membranes with a probe-based optical antenna. Small (Weinheim an der Bergstrasse, Germany), 6(2):270–5, January 2010.

[32] M J Levene, J Korlach, S W Turner, M Foquet, H G Craighead, and W W Webb. Zero-mode waveguides for single-molecule analysis at high concentrations. Science (New York, N.Y.), 299(5607):682–6, January 2003.

[33] Hervé Rigneault, Jérémie Capoulade, José Dintinger, Jérôme Wenger, Nicolas Bonod, Evgeni Popov, Thomas Ebbesen, and Pierre-François Lenne. Enhancement of Single-Molecule Fluorescence Detection in Subwavelength Apertures. Physical Review Letters, 95(11):117401, September 2005.

[34] Marcel Leutenegger, Michael Gösch, Alexandre Perentes, Patrik Hoffmann, Olivier J F Martin, and Theo Lasser. Confining the sampling volume for Fluorescence Correlation

Spectroscopy using a sub-wavelength sized aperture. Optics express, 14(2):956–69, January 2006.

[35] Davy Gérard, Jérôme Wenger, Nicolas Bonod, Evgeni Popov, Hervé Rigneault, Farhad Mahdavi, Steve Blair, José Dintinger, and Thomas Ebbesen. Nanoaperture-enhanced fluorescence: Towards higher detection rates with plasmonic metals. Physical Review B, 77(4):045413, January 2008.

[36] Heykel Aouani, Stella Itzhakov, David Gachet, Eloïse Devaux, Thomas W Ebbesen, Hervé Rigneault, Dan Oron, and Jérôme Wenger. Colloidal quantum dots as probes of excitation field enhancement in photonic antennas. ACS nano, 4(8):4571–8, August 2010.

[37] F. Mahdavi, Y. Liu, and S. Blair. Modeling Fluorescence Enhancement from Metallic Nanocavities. Plasmonics, 2(3):129–141, August 2007.

[38] Farhad Mahdavi and Steve Blair. Nanoaperture Fluorescence Enhancement in the Ultraviolet. Plasmonics, 5(2):169–174, March 2010.

[39] Jérôme Wenger, Davy Gérard, Heykel Aouani, and Hervé Rigneault. Nanoaperture-enhanced signal-to-noise ratio in fluorescence correlation spectroscopy. Analytical chemistry, 81(2):834–9, January 2009.

[40] Takeo Miyake, Takashi Tanii, Hironori Sonobe, Rena Akahori, Naonobu Shimamoto, Taro Ueno, Takashi Funatsu, and Iwao Ohdomari. Real-time imaging of single-molecule fluorescence with a zero-mode waveguide for the analysis of protein-protein interaction. Analytical chemistry, 80(15):6018–22, August 2008.

[41] Tomoya Sameshima, Ryo Iizuka, Taro Ueno, Junichi Wada, Mutsuko Aoki, Naonobu Shimamoto, Iwao Ohdomari, Takashi Tanii, and Takashi Funatsu. Single-molecule study on the decay process of the football-shaped GroEL-GroES complex using zero-mode waveguides. The Journal of biological chemistry, 285(30):23159–64, July 2010.

[42] David Liao, Peter Galajda, Robert Riehn, Rob Ilic, Jason L Puchalla, Howard G Yu, Harold G Craighead, and Robert H Austin. Single molecule correlation spectroscopy in continuous flow mixers with zero-mode waveguides. Optics express, 16(14):10077–90, July 2008.

[43] Jérôme Wenger, Davy Gérard, Pierre-François Lenne, Hervé Rigneault, José Dintinger, Thomas W Ebbesen, Annie Boned, Fabien Conchonaud, and Didier Marguet. Dual-color fluorescence cross-correlation spectroscopy in a single nanoaperture : towards rapid multicomponent screening at high concentrations. Optics express, 14(25):12206–16, December 2006.

[44] Tor Sandén, Romain Wyss, Christian Santschi, Ghérici Hassaïne, Cédric Deluz, Olivier J F Martin, Stefan Wennmalm, and Horst Vogel. A zeptoliter volume meter for analysis of single protein molecules. Nano letters, 12(1):370–5, January 2012.

[45] John Eid, Adrian Fehr, Jeremy Gray, Khai Luong, John Lyle, and Geoff Otto. Real-time DNA sequencing from single polymerase molecules. Science, 323:133–138, 2009.

[46] Sotaro Uemura, Colin Echeverría Aitken, Jonas Korlach, Benjamin a Flusberg, Stephen W Turner, and Joseph D Puglisi. Real-time tRNA transit on single translating ribosomes at codon resolution. Nature, 464(7291):1012–7, April 2010.

[47] Ben McNally, Alon Singer, Zhiliang Yu, Yingjie Sun, Zhiping Weng, and Amit Meller. Optical recognition of converted DNA nucleotides for single-molecule DNA sequencing using nanopore arrays. Nano letters, 10(6):2237–44, June 2010.

[48] Jose M Moran-Mirabal, Alexis J Torres, Kevan T Samiee, Barbara a Baird, and Harold G Craighead. Cell investigation of nanostructures: zero-mode waveguides for plasma membrane studies with single molecule resolution. Nanotechnology, 18(19):195101, May 2007.

[49] Joshua B Edel, Min Wu, Barbara Baird, and Harold G Craighead. High spatial resolution observation of single-molecule dynamics in living cell membranes. Biophysical journal, 88(6):L43–5, June 2005.

[50] K T Samiee, J M Moran-Mirabal, Y K Cheung, and H G Craighead. Zero mode waveguides for single-molecule spectroscopy on lipid membranes. Biophysical journal, 90(9):3288–99, May 2006.

[51] Jérôme Wenger, Hervé Rigneault, José Dintinger, Didier Marguet, and Pierre-François Lenne. Single-fluorophore diffusion in a lipid membrane over a subwavelength aperture. Journal of biological physics, 32(1):SN1–4, January 2006.

[52] Jérôme Wenger, Fabien Conchonaud, José Dintinger, Laure Wawrezinieck, W Thomas, Thomas W Ebbesen, Hervé Rigneault, Didier Marguet, and Pierre-François Lenne. Diffusion analysis within single nanometric apertures reveals the ultrafine cell membrane organization. Biophysical journal, 92(3):913–9, February 2007.

[53] Christopher I Richards, Khai Luong, Rahul Srinivasan, Stephen W Turner, Dennis a Dougherty, Jonas Korlach, and Henry a Lester. Live-cell imaging of single receptor composition using zero-mode waveguide nanostructures. Nano letters, 12(7):3690–4, July 2012.

[54] Christopher V Kelly, Barbara a Baird, and Harold G Craighead. An array of planar apertures for near-field fluorescence correlation spectroscopy. Biophysical journal, 100(7):L34–6, April 2011.

[55] Heykel Aouani, Oussama Mahboub, Eloïse Devaux, Hervé Rigneault, Thomas W Ebbesen, and Jérôme Wenger. Plasmonic antennas for directional sorting of fluorescence emission. Nano letters, 11(6):2400–6, June 2011.

[56] Heykel Aouani, Oussama Mahboub, Nicolas Bonod, Eloïse Devaux, Evgeny Popov, Hervé Rigneault, Thomas W Ebbesen, and Jérôme Wenger. Bright unidirectional fluorescence emission of molecules in a nanoaperture with plasmonic corrugations. Nano letters, 11(2):637–44, February 2011.

[57] Heykel Aouani, Oussama Mahboub, Eloïse Devaux, Hervé Rigneault, Thomas W Ebbesen, and Jérôme Wenger. Large molecular fluorescence enhancement by a nanoaperture with plasmonic corrugations. Optics express, 19(14):13056–62, July 2011.

[58] Young Chul Jun, Kevin C Y Huang, and Mark L Brongersma. Plasmonic beaming and active control over fluorescent emission. Nature communications, 2:283, January 2011.

[59] Lutz Langguth, Deep Punj, Jérôme Wenger, and AF Koenderink. Plasmonic band structure controls single-molecule fluorescence. ACS nano, 7(10):8840–8848, 2013.

[60] Anika Kinkhabwala, Zongfu Yu, Shanhui Fan, Yuri Avlasevich, Klaus Müllen, and W. E. Moerner. Large single-molecule fluorescence enhancements produced by a bowtie nanoantenna. Nature Photonics, 3(11):654–657, October 2009.

[61] T Lohmüller, L Iversen, M Schmidt, C Rhodes, H-L Tu, W-C Lin, and J T Groves. Single molecule tracking on supported membranes with arrays of optical nanoantennas. Nano letters, 12(3):1717–21, March 2012.

[62] Deep Punj, Mathieu Mivelle, Satish Babu Moparthi, Thomas S van Zanten, Hervé Rigneault, Niek F van Hulst, María F García-Parajó, and Jérôme Wenger. A plasmonic 'antenna-in-box' platform for enhanced single-molecule analysis at micromolar concentrations. Nature nanotechnology, 8(7):512–6, July 2013.

[63] Nathan C Lindquist, Prashant Nagpal, Kevin M McPeak, David J Norris, and Sang-Hyun Oh. Engineering metallic nanostructures for plasmonics and nanophotonics. Reports on progress in physics. Physical Society (Great Britain), 75(3):036501, March 2012.

[64] Paolo Biagioni, Jer-Shing Huang, and Bert Hecht. Nanoantennas for visible and infrared radiation. Reports on progress in physics, 75(2):024402, February 2012.

[65] LJ Guo. Nanoimprint lithography: methods and material requirements. Advanced Materials, 19(4):495–513, February 2007.

[66] Anika a. Kinkhabwala, Zongfu Yu, Shanhui Fan, and W.E. Moerner. Fluorescence correlation spectroscopy at high concentrations using gold bowtie nanoantennas. Chemical Physics, 406:3–8, October 2012.

[67] Alberto G Curto, Giorgio Volpe, Tim H Taminiau, Mark P Kreuzer, Romain Quidant, and Niek F van Hulst. Unidirectional emission of a quantum dot coupled to a nanoantenna. Science (New York, N.Y.), 329(5994):930–3, August 2010.

[68] Paul W K Rothemund. Folding DNA to create nanoscale shapes and patterns. Nature, 440(7082):297–302, March 2006.

[69] Matthew Rycenga, Claire M Cobley, Jie Zeng, Weiyang Li, Christine H Moran, Qiang Zhang, Dong Qin, and Younan Xia. Controlling the synthesis and assembly of silver nanostructures for plasmonic applications. Chemical reviews, 111(6):3669–712, June 2011.

[70] Matthew R Jones, Kyle D Osberg, Robert J Macfarlane, Mark R Langille, and Chad a Mirkin. Templated techniques for the synthesis and assembly of plasmonic nanostructures. Chemical reviews, 111(6):3736–827, June 2011.

[71] Laura C Estrada, Pedro F Aramendía, and Oscar E Martínez. 10000 Times Volume Reduction for Fluorescence Correlation Spectroscopy Using Nano-Antennas. Optics express, 16(25):20597–602, December 2008.

[72] Qingyan Wang, Guowei Lu, Lei Hou, Tianyue Zhang, Chunxiong Luo, Hong Yang, Grégory Barbillon, Franck H. Lei, Christophe a. Marquette, Pascal Perriat, Olivier Tillement, Stéphane Roux, Qi Ouyang, and Qihuang Gong. Fluorescence correlation spectroscopy near individual gold nanoparticle. Chemical Physics Letters, 503(4-6):256–261, February 2011.

[73] Guowei Lu, Jie Liu, Tianyue Zhang, Wenqiang Li, Lei Hou, Chunxiong Luo, Franck Lei, Michel Manfait, and Qihuang Gong. Plasmonic near-field in the vicinity of a single gold nanoparticle investigated with fluorescence correlation spectroscopy. Nanoscale, 4(11):3359–64, June 2012.

[74] Haifeng Yuan, Saumyakanti Khatua, Peter Zijlstra, Mustafa Yorulmaz, and Michel Orrit. Thousand-fold Enhancement of Single-Molecule Fluorescence Near a Single Gold Nanorod. Angewandte Chemie, 125(4):1255–1259, January 2013.

[75] Deep Punj, Juan de Torres, Hervé Rigneault, and Jérôme Wenger. Gold nanoparticles for enhanced single molecule fluorescence analysis at micromolar concentration. Optics Express, 21(22):27338, November 2013.

[76] Sharmistha Dutta Choudhury, Krishanu Ray, and Joseph R. Lakowicz. Silver Nanostructures for Fluorescence Correlation Spectroscopy: Reduced Volumes and Increased Signal Intensities. The Journal of Physical Chemistry Letters, 3(19):2915–2919, October 2012.

[77] Mickaël P Busson, Brice Rolly, Brian Stout, Nicolas Bonod, and Sébastien Bidault. Accelerated single photon emission from dye molecule-driven nanoantennas assembled on DNA. Nature communications, 3:962, January 2012.

[78] Mickaël P Busson, Brice Rolly, Brian Stout, Nicolas Bonod, Jérôme Wenger, and Sébastien Bidault. Photonic engineering of hybrid metal-organic chromophores. Angewandte Chemie (International ed. in English), 51(44):11083–7, October 2012.

[79] Mickaël P Busson, Brice Rolly, Brian Stout, Nicolas Bonod, Eric Larquet, Albert Polman, and Sébastien Bidault. Optical and topological characterization of gold nanoparticle

dimers linked by a single DNA double strand. Nano letters, 11(11):5060–5, November 2011.

[80] Guillermo P Acuna, Martina Bucher, Ingo H Stein, Christian Steinhauer, Anton Kuzyk, Phil Holzmeister, Robert Schreiber, Alexander Moroz, Fernando D Stefani, Tim Liedl, Friedrich C Simmel, and Philip Tinnefeld. Distance dependence of single-fluorophore quenching by gold nanoparticles studied on DNA origami. ACS nano, 6(4):3189–95, April 2012.

[81] Guillermo P. Acuna, Phil Holzmeister, Friederike M. Möller, Susanne Beater, Birka Lalkens, and Philip Tinnefeld. Dna-templated nanoantennas for single-molecule detection at elevated concentrations. Journal of Biomedical Optics, 18(6):065001–065001, 2013.

[82] G P Acuna, F M Möller, P Holzmeister, S Beater, B Lalkens, and P Tinnefeld. Fluorescence enhancement at docking sites of DNA-directed self-assembled nanoantennas. Science (New York, N.Y.), 338(6106):506–10, October 2012.

[83] K. G. Lee, X. W. Chen, H. Eghlidi, P. Kukura, R. Lettow, a. Renn, V. Sandoghdar, and S. Götzinger. A planar dielectric antenna for directional single-photon emission and near-unity collection efficiency. Nature Photonics, 5(3):166–169, January 2011.

[84] Pascale Winckler, Rodolphe Jaffiol, Jérôme Plain, and Pascal Royer. Nonradiative Excitation Fluorescence: Probing Volumes Down to the Attoliter Range. The Journal of Physical Chemistry Letters, 1(16):2451–2454, August 2010.

[85] Mathieu Foquet, Jonas Korlach, Warren R Zipfel, Watt W Webb, and Harold G Craighead. Focal Volume Confinement by Submicrometer-Sized Fluidic Channels than 1 μ m were fabricated in fused silica for high-. 76(6):1618–1626, 2004.

[86] John F Lesoine, Prahnesh a Venkataraman, Peter C Maloney, Mark E Dumont, and Lukas Novotny. Nanochannel-based single molecule recycling. Nano letters, 12(6):3273–8, June 2012.

[87] Guowei Lu, Franck H Lei, Jean-François Angiboust, and Michel Manfait. Confined detection volume of fluorescence correlation spectroscopy by bare fiber probes. European biophysics journal : EBJ, 39(5):855–60, April 2010.

[88] Heykel Aouani, Patrick Ferrand, and Neso Sojic. Optical-fiber-microsphere for remote fluorescence correlation spectroscopy Abstract :. 17(21):19085–19092, 2009.

[89] Petru Ghenuche. Hollow-core photonic crystal fiber probe for remote fluorescence sensing with single molecule sensitivity Abstract :. 20(27):19085–19092, 2012.

[90] Kerry J Vahala. Optical microcavities. Nature, 424(6950):839–46, August 2003.

[91] Stefan Schietinger, Michael Barth, Thomas Aichele, and Oliver Benson. Plasmon-enhanced single photon emission from a nanoassembled metal-diamond hybrid structure at room temperature. Nano letters, 9:1694–1698, 2009.

[92] C Kittle. Introduction to solid state physics. John Wiley & Sons, New York, 1996.

[93] U Kriebig and M Vollmer. Optical Properties of metal clusters. Springer, Berlin, 1995.

[94] Stefan A Maier. Plasmonics:Fundamental and Applications. Berlin:Springer, 2007.

[95] L Novotny and B Hecht. Principles of Nano-Optics. Cambridge University Press, 2nd edition, 2006.

[96] A. Mohammadi, V. Sandoghdar, and M. Agio. Gold, copper, silver and aluminum nanoantennas to enhance spontaneous emission. Journal of Computational and Theoretical Nanoscience, 6(9):2024–2030, 2009.

[97] J D Jackson. Classical Electrodynamics. New York: Wiley, 1999.

[98] C F Bohren and D R Huffman. Absorption and Scattering of Light by Small Particles. John Wiley & Sons, New York, 1983.

[99] Filippo Capolino. Theory and Phenomena of Metamaterials. CRC Press, Taylor and Francis Group, 2009.

[100] a. Wokaun, J. P. Gordon, and P. F. Liao. Radiation damping in surface-enhanced Raman scattering. Physical Review Letters, 48(14):957–960, 1982.

[101] Pedro de Vries, David van Coevorden, and Ad Lagendijk. Point scatterers for classical waves. Reviews of Modern Physics, 70(2):447–466, 1998.

[102] Victor Grigoriev, Nicolas Bonod, Jérôme Wenger, and Brian Stout. Optimizing Nanoparticle Designs for Ideal Absorption of Light. ACS Photonics, page 150205142313007, 2015.

[103] P. Alitalo, C. Simovski, a. Viitanen, and S. Tretyakov. Near-field enhancement and subwavelength imaging in the optical region using a pair of two-dimensional arrays of metal nanospheres. Physical Review B - Condensed Matter and Materials Physics, 74:1–6, 2006.

[104] A. Femius Koenderink and Albert Polman. Complex response and polariton-like dispersion splitting in periodic metal nanoparticle chains. Physical Review B - Condensed Matter and Materials Physics, 74:1–4, 2006.

[105] Palash Bharadwaj, Bradley Deutsch, and Lukas Novotny. Optical Antennas. Advances in Optics and Photonics, 1(3):438, August 2009.

[106] P.R. West, S. Ishii, G.V. Naik, N.K. Emani, V.M. Shalaev, and a. Boltasseva. Searching for better plasmonic materials. Laser & Photonics Reviews, 4(6):795–808, November 2010.

[107] Mario Agio. Optical antennas as nanoscale resonators. Nanoscale, 4(3):692–706, February 2012.

[108] E. M. Purcell. Spontaneous emission probabilities at radio frequencies. volume 69, page 681, 1946.

[109] Montacer Dridi and George C Schatz. Model for describing plasmon-enhanced lasers that combines rate equations with finite-difference time-domain. Journal of the Optical Society of America B, 30(11):2791–2797, 2013.

[110] Vincenzo Giannini, José a. Sánchez-Gil, Otto L. Muskens, and Jaime Gómez Rivas. Electrodynamic calculations of spontaneous emission coupled to metal nanostructures of arbitrary shape: nanoantenna-enhanced fluorescence. Journal of the Optical Society of America B, 26(8):1569, July 2009.

[111] Vincenzo Giannini, Antonio I Fernández-Domínguez, Yannick Sonnefraud, Tyler Roschuk, Roberto Fernández-García, and Stefan a Maier. Controlling light localization and light-matter interactions with nanoplasmonics. Small (Weinheim an der Bergstrasse, Germany), 6(22):2498–507, November 2010.

[112] P R Berman. Cavity Quantum Electrodynamics. Academic Press, San Diego CA, 1994.

[113] C. Sauvan, J. P. Hugonin, I. S. Maksymov, and P. Lalanne. Theory of the spontaneous optical emission of nanosize photonic and plasmon resonators. Physical Review Letters, 110(June):1–5, 2013.

[114] a F Koenderink. On the use of Purcell factors for plasmon antennas. Optics letters, 35(24):4208–10, December 2010.

[115] Mario Agio and Diego Martin Cano. Nano-optics: The Purcell factor of nanoresonators. Nature Photonics, 7(9):674–675, August 2013.

[116] J Sun, S Carney, and J Schotland. Strong tip effects in near-field optical tomography. Journal of Applied Physics, 102:103103, 2007.

[117] Ertugrul Cubukcu, Eric a. Kort, Kenneth B. Crozier, and Federico Capasso. Plasmonic laser antenna. Applied Physics Letters, 89(9):093120, 2006.

[118] Liang Tang, Sukru Ekin Kocabas, Salman Latif, Ali K. Okyay, Dany-Sebastien Ly-Gagnon, Krishna C. Saraswat, and David A. B. Miller. Nanometre-scale germanium photodetector enhanced by a near-infrared dipole antenna. Nat Photon, 2(4):226–229, 2008.

[119] Robert Filter, Karolina Słowik, Jakob Straubel, Falk Lederer, and Carsten Rockstuhl. Nanoantennas for ultrabright single photon sources. Optics letters, 39(5):1246–9, March 2014.

[120] Brahim Lounis and Michel Orrit. Single-photon sources. Reports on Progress in Physics, 68(5):1129–1179, May 2005.

[121] WL Barnes. Fluorescence near interfaces: the role of photonic mode density. journal of modern optics, 45(4):661–699, 1998.

[122] JR Lakowicz. Radiative decay engineering 5: metal-enhanced fluorescence and plasmon emission. Analytical biochemistry, 337(2):171–194, 2005.

[123] Emmanuel Fort and Samuel Grésillon. Surface enhanced fluorescence. Journal of Physics D: Applied Physics, 41(1):013001, January 2008.

[124] Jérôme Wenger, Davy Gérard, José Dintinger, Oussama Mahboub, Nicolas Bonod, Evgeny Popov, Thomas W Ebbesen, and Hervé Rigneault. Emission and excitation contributions to enhanced single molecule fluorescence by gold nanometric apertures. Optics express, 16(5):3008–20, 2008.

[125] Douglas Magde, E Elson, and WW Webb. Thermodynamic fluctuations in a reacting system—measurement by fluorescence correlation spectroscopy. Physical Review Letters, 29(September):705–708, 1972.

[126] Petra Schwille and Elke Haustein. Fluorescence correlation spectroscopy: An introduction to its concepts and applications.

[127] R Rigler and S Elson, E. Fluorescence Correlation Spectroscopy, Theory and Applications. Springer, Berlin, Germany, 2001.

[128] J. R. Lakowicz. Principles of Fluorescence Spectroscopy. Springer, Berlin, Germany, 2006.

[129] Michael Wahl. Time-correlated photon counting tech note tcspc 1.2. PicoQuant GmbH, January 2000.

[130] Jérôme Wenger. Fluorescence Enhancement Factors on Optical Antennas: Enlarging the Experimental Values without Changing the Antenna Design. International Journal of Optics, 2012:1–7, 2012.

[131] L Chen, D W McBranch, H L Wang, R Helgeson, F Wudl, and D G Whitten. Highly sensitive biological and chemical sensors based on reversible fluorescence quenching in a conjugated polymer. Proceedings of the National Academy of Sciences of the United States of America, 96(22):12287–92, October 1999.

[132] E D Palik. Handbook of Optical Constants of Solids. Academic Press, Boston, 1985.

[133] Jérôme Wenger, Pierre-François Lenne, Evgueni Popov, Hervé Rigneault, José Dintinger, and Thomas Ebbesen. Single molecule fluorescence in rectangular nano-apertures. Optics express, 13(18):7035–44, September 2005.

[134] a. Wokaun, H.-P. Lutz, a. P. King, U. P. Wild, and R. R. Ernst. Energy transfer in surface enhanced luminescence. The Journal of Chemical Physics, 79(1):509, 1983.

[135] Palash Bharadwaj and Lukas Novotny. Plasmon-Enhanced Photoemission from a Single Y 3 N @ C 80 Fullerene †. pages 7444–7447, 2010.

[136] Dennis E. Koppel. Statistical accuracy in fluorescence correlation spectroscopy. Physical Review A, 10(6):1938–1945, 1974.

[137] Kirsten Bacia, SA Kim, and Petra Schwille. Fluorescence cross-correlation spectroscopy in living cells. Nature methods, 3(2):83–89, 2006.

[138] Evgeny Popov, Michel Neviere, Jerome Wenger, Pierre-Francois Lenne, Herve Rigneault, Patric Chaumet, Nicolas Bonod, Jose Dintinger, and Thomas Ebbesen. Field enhancement in single subwavelength apertures. Journal of the Optical Society of America Aoptics Image Science and Vision, 23:2342–2348, 2006.

[139] Palash Bharadwaj and Lukas Novotny. Spectral dependence of single molecule fluorescence enhancement. Optics Express, 15(21):14266–14274, 2007.

[140] H. Mertens, a. Koenderink, and a. Polman. Plasmon-enhanced luminescence near noble-metal nanospheres: Comparison of exact theory and an improved Gersten and Nitzan model. Physical Review B, 76(11):115123, September 2007.

[141] Palash Bharadwaj, Pascal Anger, and Lukas Novotny. Nanoplasmonic enhancement of single-molecule fluorescence. Nanotechnology, 18(4):044017, January 2007.

[142] Joanne Manson, Dhiraj Kumar, Brian J. Meenan, and Dorian Dixon. Polyethylene glycol functionalized gold nanoparticles: the influence of capping density on stability in various media. Gold Bulletin, 44(2):99–105, April 2011.

List of Publications

Journal Articles

"A plasmonic 'antenna-in-box' platform for enhanced single-molecule analysis at micromolar concentrations"
Deep Punj, Mathieu Mivelle, Satish Babu Moparthi, Thomas S van Zanten, Hervé Rigneault, Niek F van Hulst, María F García-Parajó, and Jérôme Wenger.
Nature nanotechnology, 8(7):512–6, July 2013.

"Gold nanoparticles for enhanced single molecule fluorescence analysis at micromolar concentration"
Deep Punj, Juan de Torres, Hervé Rigneault, and Jérôme Wenger.
Optics Express, 21(22):27338-43, 2013

"Plasmonic band structure controls single-molecule fluorescence"
Lutz Langguth, **Deep Punj**, Jérôme Wenger, and AF Koenderink
ACS nano, 7(10):8840–8848, 2013.

"Plasmonic antennas and zero-mode waveguides to enhance single molecule fluores- cence detection and fluorescence correlation spectroscopy toward physiological con- centrations"
D Punj, P Ghenuche, S B Moparthi, J de Torres, V Grigoriev, H Rigneault, and J Wenger.
WIREs Nanomed Nanobiotechnol, 6:268–282, 2014.

Conference Proceedings Paper

"Single gold nanoparticles to enhance the detection of single fluorescent molecules at micromolar concentration using fluorescence correlation spectroscopy"
Deep Punj, Hervé Rigneault, and Jérôme Wenger
Proc. SPIE 9126, Nanophotonics V, 91261N (May 2, 2014)